THE ROLE OF FLUIDS IN THE LITHOSPHERIC MANTLE (CENTRAL PANNONIAN BASIN, WESTERN HUNGARY): DETAILED FLUID INCLUSION STUDY IN MANTLE XENOLITHS

PhD (Philosophiæ Doctor) Thesis

by

Márta Berkesi

Ph.D. program for Geology and Geophysics at the Ph.D. School of Earth Sciences, Eötvös Loránd University, Budapest

Chair of the Ph.D. School:
Dr. Gyula Gábris, D.Sc.
Department of Physical Geography, Eötvös University

Chair of the PhD. Program:
Dr. Andrea Mindszenty, D.Sc.
Department of Physical and Applied Geology, Eötvös University

Advisor:
Dr. Csaba Szabó, Ph.D.
Lithosphere Fluid Research Lab
Department of Petrology and Geochemistry
Institute of Geography and Earth Sciences
Eötvös University, Budapest

Consultant:
Dr. Jean Dubessy, D.Sc.
UMR 7566 et CREGU
Faculté des Sciences, Nancy Université,
Géologie et Gestion des Ressources
Minérales et Energétiques – G2R

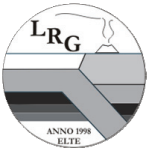

Nancy-Université
Université Henri Poincaré

"If there be light,
then there is darkness;
if cold, then heat;
if height, then depth;
if solid, then ***fluid****...*
(Pythagoras)

We're more into sort of fluid structures
that are simultaneously the most efficient,
the most beautiful, and the most engineered.
(S. Booth)

Dedicated to my Family

ACKNOWLEDGEMENT

This work would have never carried out without the help and contribution of the followings mentionned below:

First of all one of the greatest acknowledges goes to my advisor and mentor, **Csaba Szabó** for his all kind of support and patience that gave me continuously during my PhD studies; and to my consultant **Jean Dubessy** welcoming me to work at G2R lab and giving me the opportunity to use the facilities, moreover, for all of his ideas, patience and constructive criticism.

For all the administrative, logistic help and selfless of the **Lithosphere Fluid Research Lab**, Department of Petrology and Geochemistry, ELTE, Hungary and also of the **UMR G2R (Unité Mixte de Recherche, Géologie et Gestion des Ressources Minérales et Energétiques) Lab**, Nancy, France. I am particularly grateful to **Angéla Baross-Szőnyi** for dragging me many times from the labyrinth of the administration. I would like also thank to **Christine Leonard** (CNRS, Nancy, France) helping me always in logistics during my stays in France.

I am also thankful for the availability of the samples for Csaba Szabó (ELTE, Hungary) and **Károly Hidas** (University of Granada, Spain). For sample preparation special thanks goes to Margit Csömöri (ELTE, Hungary), Károly Hidas (University of Granada, Spain), Ábel Szabó (ELTE, Hungary) and Cédric Demeurie (G2R, Nancy Université, France).

To perform the data collection, i.e. the analytical measurements I am very grateful to:

1/ **Jean Dubessy, Marie-Camille Caumon, Junying Ding** (G2R, Nancy Université, France); **György Marosi, András Szabó, Balázs Vajna, Tamás Igricz** (BMGE, Budapest), for Raman microspectrometry;

2/ **Jean Dubessy, Pascal Robert, Junying Ding, Aurélien Randi, Mathieu Leisen** (G2R, Nancy Université, France) for preparing the fused silica capillaries and always thinking of the development of the equipment;

3/ **Károly Havancsák, Gábor Varga, Kitti Ratter, Zsolt Bendő** (ELTE, Hungary) for FIB-SEM measurements

4/ **Enikő Bali** (Georg August University, Göttingen), **Robert J. Bodnar** (Virginia Tech, USA), **Jean Dubessy** (G2R, Nancy Université and CNRS, France), **Luca Fedele** (Virginia Tech, USA), **Mathieu Leisen** (G2R, Nancy Université, France) for LA-ICPMS analysis;

5/ **Károly Hidas** (University of Granada, Spain), **Enikő Bali** (Georg August University, Göttingen), Detlef Krauβe (Bayerisches Geoinstitut, Germany), Ábel Szabó (ELTE, Budapest), Nigel Harris (Open University, United Kingdom), Theodoros Ntaflos (University of Vienna, Austria) for EMPA analysis;

Out of my advisor and consultant, for the fruitful discussions the followings are highly appreciated: the former and current members of the Lithosphere Fluid Research Lab, with special regard to **Tibor Guzmics, Károly Hidas, Júlia Dégi, István Kovács**, Zoltán Zajacz, Enikő Bali; the EURISPET (www.eurispet.eu) community; Robert J. Bodnar (Virginia Tech, USA); **Pascal Robert, Jacques Pironon, Mathieu Leisen, Marie-Camille Caumon** (G2R, Nancy Université, France), Junying Ding (Nanjing University, China), Tamás Váczi (Eötvös University), Vratislav Hurai (Slovak Academy of Sciences, Slovakia), the Perple_X Discussion Group (http://tech.groups.yahoo.com/group/Perple_X).

To **Françoise Perraud** (Francelab) I must thank for giving me the first chance to go to France, moreover, since then, she has never stopped helping me whenever I was in Nancy.

I must thank for the provided **financial support** of the 1/ **ELTE**, Hungary for the Ph.D. fellowship between 2007 and 2010, 2/ **TÁMOP** project nr. 4.2.1./B-09/KMR-2010-0003 by the European Union and the European Social Fund, 3/ the Department of Culture, Cooperation and Education of the **French Embassy in Hungary** (Research Scholarship for PhD students 2008, 2009, 2010); 4/ **Hungarian-French Bilateral Affair** (proposal number: FR-10/2008) to Csaba Szabó 2009-2010. This work has partly done in the framework of of the REG_KM_INFRA_09 Gábor Baross Programme (contract nr. OMFB-0038/2010).

Without my **Friends**' support and patience, this work would have been much harder to get through. Thanks to all of you guys: Sára, Katica, Orsi, Zsófi, Tacsa, Tibi, Ákos, Bence, Györgyi, Attila, Hédi, Dávid, Gábor, Petya, Alessandro, Ambrose, Christophe, Jérémy, Carolina, Laurent, Cédric (Carpentier and Demeurie), Askar, Rakhim, and those who apparently must be put in the list but their names are not coming to mind even now…! (Pour les soirées inoubliables, merci le noyau dur de la FOS team!)

Last but not least I will never be able to express my gratitude to my **Family** (Apuka, Anyuka, Anna, Judit, Pisti, Bálint, Bogi, Zsolti, the kids: Kini Bogika, Hunorka) who has always cared of and never stopped believing in me. Thanks for your abundant Love and Trust.

TABLE OF CONTENTS

LIST OF FIGURES

LIST OF TABLES

1. INTRODUCTION

Transport of melts and/or fluids through the convecting mantle are the least understood and, therefore, state-of-the-art problems among a series of processes of formation and evolution of the deep lithosphere. Although, percolation of metasomatic agents through the continental lithospheric mantle and their interaction with the peridotitic wall rock is petrographically and/or geochemically well documented, the compositions of the metasomatic melts/fluids recorded in mantle materials differ widely. For these origins many previous and recent explanations are available and are a matter of debates including silicate melts (Schiano and Clocchiatti, 1994; Bali *et al.,* 2007; 2008a,b; Dantas *et al.,* 2009; Scambelluri *et al.,* 2009; Hidas *et al.,* 2010), hydrous melts/fluids (Hartmann and Wedepohl, 1993; Zanetti *et al.,* 1999) and carbonatite melts (Green and Wallace, Watson *et al.,* 1990; Yaxley *et al.,* 1991; 1988; Rudnick *et al.,* 1993; Yaxley *et al.,* 1998; Guzmics *et al.,* 2008a, 2008b) that interacted with the mantle. The nature and composition of the metasomatic agents are inferred from the modal and chemical variations induced into the mantle by reactive melt percolation (Szabó *et al.,* 1996; Scambelluri *et al.,* 2009; Wulff-Pedersen *et al.,* 1996). One example is the orthopyroxene-enrichment in mantle xenoliths. Orthopyroxene-rich lithologies unraveled in peridotites worldwide may also be explained by several processes. The early models suggest the role of partial melting that shifts modal composition of lherzolite towards harzburgite and dunite (e.g., Arai, 1980). Recently, the significance of modal metasomatism and melt/wall rock reactions has come to the foreground (Kelemen *et al.,* 1992, 1998) by (a) the circulation of SiO_2-rich slab-derived melts or fluids formed during the dehydration or the partial melting process of the subducting oceanic crust (McInnes *et al.,* 2001; Arai *et al.,* 2006; Dantas *et al.,* 2009) and (b) the circulation of Si-oversaturated alkaline melts or sub-alkaline melts (Wulff-Pedersen *et al.,* 1996; Arai *et al.,* 2006).

Besides the obvious metasomatic effect of the percolating melt in the lithospheric upper mantle, the role of fluids as metasomatic agents has also became significant in the last decades. The composition and behavior of supercritical aqueous fluids, at upper mantle depth, as a solvent and, therefore, metasomatic agent is a subject of numerous papers (Keppler, 1996; Newton and Manning, 2000; Scambellurri and Philpot, 2001;

Kessel *et al.,* 2005; Hermann *et al.,* 2006; Spandler *et al.,* 2007). There are ongoing debates whether the hydrous melts are likely to have element concentrations that are significantly greater than coexisting aqueous fluids (e.g., Spandler *et al.,* 2007; Hermann and Rubatto, 2009). However, less information is available on subcontinental mantle composition that affected supercritical fluid/rock interaction resulting in cryptic metasomatism. Nevertheless, trace elements determined linked directly to deep lithospheric fluid inclusions are rarely known, however, the fluid-bearing xenoliths may contain enhanced concentration in case of several trace elements, such as U, Th, and LILE (Rosenbaum *et al.,* 1996; Scambelluri *et al.,* 2004; Malaspina *et al.,* 2006; Berkesi *et al.*, 2007; Hidas *et al.,* 2010). These facts supported the idea to determine not only the major (fluid and solid) phases, but also the trace elements linked to CO_2-rich fluid inclusions. As a consequence, fluid inclusion study is the most suitable method to obtain information and evidences on upper mantle fluid systems (Roedder, 1984; Szabó and Bodnar, 1996; Andersen and Neumann, 2001; Frezzotti *et al.,* 2002; Frezzotti and Peccerillo, 2007; Berkesi *et al.*, 2009).

As a detailed fluid inclusion study, the main aim was to determine the composition of the bulk fluid as precisely as it is possible. As a consequence, I clarified the bulk composition of the fluid phases (CO_2, H_2S and H_2O) within the inclusions (Berkesi *et al.,* 2009). By the specification of such fluid components fused silica capillary fluid inclusions were prepared and then applied. The technique itself was established and developed firstly in the USGS lab, Reston, USA according to Chou *et al.* (2008), additionaly it was adapted in France at G2R lab (Dubessy *et al.,* 2009). Many advances linked to this technique applied to fluid inclusion studies have been presented in Ding (2010). In this study the CO_2-H_2O system could be better described due to the investigation of the fused silica capillaries.

In addition, the solid (daughter) phases and their volume proportion was also analyzed and calculated by Focused Ion Beam (FIB) technique, which is one of the most promising tools in geological studies working on submicron-sized samples (e.g., Dobrzhinetskaya *et al.,* 2001; 2003; 2005; 2006; Heaney *et al.,* 2001; Lee *et al.,* 2003; 2007; Obst *et al.,* 2005; Stöckhert 2003; Wirth 2004; 2009; Dégi *et al.,* 2010). I demonstrate the applicability of the stepwise exposure of the fluid inclusions to get precise volume proportions of daughter phases. In addition, with this study we show that

within the fluid inclusions even submicron-sized phases can be efficiently studied by FIB-SEM.

With the laser ablation technique (LA-ICPMS) the trace elements that are linked to fluid inclusions and are incompatible to the host mineral could also be semi-quantified. It was also proved that CO_2-rich supercritical fluid caused cryptic metasomatism resulting in enrichment of several trace elements (e.g. MREE, Y, Ti) both in ortho- and clinopyroxene (Berkesi *et al.,* 2007). Consequently, multistage petrologic and geochemical stages have been recorded in mantle peridotites that are presented here.

2. GOALS OF THE DOCTORAL WORK

In this thesis fluid inclusions, hosted in upper mantle xenolith, have been studied in details. For this, upper mantle xenoliths from the BakonyBalaton Highland Volcanic Field, Central Pannonian Basin (Hungary) have been selected. Besides, synthetic fluid inclusions were also applied. The main aims of this study, by a combination of study on natural fluid inclusions with application of capillary inclusions, were such as:

- select the fluid inclusion-bearing xenoliths for further study on the basis of detailed petrographic observation of the peridotites
- determine the phases in the fluid inclusions and look for possibilities to quantify them
- find out the volume properties of the phases determined
- model the bulk composition of the fluid trapped at mantle
- estimate the bulk density of the trapped fluid to construct the corresponding isochor and calculate the minimum pressure conditions preserved
- reconstruct the post-entrapment processes and the fluid/host mineral reactions within the inclusions
- understand the supercritical fluid/peridotite reaction in geochemical point of view

In other words, the major goal was the comprehension of the role of fluids that have migrated at lithospheric upper mantle condition beneath the Central Pannonian Basin.

3. GEOLOGY

3.1. The geodynamic framework and major tectonic units in the Carpathian-Pannonian region

The Carpathian-Pannonian region (referred to as CPR in the followings) is geologically complex region from which the studied samples are. The CPR consists of several mountain chains, such as the Eastern Alps, the Carpathian arc and the Dinarides which surround the Intra-Carpathian Basin System, the internal part of which is commonly referred to as Pannonian Basin (Figure 1).

The Intra-Carpathian Basin System can be characterized by an extended continental crust, outcropping in several smaller internal mountains, and is filled by young sediments. Based on the Mesozoic tectonostratigraphy and structural analysis, the internal area is subdivided into two independently moving microplates (Csontos, 1995; Csontos and Vörös, 2004; Haas *et al.,* 1995; 2000; Kovács *et al.,* 2000): 1/ ***ALCAPA*** (the acronym of ALps-CArpathians-PAnnonian, i.e. northern Intra-Carpathian Basin System and Western Carpathians) and 2/ ***Tisza-Dacia*** (southern Intra-Carpathian Basin System; East and South Carpathians) (Figure 1). These units have different Mesozoic history that is proved on the basis of paleobiogeographic (Géczy, 1973; 1984; Vörös, 1993; Szente, 1995) and paleomagnetic data (e.g., Márton and Márton, 1978; Márton, 1997): the ALCAPA is of African, whereas the Tisza-Dacia block is of European affinity. The Mid-Hungarian zone (Figure 1) a narrow structural belt between Lake Balaton and the Mecsek Mts. (SW Hungary) composed of the Bükk Mts. (N Hungary), separates the aforementioned two units having distinct evolution during the Paleogene-early Miocene. It comprises low- to high-pressure metamorphic Paleozoic-Mesozoic continental margin sediments, a mélange, and dispersed remains of a Jurassic ophiolite nappe (Wein, 1969; Haas *et al.,* 2000; Csontos and Vörös, 2004). The ALCAPA unit is the northern part of the Pannonian Basin defined as the unit bound to the north by the Pieniny Klippen Belt and to the south by the Periadriatic and Balaton faults (Balla, 1984; Csontos, 1995; Fodor *et al.* 1998; 1999).

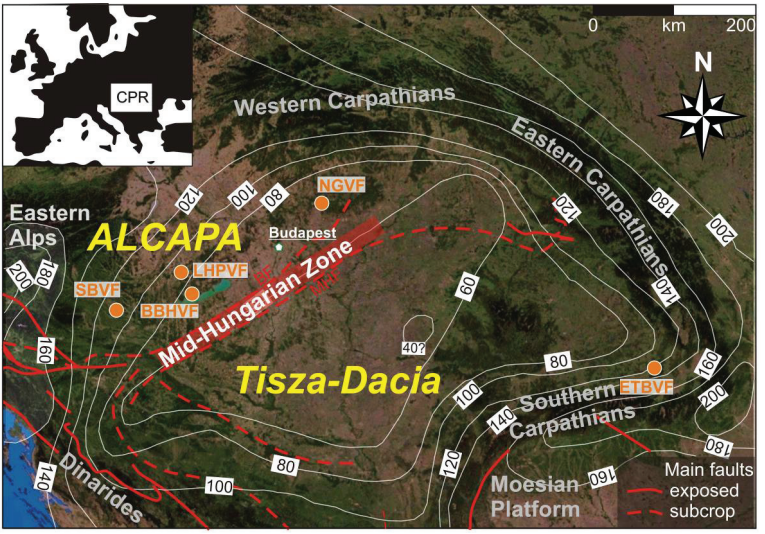

Figure 1. Schematic view of the Carpathian-Pannonian region (CPR) modified after Hidas et al (2010). The photo-map (satellite image was downloaded from GoogleEarth) shows the main tectonic units (ALCAPA and Tisza-Dacia separated by the Middle Hungarian Zone (after Csontos and Vörös, 2004; Kovács *et al.,* 2007 and references therein), the lithospheric thickness (units in km) beneath the region (after Horváth, 1993; Lenkey, 1999) and the sorrounding mountain chains. The position of the Balaton fault (BF) and the Middle Hungarian fault (MHF) is also shown. The orange spots indicate the location of the Plio-Pleistocene alkali basaltic volcanic fields hosting mantle xenoliths (e.g. Szabó *et al.,* 1995 and references therein) - BBHVF: Bakony-Balaton Highland Volcanic Field; ETBVF: Eastern Transylvanian Basin Volcanic Field; LHPVF: Little Hungarian Plain Volcanic Field; NGVF: Nógrád-Gömör Volcanic Field; SBVF: Styrian Basin Volcanic Field

The Balaton fault (abbreviated as BF on the Figure 1) separates ALCAPA from the Mid-Hungarian zone (MHZ). The major fault separating the Mid-Hungarian zone from the Tisza-Dacia unit to the south is referred to as the Mid-Hungarian (or Zagreb-Zemplin) fault (Balla, 1984; Csontos and Nagymarosy, 1998; Haas *et al.,* 2000) (abbreviated as MHF on the Figure 1). Along the northeastern MHZ, roughly east of the Danube, the Szolnok Flysch unit was thrusted and folded onto the northern edge of the Tisza block (Nagymarosy and Báldi-Beke, 1993).

3.2. The geodynamic evolution of the CPR

The CPR formed in the latest stage of Alpine orogeny, as a result of the convergence of the Adriatic and European plates. Related to the consumption of the two oceans (Penninic and Vardar), the Paleogene evolution of the Mediterranean region was determined by the northward drift and counterclockwise rotation of the Apulian microcontinent of African origin (Csontos and Nagymarosy, 1998). One of these two oceans is the Penninic ocean, located north of Apulia (Csontos 1995; Channell and Kozur 1997; Nemcok *et al.,* 1998), whereas the other one is called as the Vardar Ocean (Csontos and Vörös, 2004; Kovács and Szabó, 2008) (Figure 2). The Late Eocene collision of Apulia and the European foreland in the Eastern Alps closed the Penninic Ocean flysch basin between continental plates and resulted in a strong N-S compressional regime.

The Pannonian Basin was formed in several steps during Tertiary times. In the Paleogene the earliest tectonic phase took place as a major right lateral shearing along the Periadriatic fault (abbreviated to as PAF on Figure 2) and the Balaton fault. This shear event was initiated in the late Eocene (Fodor *et al.,* 1992) (Figure 2a); however, the main phase of shearing appears to have occurred during the Oligocene (Figure 2b). As a consequence, ALCAPA suffered extrusion, and major right lateral displacement (Kázmér and Kovács, 1985) (Figure 2), which may have exceeded up to 450 km (e.g. Tari *et al.,* 1992). Volcanic products of the Paleogene-Early Miocene period occur sporadically and silicic rocks, as thick ignimbrites were erupted along the Mid-Hungarian Zone (e.g. Szabó *et al.,* 1992, Pécskay *et al.,* 1995, Kovács and Szabó, 2008) (Figure 2).

The main driving force of such extrusion process may be the adjacent subductable oceanic or thinned continental crust at the edge of the escaping units. There are ongoing discussions to describe the mechanism of continental escape and its correlation with the roll-back type subduction. Concerning the ALCAPA extrusion, there are explanations (e.g. Royden and Horváth 1988; Csontos *et al.,* 1992; Fodor *et al.,* 1999; Huismans *et al.,* 2001; Horváth 2007) suggesting that it was extruded from the Alps as a *crustal block*. In contrast, some authors (e.g. Willingshoffer *et al.,* 1999, Willingshoffer and Cloetingh 2003; Kovács and Szabó 2008) argue that the extrusion affected the whole lithospheric column. Geochemical (e.g. Bali *et al.,* 2002, 2007, 2008a,b; Demény *et al.,* 2004) and deformation studies (e.g. Falus *et al.,* 2000, 2004, 2008) of mantle xenoliths indicate that

at least part of the lithospheric mantle was extruded together with the crust of the ALCAPA, therefore, supporting the later model. In addition, Kovács and Szabó (2008) suggest that an E-W directed hot mantle flow forced the ALCAPA (and Tisza-Dacia to a smaller extent) unit to escape from the southern neighborhood of the Eastern Alps together with its lithospheric mantle. In addition, the mantle flow may have enhanced the steepening and retreating of the subducting Magura slab. The Outer Carpathian flysch basins (i.e., part of the "sensu strictu" Penninic ocean), which were opened by Jurassic-Early Cretaceous rifting (Csontos, 1995), with weakened lithosphere served as such "free space" (Horváth, 1988), which could be later occupied by the escaping ALCAPA and Tisza-Dacia blocks (Csontos, 1995).

The next tectonic phase was dominated by opposite rotations of the ALCAPA and Tisza-Dacia microplates within the CPR (Márton, 1987; Csontos *et al.,* 1992). The two tectonic units of the Pannonian Basin have been finally assembled in the Middle to Late Miocene (e.g. Márton and Márton, 1978, Balla, 1984, Csontos *et al.,* 1992, Kovač *et al.,* 1994) (Figure 2c and d). Based on paleomagnetic data, the two microplates were detached from their southern neighbor, the Dinarides, and were pushed or rotated into the Carpathian embayment during the early Miocene (ca. 20-18 Ma) (Figure 2b). Fodor *et al.,* (1999) have found that the ALCAPA and Tisza-Dacia units rotated in opposite directions (counterclockwise and clockwise, respectively) and extended northeastwards from the Ottnangian (18–17 Ma) until the Sarmatian, when the collision of the ALCAPA unit (~12 Ma) and the European foreland took place (Figure 2c and d).

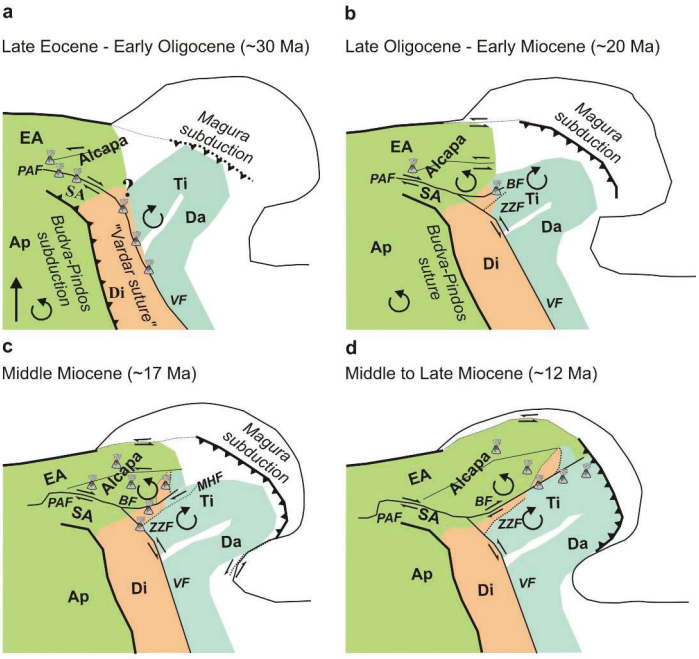

Figure 2. Modified figure after Kovács and Szabó (2008), showing a model for summarizing the geodynamic evolution of the main tectonic units, subduction zones, sutures and faults in the Carpathian-Pannonian region from the late Eocene from a „mantle perspective". Abbreviations: EA: Eastern Alps, SA: Southern Alps, Ti: Tisza, Da: Dacia, Di: Dinarides, Ap: Apulian indenter; for tectonic lines—PAF: Periadriatic fault, BF: Balaton fault, MHF: Middle-Hungarian fault, ZZF: Zagreb-Zemplén fault, VF: Vardar fault.

The roll-back type subduction along the Carpathian front continued following the extrusion of the ALCAPA and Tisza-Dacia units (pre-rift phase). It was accompanied by the formation of voluminous calc-alkaline rocks along the subduction front (Szabó *et al.,* 1992; Harangi, 2001). The stress field generated by the subduction rollback resulted in large-scale block movements and extension. With respect to the basin formation the last major tectonic phase was the extension in the CPR. The extension period can be divided into two major phases (e.g., Fodor *et al.,* 1999; Huismans *et al.,* 2001).

The earlier phase of the extension period (Tari *et al.,* 1992) with high subsidence rates took place in the Karpatian to Early Badenian (ca. 18-14 Ma). The key factor is the active asthenospheric upwelling, therefore, this phase is commonly regarded as the 'active' extensional period. Rapid uplift of metamorphic core complexes and associated high angle normal faults were formed at this time. Meanwhile, opening of thin-skinned, strike slip basins (e.g. Vienna and East Slovakian Basins) took also place. NE-SW tension directions (Fodor *et al.,* 1999) were characteristic, furthermore, the thinning factor is thought to be nearly the same for both the crust and the mantle (Huismans *et al.*, 2001). Another main geodynamical feature of this extensional phase is nappe thrusting in the Outer Carpathians, whereas nappe formation had already closed down at the western part of the Carpathians (e.g., Royden 1988; Csontos *et al.,* 1992). Also, during the Karpatian tectonic events basin openings of the Little Hungarian Plain (Tari, 1994) and Hód-Békés (Győrfy and Csontos, 1994) are characteristic. Besides, rare ultrapotassic (Harangi *et al.,* 1995) and some Middle Miocene calc-alkaline volcanites of the Northern Pannonian Basin (Szabó *et al.,* 1992, Konečnỳ *et al.,* 1995) are related to this extensional period. The considerable thinning of the lithosphere relates to the first phase of extension. It is important to note that in contrast to previous models (e.g. Szabó *et al.,* 1992, Harangi, 2001), suggesting a southward-dipping subduction of European lithosphere beneath the ALCAPA microplate along the Western Carpathians being responsible for the chemical characteristics seen in middle Miocene volcanic rocks, Kovács *et al.,* (2007) and Kovács and Szabó (2008) proposed a new model. These authors believe that the subduction-related geochemical characteristics in Tertiary calc-alkaline igneous rocks and mantle xenoliths from the Bakony-Balaton Highland, close to the Middle Hungarian Zone, are inherited from an earlier subduction event (either the Budva-Pindos or Vardar Ocean during the Mesozoic–Paleogene). This previously

metasomatized mantle was extensively melted as a result of considerable thinning of the lithosphere during the first phase of extension in the middle Miocene (Harangi *et al.,* 2007, Kovács and Szabó, 2008).

The later, second 'passive' extensional episode (ca. 12-8 Ma) was due to the collapse of the asthenospheric dome (e.g., Bada and Horváth, 2001). This tectonic phase is considered to be driven by the westward subduction of the European margin beneath the internal Carpathian area (Horváth, 1993; Jolivet and Faccenna, 2000) and an eastward directed asthenospheric flow could be also an additional driving force (Kovács and Szabó, 2008). The rotation of major tension direction changed from SE-NW to E-W (Fodor *et al.,* 1999) due to fixation of the subduction front in the northwesternmost part of the Carpathians. The central part of the Pannonian Basin was the most intensively affected by this extensional event. In contrast to the previous period, the extent of thinning was not the same for the crust and the mantle according to the thinning factors of Huismans *et al.,* (2001): the mantle lithosphere was more affected in comparison to the crust (thinning factor of the crust: $\beta = 1.1$, whereas thinning factor of the mantle: $\delta = 4–8$). Several seismic sections show the end of the rifting phase in the western parts of the Pannonian Basin (Tari, 1994). Volcanic products of this period composed of large volumes of calc-alkaline rocks located along the Carpathian arc (Szakács and Seghedi, 1995).

The Sarmatian collision of the ALCAPA and later the Tisza-Dacia units (11–8 Ma) with the European foreland led to a compression event. The Post-Sarmatian tectonic inversion (e.g. Csontos *et al.,* 1992) can be regarded as the end of extension in the Pannonian Basin. The Sarmatian-Pontian period is considered to be the thermal cooling phase of the Middle Miocene rifting (Horváth and Royden, 1981). In the late Sarmatian inversion in the basin system can be observed. Most of the basin system is characterized by tectonic subsidence. The Sarmatian erosional event is explained by the combination of an increase in the intraplate compressional stress (Horváth and Cloetingh, 1996) and global sea level fall at the end of the Sarmatian (Vakarcs *et al.,* 1994). The Pannonian was characterized by post-rift subsidence, as indicated by widespread and thick Pannonian sediments, often onlapping the pre-Miocene basement (Csontos, 1995). The basin system was filled up by the end of the Pontian by sediments provided by large delta system.

It is important to note, that there is, however, another idea for the driving force of the extension process in the Intra-Carpathian System. On the basis of the model of Gemmer and Houseman (2007), the subduction as a key process beneath the Carpathian can be excluded. Instead, the gravitational instability promoted by collision-induced crustal thickening may explain simultaneous extension and convergence and depth-variable thinning of the lithosphere beneath the Pannonian Basin.

To summarize, eastward escape of the orogenic lithosphere block from the Alpine collision zone, followed by extensional collapse and the retreat accompanied by active pull of the Eastern Carpathian subduction zone via subduction roll-back are considered to be responsible for the formation of the Pannonian Basin. As a consequence, the area is now characterized by an anomalously thin lithosphere (~60 km) (Horváth, 1993; Bada *et al.,* 2007; Tašárová *et al.,* 2009) (Figure 1). Seismic studies (e.g., CELEBRATION 2000, Grad *et al.,* 2006; Janik *et al.,* 2011) showed that, with the exception of the Transdanubian Central Range, the basin system is characterized by 30-22.5 km crustal thickness being the thinnest in the central part of the basin and thickening towards the margins (Figure 1). The anomalously thin crust is suggested to be the result of Neogene extension (e.g. Horváth, 1993).

3.3 The xenolith-bearing alkali basaltic volcanism

Peridotite and/or granulite xenolith-bearing volcanic fields occur in Late Miocene–Quaternary mafic volcanic rocks the found in the Intra-Carpathian Basin System either at the edge [Styrian Basin Volcanic Field (SBVF), Nógrád-Gömör Volcanic Field (NGVF) and Eastern Transylvanian Basin Volcanic Field (ETBVF)] or in its central part [Little Hungarian Plain Volcanic Field (LHPVF), Bakony-Balaton Highland (BBHVF) (Figure 1) (e.g., Embey-Isztin *et al.,* 1989; Szabó *et al.,* 2004 and references therein). The volcanism began first (10-12 Ma) in the western part of the CPR (e.g. Balogh *et al.,* 1986, Balogh and Pécskay, 2001). It culminated in all volcanic fields at 2-5 Ma. The volcanism can be classified as post-extensional volcanic activity (Embey-Isztin and Dobosi, 1995; Harangi, 2001) and was generated as decompression melt due to the upwelling of asthenospheric material. According to Embey-Isztin *et al.* (1993), in the LHP and in the BBH olivine tholiites, alkali basalts and basalts, in the SB nephelinites,

whereas in the NG and ETB basanites are found. Major element composition of the mafic melts implies that they represent mantle derived primary magmas (Embey-Isztin *et al.,* 1993). Partial melting occurred at 80 – 100 km mantle depth, in the garnet stability zone (Embey-Isztin and Dobosi 1995; Harangi *et al.,* 1995). Trace element compositions indicate subduction related component in the source region of most of the magmas (e.g. Downes *et al.,* 1995; Harangi 2001, Gméling *et al.,* 2007). In the followings, the Bakony-Balaton Highland will be on focus as the studied samples have been collected from this area.

The BBH is located in one of the subunits of ALCAPA, called Transdanubian Central Range unit. Its pre-Cenozoic lithology correlates with that of Upper Austroalpine nappes in the east Alpine orogen (Kázmér and Kovács, 1985; Tari, 1991). The underlying basement of the volcanic field consists of Paleozoic rocks (Silurian schist, Permian red sandstone – Császár and and Lelkesné-Felvári, 1999) and a thick Mesozoic carbonate sequence (Haas *et al.,* 1999), all of these were previously deposited on the Alpine units (SW from their present location) and were transported towards east-northeast via the escape and extrusion of the ALCAPA microplate (Figure 2).

The volcanism of the BBH, according to $^{40}Ar/^{39}Ar$ measurements, was active between 7.96 Ma and 2.61 Ma (Figure 3) (Balogh *et al.,* 1982; Borsy *et al.,* 1986; Balogh and Pécskay, 2001; Balogh and Németh, 2005; Wijbrans *et al.,* 2007) and produced mostly alkali basaltic volcanic rocks (Szabó *et al.,* 1992; Embey-Isztin, 1993). Precisely, the Tihany and Hegyestű volcanoes were formed in the first period around 7.9–8.0 Ma, while the rest of the volcanic centers were active in the second period: 5.5–2.6 Ma (Wijbrans *et al.,* 2007). The BBH itself has approximately 50 basaltic volcanoes in a relatively small area (~3500 km^2), however the number of vents maybe far more than 50 due to the existence of volcanic complexes and nested volcanoes (Martin *et al.,* 2003). The alkali basaltic volcanism in the western Pannonian Basin was of a predominantly subaerial, intracontinental type. However, large shallow water bodies may have been present during eruptions, which most likely led to the formation of emergent volcanoes (Kokelaar, 1983; White and Houghton, 2000). After volcanism ceased, fluvial/alluvial sedimentation was widespread in the western Pannonian Basin and major erosion affected the BBH, too (Németh *et al.,* 2003). All types of eroded volcanoes can be found in the western Pannonian Basin, including the BBH, where the most prominent

geomorphologic formations are the circular, lava-capped buttes. These centers are usually related to phreatomagmatic volcanoes, such as maar structures and tuff rings (Németh *et al.,* 2003). Lake Balaton is a recent landform and its history dates back only 17 000-15 000 years (Csernyi and Corrada, 1989; Tullner and Csernyi, 2003).

3.4. Petrography and geochemistry of upper mantle xenoliths

Up to now, the ultramafic peridotite xenoliths were found from six locations in the BBH, namely from Tihany, Bondoró, Füzestó, Szentbékkálla, Mindszentkálla and Szigliget. The petrography of these xenoliths reveals a high variety of the rock types, as well as the textures. Most of the xenoliths are spinel lherzolites, representing residual material of the mantle with complex history. However, harzburgite, clinopyroxenite, orthopyroxenite, wehrlite, websterite and sometimes composite xenoliths appear, too. From the matter of the texture, the vast majority of the studied xenoliths are equigranular, besides, in lesser amount protogranular and porphyroclastic types were also described (Embey-Isztin *et al.,* 1989; Downes *et al.,* 1992; Downes and Vaselli, 1995; Szabó *et al.,* 1995; 2004). Subsequently poikilitic (Berkesi *et al.,* 2007), flattened equigranular (Hidas *et al.,* 2007) and milonitic (Falus et al., 2004) textured xenoliths also present in highly different portion on locations. In the BBH, an unusual quartz-bearing orthopyroxene-rich websterite xenolith has been found in an alkali basaltic tuff at Szigliget. These kind of xenoliths are of great importance as they are interpreted to represent a fragment of an orthopyroxene-rich body that crystallized in the upper mantle from a hybrid melt that formed by interaction of mantle peridotite with a quartz-saturated silicate melt that was released from a subducted oceanic slab (Bali *et al.,* 2008). The study of another two orthopyroxene-rich olivine websterites from the same region (Bali *et al.,* 2007), in addition, revealed material formed from Mg-rich silicic (boninitic) melts at mantle depths.

The peridotite xenoliths from alkali basalts of the Bakony-Balaton Highland have a bulk compositions ranging from 37 to 45 wt.% MgO, 1.0 to 3.5 wt.% CaO, and Al_2O_3, and 0.02 to 0.14 wt.% TiO_2. There are no significant chemical differences of xenoliths among the major localities, although the compositional range of the Nógrád-Gömör Volcanic Field covers the highest MgO-bearing xenoliths, whereas ranges of the Styrian

Basin and Eastern Transylvanian Basin Volcanic Fields xenoliths involve samples containing the lowest MgO content. Concentration of basaltic elements, representing Al_2O_3 and TiO_2, and of CaO displays a negative correlation with MgO as Downes and Vaselli (1995) have already noted. These chemical features of the Carpathian-Pannonian Region xenoliths are in agreement with xenoliths from other localities (e.g., Rhenish Massive, Massif Central) and with alpine massive peridotites (Bodinier *et al.,* 1988; Downes *et al.,* 1991; Wilson and Downes, 1991). It is suggested that gradual depletion in basaltic elements is connected at first consideration to partial melting event(s). The most frequent mineral is olivine in these xenoliths with mg# and Fo content between 89 and 92 along with low CaO-content (0.04-0.11 wt.%). Al_2O_3 content of orthopyroxenes is generally higher in protogranular xenoliths than porphyroclastic or equigranular ones. In most cases, clinopyroxene is Cr-diopside with mg# between 89 and 93. The spinel composition is the most variable with cr# between 10 and 55 and mg# between 80 and 60 (Embey-Isztin *et al.,* 1989; Downes *et al.,* 1992; Szabó *et al.,* 1995). Additional mineral phase can be pargasitic amphibole (Embey-Isztin, 1976; Bali *et al.,* 2002; Szabó *et al.,* 2004). The clinopyroxenes from protogranular xenoliths from the Bakony-Balaton Highland are LREE depleted which is characteristic for undeformed subcontinental lithospheric mantle, whereas porphyroclastic and equigranular textured xenoliths contain clinopyroxenes that are LREE enriched. This enrichment could be the result of a metasomatic event related to deformation (Downes *et al.,* 1992). The $^{87}Sr/^{86}Sr$ values of separated clinopyroxenes from Bakony-Balaton Highland xenoliths vary between 0.70307 and 0.70523, the $^{143}Nd/^{144}Nd$ ratio ranges from 0.513341 to 0.512733. The εNd values of clinopyroxenes from protogranular xenoliths are the highest, whereas porphyroclastic and equigranular xenoliths show lower values. Clinopyroxenes from protogranular xenoliths have high Sm/Nd and $^{143}Nd/^{144}Nd$ values, whereas equigranular samples show lower values. The heterogeneity might be the result of a three-component mixing where the end members are: LREE depleted, high εNd low εSr mantle; Pliocene alkali basalts and Miocene calc-alkali magmas (Downes *et al.,* 1992).

The equilibrium temperature of BBH mantle xenoliths is between 880 and 1090 °C. Protogranular textured peridotites have the highest and equigranular xenoliths have the lowest equilibrium temperatures (Embey-Isztin *et al.,* 1989; Downes *et al.,* 1992; Szabó *et al.,* 1995; 2004; Bali *et al.,* 2002; 2007).

3.5. Previous fluid inclusion studies on BBH xenoliths

On the basis of previous studies, fluid inclusions trapped prior to the upbringing by the alkali basalt are filled by high density CO_2-rich fluid (Bali *et al.,* 2008). Szabó and Bodnar, (1996) have also worked on fluid inclusions that might have trapped during the uplift, nonetheless, the same conclusion about the CO_2-dominance has been drawn. These latter inclusions have lower fluid density and show clear secondary feature.

In two amphibole-bearing spinel lherzolite xenoliths from Szigliget the presence of coexisting fluid and silicate melt inclusions, trapped as primary inclusions in clinopyroxene rims and as secondary inclusions along healed fractures in orthopyroxene have been observed (Hidas *et al.,* 2010). It was confirmed that the parental melt for both silicate melt and fluid inclusions was the same and suggested that the trace element content of the CO_2-rich end-member (containing some dissolved melt) resulted from high P–T immiscibility in deep lithospheric environments and is controlled by the trace element content of the parent silicate melt (Hidas *et al.,* 2010)

3.6. Sampling

3.6.1. The Tihany Maar Volcanic Complex

The Tihany Maar Volcanic Complex (TMVC) represents the earliest (7.96 ± 0.03 Ma, Wijbrans *et al.,* 2007) volcanic products of post-extensional alkaline basaltic volcanism in the BBH. The studied xenoliths were collected from the maar-type rocks at "Szélfútta cliffs" (Figure 3b). In Tihany Maar Volcanic Complex numerous xenoliths occur representing the lithospheric upper mantle (peridotites), the lower crust (granulites) and most probably the crust/mantle boundary (pyroxenites) (Falus and Szabó, 2004, Hidas, 2006), however, there are lesser xenoliths compared to that of other well-known xenolith localities in Bakony-Balaton Highland Volcanic Field (e.g.: Szentbékkálla, Szigliget; Bondoró: Embey-Isztin *et al.,* 1989; Downes *et al.,* 1992; Szabó *et al.,* 2004; Bali *et al.,* 2007, 2008). The collected peridotite xenoliths are hosted in well-exposed maar sediment, sampled by the same eruption event, with average size 1–3 centimeter, in some cases the grain size is 5 mm. Their shape is either irregular or rounded some of them are

altered. From 16 petrogaphically studied xenoliths nine, the freshest xenoliths have been selected for detailed geochemical study, providing a representative series (Tih 0304, Tih 0305, Tih 0310, Tih 0501, Tih 0503, Tih 0504, Tih 0506, Tih 0507, Tih 0509) for Tihany peridotites (Table 1).

3.6.2. Szentbékkálla

The phreatomagmatic volcanism (Martin and Németh, 2004) was active from approximately 4.53 Ma (Wijbrans *et al.,* 2007). The lapilli tuff contains a high proportion of semi-rounded to rounded gravel-like ultramafic xenoliths, broken olivine and clinopyroxene xenocrysts without any systematic accumulation pattern (Martin and Németh, 2004). The juvenile fragments of the lapilli tuffs and tuffs from Szentbékkálla are usually ranging from tephrite through phonotephrite to tephriphonolite (Németh and Martin, 1999). Small, altered, light colored glass shards show dacite/trachydacite and basaltic andesite composition (Németh and Martin, 1999).

At this locality a large amount of upper mantle peridotites, pyroxenites and granulites has also been found (Bali *et al.,* 2007, 2008). Usually, the peridotites are coarse grained and equigranular or porphyroclastic, rarely protogranular in texture. A pyroxenite-veined peridotite xenolith has been found hosting large amount of fluid inclusions, which was selected for fluid inclusion studies in this work (sample name: Szb 0311).

Figure 3. A - Schematic geological map of the Bakony–Balaton Highland Volcanic Field (enlarged) modified after Jugovics (1968), Harangi (2001). The Ar/Ar age of the volcanism in the study area is indicated by number (Wijbrans et al., 2007).
Figure 3. B - Simplified geological map of the Tihany peninsula showing the position of volcano-sedimantary rocks, modified after Németh et al., (2001). Dashed line: inferred positon of maar crater rim, red diamond: location of sampling. Abbreviations: CM - Central Maar, EM - Eastern Maar, WM - Western Maar

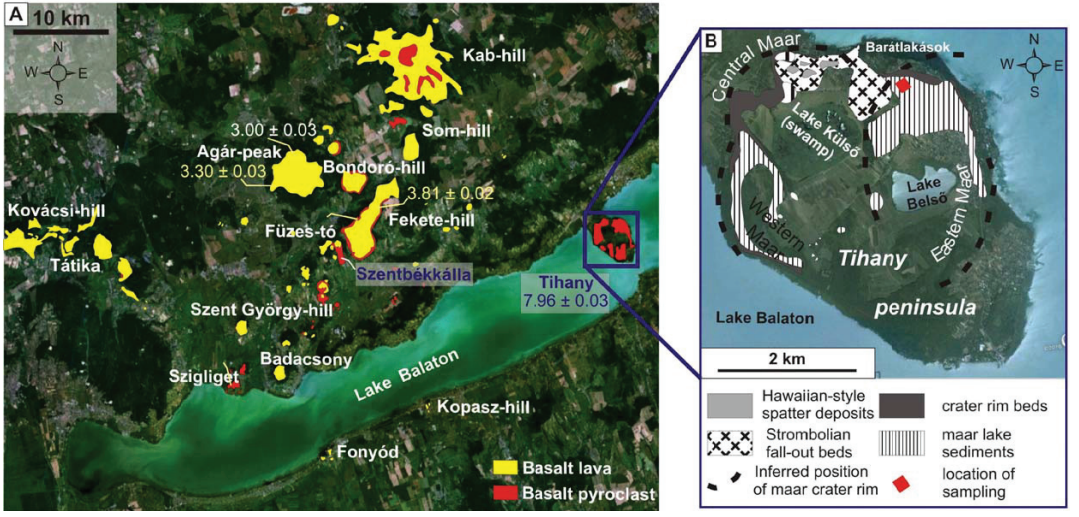

4. APPLIED TECHNIQUES ON THE NATURAL SAMPLES

From the selected xenoliths 100-130 μm thick sections were prepared and polished on both side for the best visibility.

4.1. Microscopes for petrographic observation

Petrographic observations were performed on a Nikon SMZ 800 stereomicroscope and on a Nikon Eclipse LV100POL polarizing microscope equipped with Nikon DS-Fi1 digital camera and NIS Elements AR 2.20 digital imaging software at the Lithosphere Fluid Research Lab, Eötvös University Budapest (Budapest, Hungary). The modal composition of the rock samples was evaluated by digital image analysis on high resolution photomicrographs of the whole thin sections using Corel X4 software package.

Backscattered imaging of the exposed fluid inclusions was performed on an AMRAY 1830 I/T6 type scanning electron microscope equipped with Microspec WDX (Department of Petrology and Geochemistry, Eötvös University Budapest, Hungary) and on JEOL Superprobe JXA-8200 scanning electron microscope at Bayerisches Geoinstitut, Bayreuth, Germany. Accelerating voltage, beam current and beam size were 20 kV, 1-2 nA and 2-7 μm, respectively.

4.2. Electron microprobe analysis (EMPA)

The major elements of the rock-forming minerals in Szentbékkálla peridotite were analyzed by JEOL Superprobe JXA-8200 at the Bayerisches Geoinstitut. Analyses were carried out with an accelerating voltage of 15 kV, beam currents of 10 and 20 nA and beam sizes of 10 and 5 microns. The counting time for each element was 20 s. Natural and synthetic silicate and oxide standards were used for calibration and ZAF correction was applied.

The constituent minerals of Tihany peridotites have been analyzed for major elements by CAMECA SX-100 electron microprobe (EMPA) at the University of Vienna (Austria) and at the Open University (United Kingdom). The accelerating voltage was set to 20

kV, with 10 and 20 nA probe current and a beam size of 5 and 10 μm for all analyses at University of Vienna and Open University, respectively. The counting time was 40 s for each element. Natural standards were used for the analyses and ZAF correction was applied.

4.3. Heating - freezing experiments – microthermometry

Microthermometry of the natural fluid inclusions was performed using FLUID INC. type USGS heating-freezing gas flow stage at the Lithosphere Fluid Research Lab (LRG), Eötvös University, Budapest; and on Linkam MDS 600 heating-freezing stage at the laboratory "Géologie et Gestion des Ressources des Minérales et Energétiques" (G2R Laboratory), Faculty of Science, University Nancy 1, France. All stages were calibrated on the melting points of CO_2 (-56.6 ºC, Span and Wagner, 1996) and the H_2O (0.0 ºC, Fisher, 1976), the eutectic point of the system H_2O-NaCl (21.2 ºC, Knight and Bodnar, 1989) and the critical temperature of H_2O (373.9 ºC at 22 MPa, Fisher, 1976) points of synthetic CO_2, H_2O, CO_2-H_2O and H_2O-NaCl fluid inclusions. As a result of the calibration, the accuracy of the microthermometric measurement is ±0.2 ºC. The fluid inclusions were cooled below -100 ºC for complete freezing and then were slowly heated until visible total homogenization. Melting and homogenization temperatures were recorded at least twice for each fluid inclusion to reduce artificial deviations. In those cases when the homogenization temperature was detected below 9.9 ºC (melting of CO_2 gas hydrate; Diamond, 2001) the inclusions were heated until 15 ºC too see if there is visible clathrate melting at this particular temperature. Both the densities and the minimum pressure values have been calculated using the FLUIDS software package (Bakker, 2003).

4.4. Raman microspectroscopy on natural fluid inclusions

For the Raman analyses of the glass-hosted bubbles, a Jobin Yvon confocal Labram HR (high resolution), at G2R laboratory, Nancy University, was applied using a frequency-doubled 457nm Nd-YAG laser with holographic edge filter. The laser power

at the laser source was set to 200 mW, spectra were taken applying a 20LWD (long working distance) or 80x objective lens. The spectral resolution was set <0.5 cm^{-1} using the grating of 1800 grooves per mm.

Fluid inclusions were analyzed by Raman spectrometer in two different laboratories using different instruments and analytical settings. At Budapest University of Technology and Economics (Hungary), a Jobin Yvon confocal Labram Raman instrument with using frequency-doubled Nd-YAG laser with an excitation wavelength 532 nm, 50 mW and 20 mW laser energy at laser source and at sample surface, respectively. A 50× objective was used.

At G2R Laboratory a Dilor® Labram-type Raman spectrometer with edge filter, 514 nm Ar^{+} laser, 200 mW laser power at the laser source and ~80 mW at the sample surface and 80× objective was applied. The analytical settings included a 200-500 μm confocal hole, 200 μm spectral slit, 600 or 1800 g/mm spectrograph gratings, 2-10× accumulations and 2-150 sec acquisition time (all depending on the maximum intensity). The spectral resolution of the measurements varied with wave number but was under 2 cm^{-1} choosing grating of 1800 grooves per mm. For detecting small amounts of water the method of Berkesi *et al.,* (2009) was used.

The heating experiments compiled with Raman microspectroscopy (see later) have been carried out at G2R laboratory, Nancy University. To characterize the phases on the Raman spectra, the online Raman databases of the French Society of Mineralogy and Crystallography (http://wwwobs.univ-bpclermont.fr/sfmc/ramandb2/index.html) and that of Bonelli and Frezzotti (2003, http://www.dst.unisi.it/geofluids/raman) was applied. Raw data were processed using LabSpec v5.25.15 software designed for Jobin-Yvon Horiba LabRam instruments.

4.5. LA-ICP-MS analyses

The trace element composition of the rock-forming minerals of the Tihany peridotites and the semiquantitative composition of fluid inclusions was determined by laser ablation inductively coupled plasma mass spectrometer (LA-ICP-MS) with an Agilent 7500ce octopol spectrometer (ORS) and GeoLas laser ablation system (Department of

Geosciences, Virginia Tech, USA) using 193 nm ArF laser beam, 103 Pa vacuum, 1.2 l/min He-flow with 10-50 μm spot size, 0.01 s dwell time, 5 Hz repetition rate and 150 mV output energy. Trace elements in the phases in the Szentbékkálla sample has been analyzed by excimer laser (ArF, 193nm) and an Agilent 7500c quadrupole ICP-MS, equipped with an octopole reaction cell using H_2 gas at the G2R laboratory, Nancy1 University Nancy, France. Helium flow is always 0.5 l/min for all different types of samples analyzed. The collision-reaction cell flowed with 2.5 ml/min of H_2 (to eliminate $^{40}Ar^+$ interferences on $^{40}Ca^+$) 44-60 μm spot size, 0.01 s dwell time, 5 Hz repetition rate and 10 J/cm².

In both labs NIST SRM 610 was used for external standardization. Data processing was carried out by the AMS data analyses software (Mutchler *et al.,* 2008) and by SILLS (Guillong *et al.,* 2008) on the Tihany samples, whereas by Longerich (Longerich *et al.,* 1996) calculation method on the Szentbékkálla xenolith (software used: L.A.S.P. developed by Mathieu Leisen at G2R lab, Nancy, France). Beam size was greater than the fluid inclusions (>10 μm) to sample the entire inclusion plus some of the host immediately around the inclusion. In microscopic view, no crystal and/or silicate melt inclusions were observed other than the studied fluid inclusions in the ablation volume. Since neither the C nor the O, that are the major constituent atoms of the ablated fluid, can be determined by using laser ablation techniques. Direct information on trace elements associated to fluid inclusions is able to obtain solely on signal intensity versus time plot with progressing analysis**.** Each analysis started with monitoring of the blank for about 50-60 seconds. The first section of the ablation signal, until the inclusion is ablated, corresponds to host mineral. As the inclusion is reached, mixed material from the host and the inclusion are analyzed simultaneously in an unknown proportion. When the entire inclusion is ablated, element ratios are again identical to those of the pure host and the analysis is stopped (Halter *et al.,* 2002). Semi-quantitative trace element ratios for the fluid inclusions have been calculated by using the method of Hidas *et al.,* 2010.

For the Tihany peridotites data were collected for the following masses: ^{23}Na, ^{25}Mg, ^{27}Al, ^{29}Si, ^{39}K, ^{40}Ca, ^{49}Ti, ^{52}Cr, ^{56}Fe, ^{58}Ni, ^{85}Rb, ^{88}Sr, ^{89}Y, ^{90}Zr, ^{93}Nb, ^{138}Ba, ^{139}La, ^{140}Ce, ^{143}Nd, ^{147}Sm, ^{153}Eu, ^{172}Yb, ^{175}Lu, ^{178}Hf, ^{208}Pb, ^{232}Th and ^{238}U. For the Szentbékkálla xenolith two methods were used: a/ no gas mode: Data were collected for the following masses: ^{24}Mg, ^{28}Si, ^{39}K, ^{43}Ca, ^{44}Ca, ^{89}Y, ^{90}Zr, ^{93}Nb, ^{139}La, ^{140}Ce, ^{146}Nd, ^{147}Sm, ^{153}Eu,

^{163}Dy, ^{165}Ho, ^{166}Er, ^{172}Yb, ^{175}Lu, ^{178}Hf, ^{181}Th and ^{238}U. b/ H2 in reaction cell: Data were collected for the following masses: ^{24}Mg, ^{28}Si, ^{39}K, ^{40}Ca, ^{45}Sc, ^{47}Ti, ^{51}V, ^{53}Cr, ^{56}Fe, ^{59}Co, ^{60}Ni, ^{63}Cu, ^{85}Rb, ^{88}Sr, ^{133}Cs, ^{138}Ba, ^{208} Pb, ^{232}Th

4.6. Focused Ion Beam (FIB) technique coupled with SEM-EDX

FIB-SEM measurements were carried out in a FEI QUANTA 3D FIB-SEM apparatus having both secondary and backscattered electron detector together with silicon drift (SDD) x-ray energy dispersive detector, operating at the Eötvös University, Budapest. Identification of these phases were mostly based on the morphology on SEI (secondary electron image), the brightness on the BSE (backscattered electron) images and on the EDS spectra. Latter one have been taken at 10-15 kV (depending on their size and elements of interest) and 0.46 – 2 nA, which allowed to detect major elements in the daughter phases from carbon through oxygen to barium. Because of the small size of the solid samples, signals detected by EDS detector are a kind of mixed signals, as x-ray from the adjacent area is also detected. To better distinguish the daughter phases from the signals of the host mineral, EDS control spectra from the host mineral were also taken in the proximity and from the same depth of the solid phases after each spectra.

5. PETROGRAPHY

5.1. Tihany peridotites

5.1.1. Xenolith petrography

Modal composition and texture types of the studied peridotites from Tihany are summarized in Table 1. The studied xenoliths are orthopyroxene-rich spinel lherzolites and spinel harzburgites, composed of only anhydrous silicates (olivine, orthopyroxene, clinopyroxene) and spinel. Orthopyroxene/clinopyroxene ratio is ranging from 1.9 to 16.7 (6.8 in average) that exceeds the average subcontinental lithospheric value of around 2 (Griffin *et al.,* 1999; Downes, 2001). Due to the small size of the xenoliths and their rarity in the locality, the modal composition might not be representative for the whole lithospheric column. It seems that the peridotites studied contain unusually large amount of orthopyroxene (Figure 4a and b).

The average grain size of minerals in the peridotites studied is also coarser than that of the peridotites of the other BBH localities: the fabric is dominated by 1-5 mm large orthopyroxenes and 2-4 mm sized olivines. In contrast, clinopyroxenes and spinels are generally small with their 40-300 μm and 20-100 μm size, respectively. Distribution of orthopyroxenes within the texture is heterogeneous, because they occur as clusters having curvilinear grain boundaries (Figure 4c and d). The coarse grained orthopyroxenes enclose euhedral or subhedral olivine (50-500 μm) as crystal inclusion (Figure 4e and f). Subhedral olivines can rarely be enclosed in large clinopyroxenes, too. Furthermore, spinel can be present either as anhedral/subhedral crystal inclusion enclosed in the silicates or as an interstitial phase. Therefore, the texture type is addressed as poikilitic throughout this study (e.g. Embey-Isztin; 1984, Embey-Isztin *et al.,* 1989; Xu *et al.,* 1998).

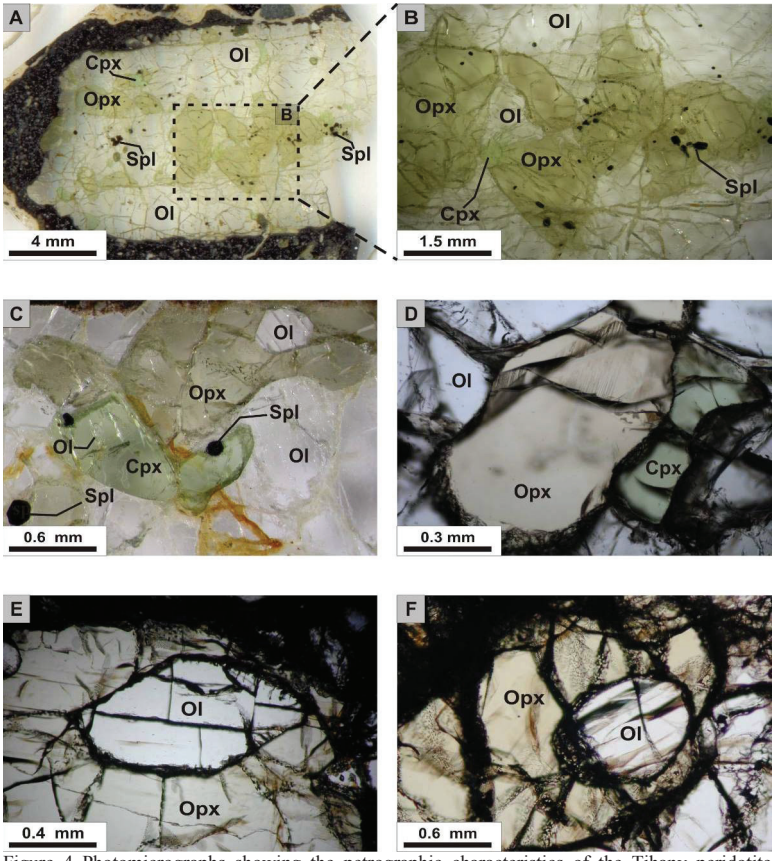

Figure 4 Photomicrographs showing the petrographic characteristics of the Tihany peridotite series. A) and B) coarse-grained orthopyroxene-rich xenolith indicating that the orthopyroxenes occur mainly in clusters together with lesser clinopyroxene. Sample: Tih0504, stereomicroscopic view. C) typical petrographic feature observed in Tihany peridotites. The dominant orthopyroxene occurs together with the clinopyroxene. Spinel can be mainly found as crystal inclusions, moreover, euhedral and subhedral olivines both in ortho- and clinopyroxene have been found. Sample: Tih0506, stereomicroscopic view. D) The dominant orthopyroxene occurs together with clinopyroxene. Sample: Tih0506, plane polarized light, 1N. E) euhedral olivine and F) subhedral olivines as a crystal inclusions hosted in orthopyroxenes. Sample: Tih 0509 and Tih 0504 at the picture E) and F), respectively. Note that on both pictures late-stage fluid inclusion assemblage is found across the orthopyroxene and the olivine. Plane polarized light, 1N. Abbreviations: Ol - olivine, Opx - orthopyroxene, Cpx - clinopyroxene, Spl – spinel.

Sample	Modal percentages				Opx/Cpx	Rock type	Texture	Av. grain size (mm)	T (°C)	Classification
	Ol	Opx	Cpx	Spl						
Tih 0304	72.6	22.6	3.8	0.9	6	harzburgite	cg-poikilitic	1.2 – 1.5	955	NOFLUID
Tih 0305	81.7	11.1	5.9	1.3	1.9	lherzolite	cg - poikilitic	~ 1.0	989	NOFLUID
Tih 0310	85.6	10.1	2.4	1.9	4.2	harzburgite	cg-poikilitic	1.5 – 2.5	1070	FLUIDRICH
Tih 0501	63.3	29.8	5.5	1.4	5.4	lherzolite	cg-poikilitic	1.0 – 1.5	1015	NOFLUID
Tih 0503	68.1	25.8	5.3	0.9	4.9	lherzolite	cg-poikilitic	0.4 – 0.6	1005	NOFLUID
Tih 0504	72.4	24.4	2.3	1	10.6	harzburgite	cg-poikilitic	2.0 – 3.0	925	FLUIDPOOR
Tih 0506	72.4	24.5	2.6	0.6	9.4	harzburgite	cg-poikilitic	2.5 – 3.0	1015	FLUIDPOOR
Tih 0507	55.1	41.8	2.5	0.6	16.7	harzburgite	cg-poikilitic	2.0 – 2.5	1150	FLUIDRICH
Tih 0509	58.5	26.3	12.4	2.8	2.1	lherzolite	cg-poikilitic	2.0 – 2.5	1165	FLUIDRICH

Table 1 Modal composition, rock type (after Streckeisen, 1976) and texture, equilibrium temperature based on two-pyroxene thermometer (Brey and Köhler, 1990) indicating additionally the classification of the Tihany peridotites (for details, see text). NOFLUID – no fluid inclusions found in the rock, FLUIDPOOR - fluid inclusion present in the rock tough with a small amount, FLUIDRICH - fluid inclusion present in the rock in large amount. Abbreviations: Ol – olivine, Opx – orthopyroxene, Cpx – clinopyroxene, Spl – spinel, Opx/Cpx: orthopyroxene/clinopyroxene molar ratio (note that the average opx/cpx ratio of the subcontinental mantle is ~2; Downes er al., 1992) cg – coarse grained, av – average, T – calculated equilibrium temperature.

5.1.2. Fluid inclusion petrography

Fluid inclusions have been found in orthopyroxenes, whereas inclusions in clinopyroxene are less common and in olivine were not found. No primary or pseudosecondary melt inclusions were identified.

Fluid inclusions are negative crystal shaped with size varying between 3-70 μm (Figure 5a-d). At room temperature these fluid inclusions contain mainly one phase, whereas, if partially decrepitated (Figure 5a-d), they are composed of a liquid and a vapor phase. Using definition of Roedder (1984), this generation can be referred as either primary (single fluid inclusions), or pseudosecondary (appearing along healed fractures without reaching the mineral edges) and secondary (appearing along healed fractures reaching the mineral edges) fluid inclusions. Rarely 4-15 μm sized rhombohedral shaped crystals also occur in the fluid inclusions in maximum 10 vol.% (Figure 5d).

Among the Tihany peridotite series there is a group of xenoliths which contains no fluid inclusions (*Tih 0304, Tih 0305, Tih 0501, Tih 0503;* Table 1). The other, fluid inclusion-bearing, group can be divided into two subgroups: a fluid inclusion-poor and a fluid inclusions-rich one. The fluid inclusions-rich xenoliths (*Tih03-10, Tih 0507, Tih 0509;* Table 1) enclose fluid inclusions with high abundance, whereas the fluid inclusion-poor ones host only some fluid inclusions (*Tih 0504, Tih 0506;* Table 1). Considering the absence/presence of the fluid inclusions, the studied peridotite xenoliths are divided into (1) fluid inclusion-absent, referred as NOFLUID, xenoliths, (2) fluid inclusion-poor, referred as FLUIDPOOR, xenoliths, and (3) fluid inclusion-rich, referred as FLUIDRICH, xenoliths in the following (Table 1).

As observed in many other mantle peridotites worldwide (de Vivo *et al.,* 1988; Szabó and Bodnar, 1996; Frezzotti and Peccerillo, 2007), small (up to 15 μm), rounded or worm-like, at room temperature vapor and/or liquid-rich fluid inclusions occur along intergranular microfractures. On the basis of their petrographic features, these highly likely late-stage inclusions represent different environment and/or time of formation compared to the entrapment of fluid inclusions studied here and are not considered in this study.

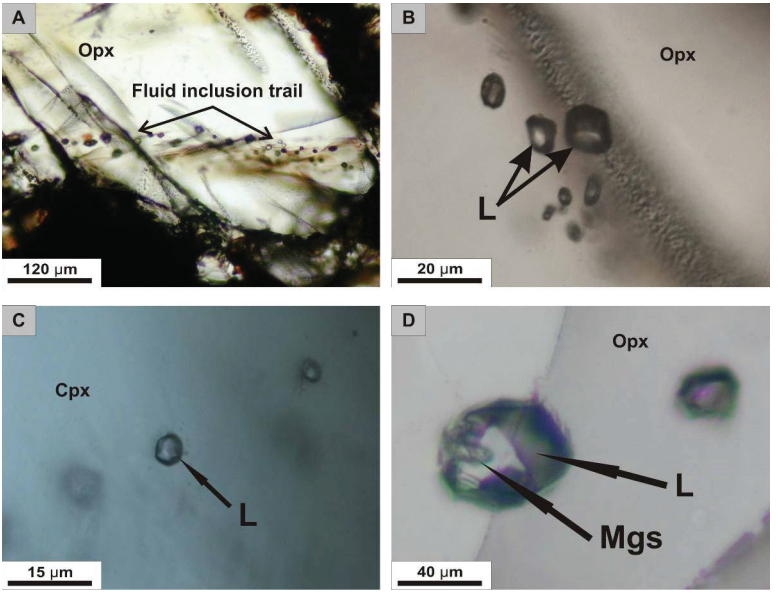

Figure 5 Photomicrographs showing the fluid inclusion petrographic characteristics of the Tihany peridotite series. A) orthopyroxene-hosted, negative crystal shaped fluid inclusion trail Sample: Tih 0509. B) partially decrepitated, negative crystal shaped at room temperature mainly one phase (liquid – confirmed by microthermometry) fluid inclusions in clusters hosted by orthopyroxene Sample: Tih 0310. C) Clinopyroxene-hosted, negative crystal shaped one phase (liquid – confirmed by microthermometry) fluid incusion hosted in clinopyroxene. Around the fluid inclusion in the middle of the picture, decrepitation halo can be observed. Sample: Tih 0506. D) partially decrepitated negative crystal shaped fluid inclusions in orthopyroxene. Beside the liquid (confirmed by microthermometry), solid phase, namely magnesite (confirmed by Raman microspectroscopy) was found within the fluid inclusion Sample: Tih 0310. Abbreviations: Opx - orthopyroxene, Cpx - clinopyroxene, L – liquid phase, Mgs - magnesite. All the pictures have been taken at room temperature using plane polarized light, 1N.

5.2. Szentbékkálla peridotite

5.2.1. Xenolith petrography

The studied sample is a composite xenolith as the peridotite is crosscut by a clinopyroxenite vein. On the basis of the petrographic observation, the composite xenoliths can be divided into three parts: the clinopyroxenite vein, the interaction zone and the lherzolite wall rock (Figure 6). In the followings the three parts will be separately introduced.

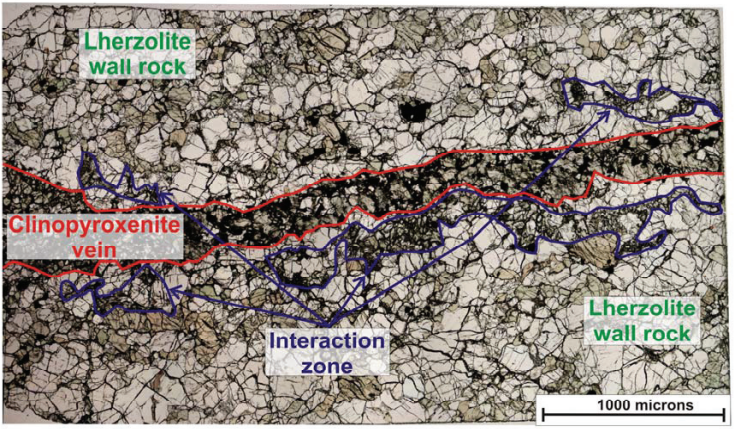

Figure 6 Photomicrograph (transmitted light, 1N) of the whole thin presenting the main textural features of the Szentbékkálla composite xenolith (Szb 0311) indicating the interrelation of the clinopyroxenite vein (red letters), the interaction zone (blue letters) and the lherzolite wall rock (green letters). The latter one hosts the studied fluid inclusions.

Sample	Modal percentages				Opx/ Cpx	Rock type	Texture	Grain size (mm)	T (°C)
	Ol	Opx	Cpx	Spl				average	
Szb0311 wall rock	65.1	27.1	6.9	0.9	3.9	lherzolite	cg-poikilitic	1.6 – 1.7	1120
Szb0311 vein	7.3	-	54.3	38.4	-	clinopyoxenite	magmatic	~ 1.1	-

Table 2. The modal composition, rock type (after Streckeisen, 1976) and texture, equilibrium temperature based on two-pyroxene thermometer (Brey and Köhler, 1990) of the Szentbékkálla composite peridotites (for details, see text). Abbreviations: Ol – olivine, Opx – orthopyroxene, Cpx – clinopyroxene, Spl – spinel, Opx/Cpx: orthopyroxene/clinopyroxene molar ratio (note that the average opx/cpx ratio of the subcontinental mantle is ~2, (Downes et al., 1992) cg – coarse grained, av – average, T - temperature.

5.2.1.1 The clinopyroxenite vein

The vein is composed mainly of coarse-grained clinopyroxene (500 μm – 2 millimeters) and spinel (400-700 μm) (Figure 7a). The latter one occurs either as interstitial phase or as crystal inclusion. The clinopyroxenes are bright brown and dominantly euhedral or subhedral in shape. These clinopyroxenes have spongy rim. In addition, they are abundant in different inclusions: 1/ multiphase (glass + solids + bubble) *silicate melt inclusions* with a size varying between 5-40 μm having spherical shape. Using the definition of Roedder (1984) and Kerkhof and Hein (2001), this generation can be referred as either primary (single fluid inclusions), or pseudosecondary (appearing along healed fractures without reaching the mineral edges), 2/ secondary *fluid inclusions* appearing along intergranular healed fractions. They have rounded and elongated shape and contain mostly one (liquid) or two (liquid and vapor) visible phases at room temperature, their size ranges between 3-20 μm; 3/ primary sulfide melt inclusions (Figure 7b and c). Sulfide melt inclusions occur in all parts of the rocks, however, the vast majority of these inclusions can be found in the vein, therefore, will be discussed here. They have a rounded or irregular shape with a size between 10-100 μm. The glass-hosted sulfide melt inclusions (Figure 7b and c)

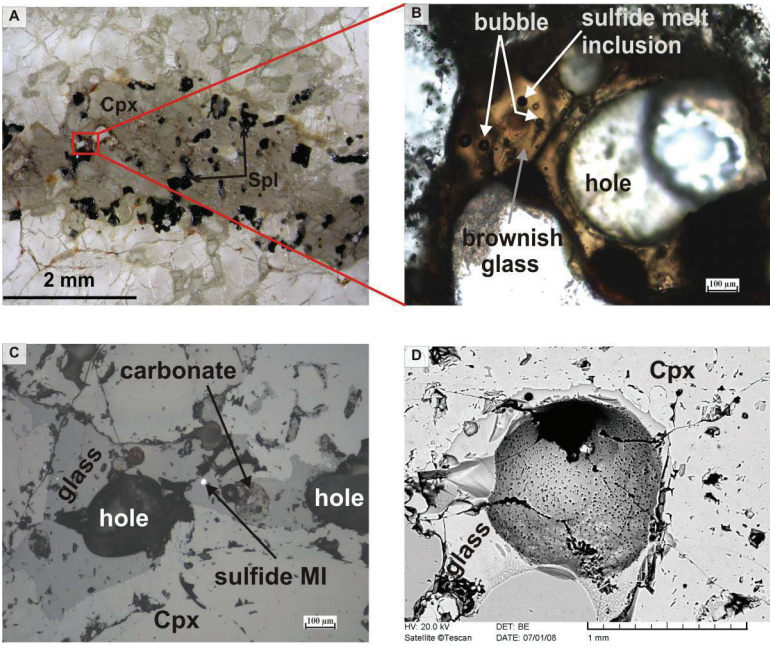

Figure 7. Photomicrographs on the characteristics of the clinopyroxenite vein (Szb0311). A - stereomicroscopic view of the pyroxenite-forming clinopyroxene (Cpx) and spinel (Spl), B – enlarged part of the pyroxenite vein (picture A) representing the interstitial brown glass which contains spherical bubbles and sulfide melt inclusions (picture taken using transmitted light, 1N). C – reflected light image shows the textural relation of clinopyroxene (Cpx), brown glass, sulfide melt inclusions (MI) and carbonate globules. D – backscattered electron image that demonstrates the glass have many spherical shaped vesicles on its surface

are monophase, whereas in some cases the vein clinopyroxene-hosted ones are poliphase inclusions. Interstitially, brownish glass is found predominantly in the vein. At the interface between the glass and the clinopyroxene and spinel the traces of the dissolution and re-precipitation can be clearly seen. Several phases have been identified in the brown glass, as follows: 1/ skeleton (unidentified whether silicate or oxide) crystal, having size between several to 300 microns and tabular shape are mainly found in clusters or at the glass/spinel boundary layer, 2/ sulfide melt inclusions (discussed later), 3/ rounded-shaped carbonates, which is commonly defined in the literature as "carbonate globules". These highly likely carbonate microcrystals occurs in roundish-shaped volume enclosed in the glass (Figure 7c). Besides, similar rounded „holes" can also be found in the glasses, which have pitted surface (Figure 7d), 4/ spherical-shaped bubbles sizes 5-60 μm (Figure 7b). Optically it is no possible to determine their phase(s) if there are any.

5.2.1.2. The interaction zone

The interaction zone is found in the "vicinity" of the clinopyroxenite vein with a maximum distance from the vein of about 600 μm (Figure 8a) showing non-equilibrium texture. This part of the rock is a transitional zone between the clinopyroxenite vein and the lherzolite wall rock, and mostly composed of clinopyroxene and olivine, both of these minerals are subhedral or anhedral. T he average grain size decreased in this part: the olivine and the clinopyroxene has the same size, between 200 and 500 μm (Figure 8b). Similarly to the clinopyroxenes in the vein, the rim of this phase shows a spongy character. Euhedral and subhedral spinel also present, its sizes are up to 50 μm. Similarly to the vein, carbonate globules are common (Figure 8c-f)

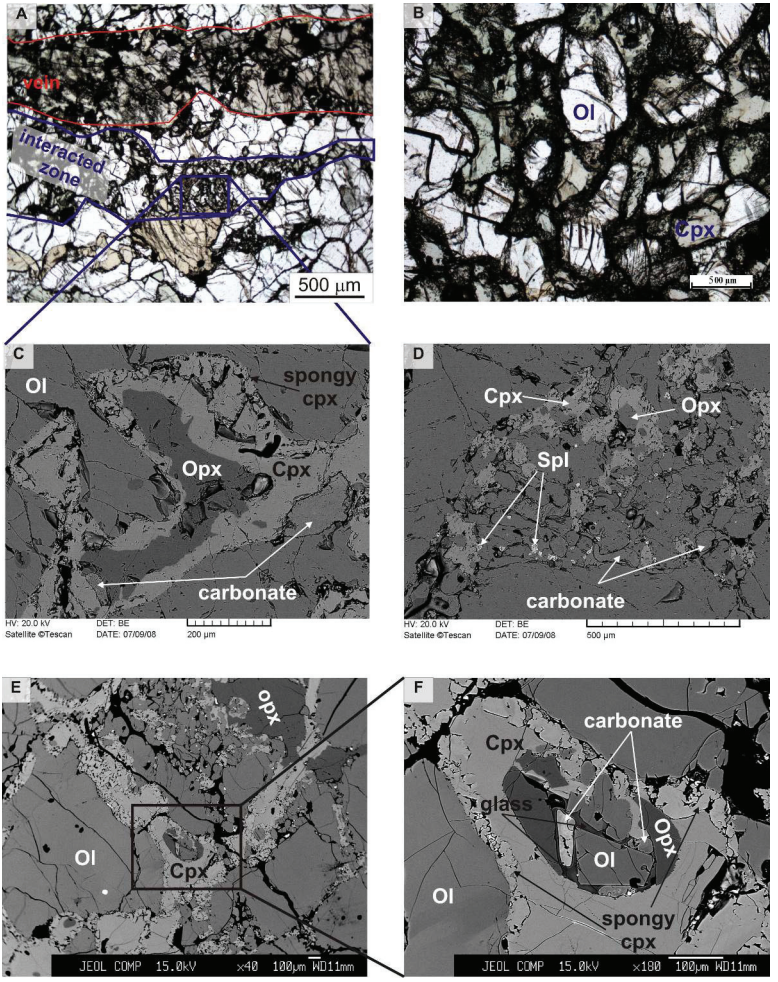

Figure 8. Photomicrographs showing the characteristics of the interaction zone (Szb0311). A and B – transmitted light image (1N) demonstrating the relation of the interaction zone to the clinopyroxenite vein and the texture of the olivines (Ol) together with clinopyroxenes (Cpx), respectively C - F backscattered electron images presenting the orthopyroxene (Opx)-consuming clinopyroxene coronas, carbonate globules, spinels (Spl) and the euhedral olivines (Ol). Position of picture 'C' is marked on the picture 'A'. Picture 'F' shows a part of area 'E' enlarged

Predominantly in that zone (and also in the lherzolite part but more subsequently) the clinopyroxene consumes the orthopyroxene. However, as this reaction is not completed, remaining anhedral orthopyroxenes, enclosed by clinopyroxenes, occurs in the interaction zone. Small amount interstitial brown glass can be found in this part having the same features as the ones in the clinopyroxenite vein. In addition, glass also presents together with the orthopyroxene (Figure 8 e and f). In this case, besides the consuming anhedral orthopyroxene coexists with euhedral olivine coexists (Figure 8e and f).

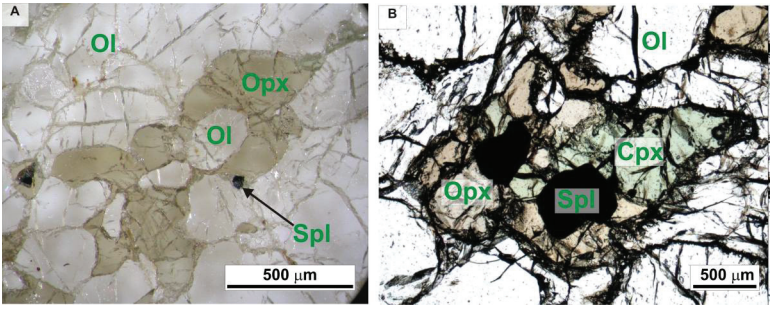

Figure 9. Photomicrographs showing the characteristics of thr lherzolite wall rock of the Szentbékkálla sample (Szb 0311). Orthopyroxene often encloses olivines, as demonstrated on the picture 'A' (stereomicroscopic view), whereas all the rock-forming minerals together can be seen on 'B' (transmitted light, 1N). Abbreviations: Ol - olivine, Opx - orthopyroxene, Cp x-clinopyroxene, Spl - spinel

5.2.1.3. The lherzolite wall rock

The lherzolite wall rock is a coarse-grained spinel peridotite composed of only anhydrous silicates, such as euhedral or subhedral olivine (1-3 mm), subhedral or anhedral orthopyroxene (0.5-4 mm), euhedral or subhedral clinopyroxene (0.3-1 mm) and euhedral or subhedral spinel (0.3-1.2 mm) (Figure 9b). Furthermore, spinel can be present either as anhedral/subhedral crystal inclusion enclosed in the silicates or as an interstitial phase. Therefore, the texture of this part is addressed as coarse-grained poikilitic, where spinel and silicate phases, mostly olivine are enclosed in orthopyroxene (Figure 9a). The crystal inclusions, both the spinel and the olivines, are euhedral or

subhedral having a size up to 500 μm. The lherzolite part is an orthopyroxene-rich lherzolite rock (Table 2).

Similarly to the feature observed in the interaction zone, clinopyroxene coronas around the orthopyroxene can be seen, however, with a lesser extent. Textural equilibrium feature, such as triple junctions at the grain boundaries of olivines, could also be seen. Interstitial glass at grain boundaries is rarely found, and sometimes clinopyroxene hosts sulfide inclusions.

5.2.2. Fluid inclusion petrography

In this subchapter only selected fluid inclusions, found solely in the lherzolite wall rock, will be described. These fluid inclusions are pseudosecondary (appearing along healed fractures without reaching the mineral edges) or secondary (appearing along healed fractures reaching the mineral edges) in orthopyroxene, however, pseudosecondary or primary (appearing along growth zone) (Figure 10a) in clinopyroxene. Rarely, olivine also hosts secondary fluid inclusions, however no primary or pseudosecondary melt inclusions were identified.

The fluid inclusions are negative crystal shaped, enclosing mainly one visible phase (liquid), rarely two (liquid + vapor) visible phases at room temperature (Figure 10b-d). In contrast to the fluid inclusions in the Tihany peridotites (Figure 5d), these inclusions have no visible solid phases. Their sizes are varying between 3-45 μm.

As observed in many other mantle peridotites worldwide (de Vivo *et al.,* 1988; Szabó and Bodnar, 1996; Frezzotti and Peccerillo, 2007), in the studied xenoliths small (up to 15 μm), rounded or worm-like, at room temperature vapor and/or liquid-rich fluid inclusions also occur along intergranular microfractures. According to their petrographic features, these inclusions highly likely late-stage inclusions, which represent different environment and/or time of formation compared to the entrapment of fluid inclusions studied in details here and are not considered in this thesis.

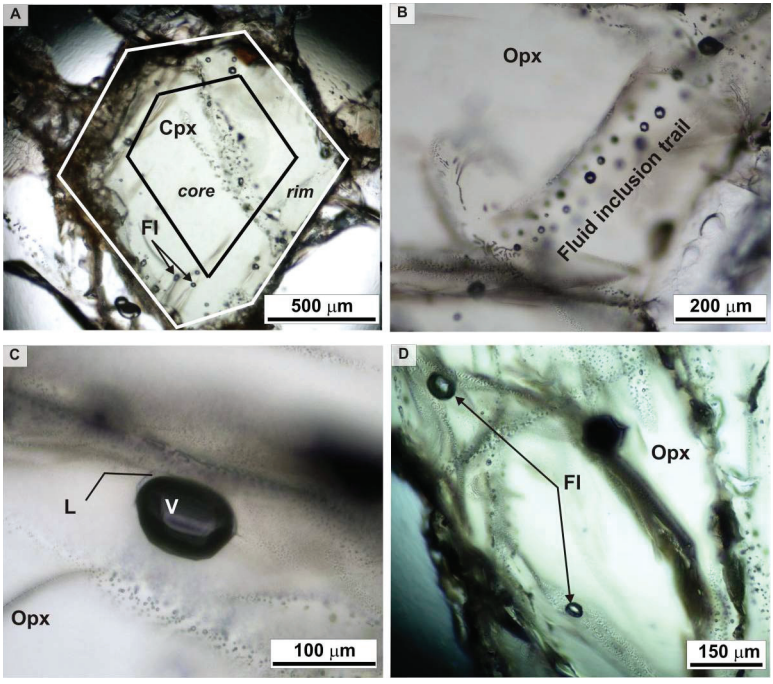

Figure 10. Photomicrographs showing the fluid inclusion petrographic characteristics of the Szentbékkálla peridotite. A - negative crystal shaped, high dense fluid inclusions at the rim, and trail of secondary, strongly decrepitated fluid inclusion in the core of clinopyroxene. B - partially decrepitated, pseudosecondary fluid inclusions in orthopyroxene. C - orthopyroxene-hosted fluid inclusion at room temperature with two visible immiscible fluid phases. D – orthopyroxene-hosted negative crystal shaped fluid inclusions containing one visible fluid phase at room temperature. All the pictures have been taken under transmitted light, 1N. Abbreviations: Cpx - clinopyroxene, Opx - orthopyroxene, L - liquid phase, V - vapor phase, FI - fluid inclusion

6. MAJOR ELEMENT MINERAL CHEMISTRY

6.1. Tihany peridotites

In the rock-forming minerals of the Tihany peridotites no significant major element zonation was observed (Appendix 1). Olivines, either as interstitial or as enclosed mineral inclusions show mg# [$100\times Mg/(Mg+Fe^{2+})$] of 0.90-0.91 and possess high NiO (0.30-0.43 wt.%) content (Appendix 1).

Similarly to the olivines, the mg# of orthopyroxenes is consequently high (0.91-0.92) regardless to the absence or presence of fluid inclusions in the xenolith. However, the major element content of orthopyroxenes in the NOFLUID and FLUIDPOOR xenoliths shows consistently low Al_2O_3 (2.66–3.05 wt %), Na_2O (0.01-0.08 wt %), and elevated Cr_2O_3 (0.55–0.59 wt %) contents in contrast to the FLUIDRICH xenoliths, where higher Al_2O_3 (up to 6.86 wt.%), (Figure 11a, Appendix 1) and Na_2O (up to 1.16 wt.%) (Figure 11b, Appendix 1) contents were observed. The composition of NOFLUID and FLUIDPOOR orthopyroxenes falls close to the compositional range of orthopyroxenes found in orthopyroxene-rich olivine websterite veins and harzburgite wall rock published from Szentbékkálla (Bali *et al.,* 2007) (Figure 11a and b).

Clinopyroxenes have also high mg# ranging between 0.90 and 0.93. In the NOFLUID xenoliths clinopyroxenes are homogeneous and show low Al_2O_3 (2.66–3.27 wt.%), TiO_2 (0.03-0.11 wt.%) and Na_2O (0.39-0.74 wt.%), high Cr_2O_3 (0.73–0.90 wt.%). Nevertheless, there are continuous elevation in concentration of Al_2O_3 (3.25–6.86 wt.%), TiO_2 (0.07-0.31 wt.%), Na_2O (0.16-1.15 wt.%) in clinopyroxenes from FLUIDPOOR to FLUIDRICH xenoliths relative to the NOFLUID xenoliths (Figure 11c and d; Appendix 1). However, compositional difference can be observed between the NOFLUID and FLUIDRICH clinopyroxenes (Figure 11c and d; Appendix 1). The NOFLUID clinopyroxenes show compositional range (Figure 11c and d; Appendix 1) close to those clinopyroxenes found in orthopyroxene-rich olivine websterite veins and harzburgite wall rock from Szentbékkálla (Bali *et al.,* 2007).

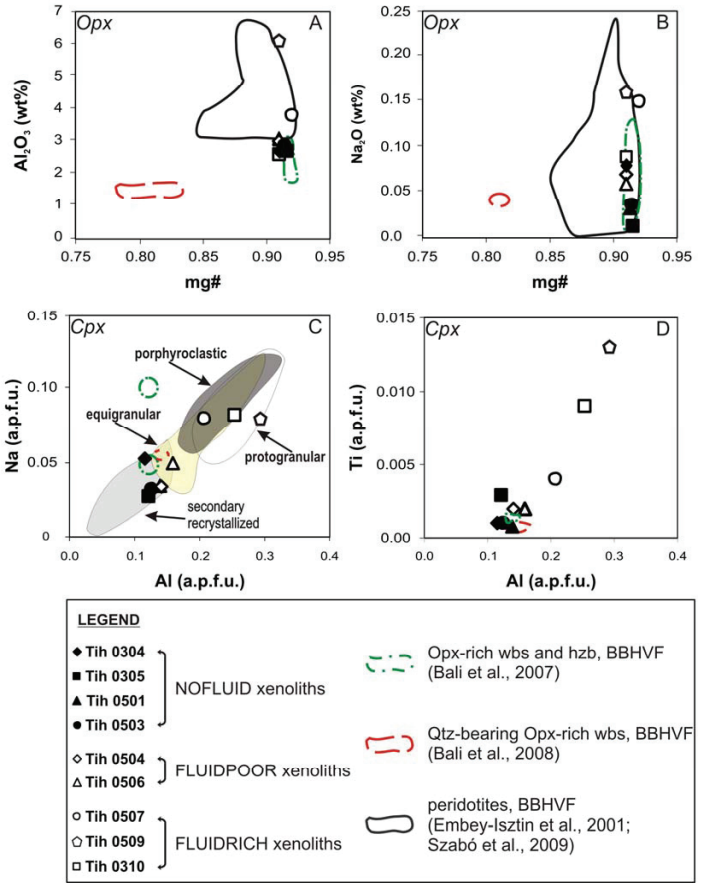

Figure 11. Composition of orthopyroxene (A and B) and clinopyroxene (C and D) of the studied Tihany peridotites (Bakony-Bakony Highland Volcanic Field, Central Pannonian Basin, Hungary). For comparison, orthopyroxene-rich xenoliths from the same volcanic field after Bali *et al.,* (2007, 2008) and compositional fields of clino- and orthopyroxenes from BBHVF peridotites (Embey-Isztin *et al.,* 2001 and Szabó *et al.,* 2009) are denoted. On the diagram C) xenolith data from BBHVF is indicated with respect of their texture (after Downes *et al.,* 1992; Embey-Isztin *et al.,* 2003; Falus, 2004). On the figures ortho- and clinopyroxene compositions from NOFLUID, FLUIDPOOR, FLUIDRICH xenoliths are separately shown. Abbreviations: BBHVF – Bakony-Balaton Highland Volcanic Field, Opx - orthopyroxene, Cpx - clinopyroxene, wbs - websterite, hzb - harzburgite, Qtz-quartz, a.p.f.u. – atoms per formula unit.

Spinels have a wide compositional range (Figure 12; Appendix 1). They are characterized by narrow ranges in NOFLUID xenoliths, whereas spinels in FLUIDPOOR and FLUIDRICH xenoliths have wider compositional range (Appendix 1). The cr-number [Cr/ (Cr+Al)] of the spinel is between 0.39 and 0.49 with one exception: 0.14 in sample Tih 0509 (Appendix 1; Figure 12.).

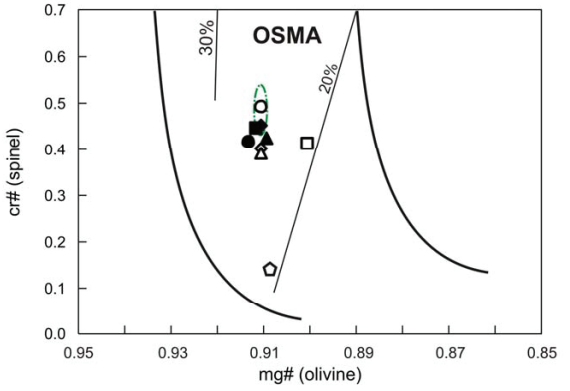

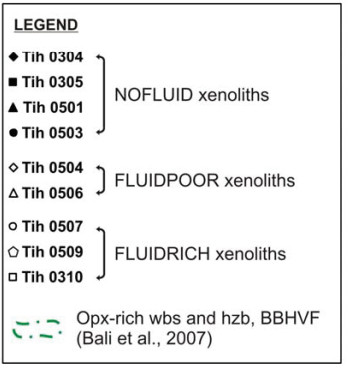

Figure 12. Relationship between Cr/(Cr + Al) ratio (cr#) of spinel and Mg/(Mg+Fe^{2+}) ratio (mg#) of coexisting olivine in fluid absent and fluid hosted mantle xenoliths from Tihany. The region labeled by olivine-spinel mantle array (OSMA) (indicating by the black curves) after Arai (1994). Compositional fields for spinel peridotites from Bakony-Balaton Highland Volcanic Field (Downes et al, 1992; Embey-Isztin *et al.,* 2003; Falus, 2004) showing the textural differences. The fine lines separate the possible compositional fields of the different percent of partial melting (corresponding grade is indicated on the left-bottom side of the line)

6.2. Szentbékkálla peridotite

Olivines have lower mg# than those of Tihany peridotites as the number varies between 0.85 and 0.86 (Appendix 2). The NiO content shows wide range (0.11-0.34 wt.%), nevertheless, the most of the olivines possess rather low NiO content (0.21 wt.% in average). The rock-forming olivines have lower, whereas the olivine inclusions have higher NiO content.

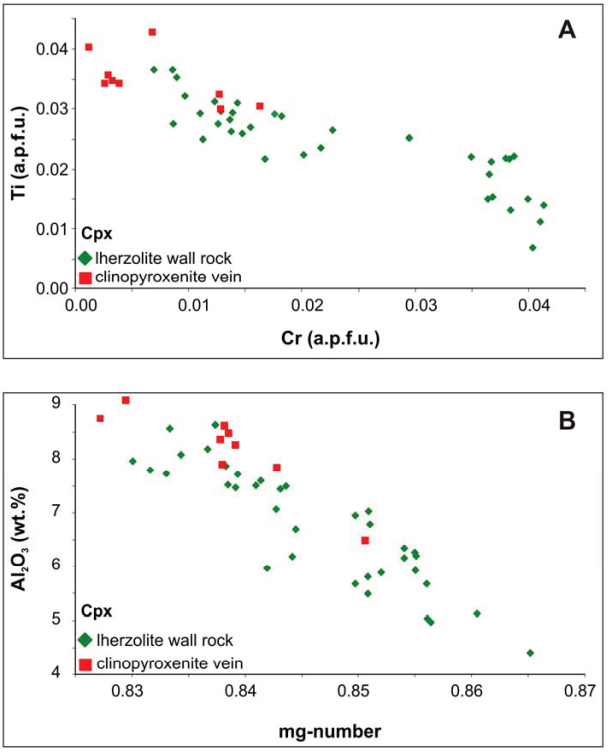

Figure 13. Major element variations of clinopyroxenes (Cpx) in the Szentbékkálla peridotite (Szb 0311). A) shows Cr-Ti correlation, whereas B) shows correlation of mg-number with the Al_2O_3 content. Red square indicates data collected from the clinopyroxenite vein, the green diamonds indicate data from the lherzolite wall rock. Abbreviation: a.p.f.u. – atomic per formula unit

Orthopyroxenes have similar mg# (0.86-0.87) to olivines, Al_2O_3 content varies between 3.97 and 5.69 wt.% (Appendix 2). Moreover, the orthopyroxenes are characterized by low Cr_2O_3 (0.26-0.74 wt.%) (Appendix 2), whereas elevated Na_2O content (0.11-0.46 wt.%) (Appendix 2).

Clinopyroxenes have mg# (0.83-0.86) which is slightly lower than that of orthopyroxene and olivine (Appendix 2). However, there are two geochemically different clinopyroxene groups being in a good agreement with the petrographic observation: the vein clinopyroxenes are different in major element composition compared to the ones in the lherzolite. The vein clinopyroxenes possess elevated concentration in basaltic major element components, such as in Al_2O_3 (6.49-9.09 wt.%, average: 8.21 wt.%) (Figure 13), TiO_2 (1.09-1.54, average: 1.27 wt.%) (Figure 13) and CaO (18.54-21.51, average: 19.46 wt.%) (Appendix 2). The major element compositions of the clinopyroxenes in the lherzolite wall rock are dependent on the distance from the clinopyroxenite vein: diverging from the vein towards the vein there is a continuous increase in Cr_2O_3 (from 0.24 to 1.44 wt.%), whereas decrease in TiO_2 (from 1.34 to 0.25wt.%) and in Al_2O_3 (from 8.64-4.40 wt.%) (Appendix 2).

Strong negative correlation is shown between the cr-number and the mg-number in spinels (Figure 14): the mg-number varies between 0.537-0.702 (from the lherzolite wall rock to the clinopyroxenite vein), whereas the cr-number ranges between 0.005-0.378 (from the clinopyroxenite vein to the lherzolite wall rock).

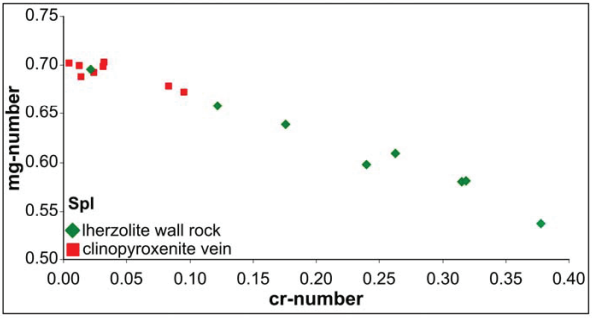

Figure 14. Cr-number vs. mg-number of spinels (Spl) of the Szb 0311 composite xenolith. Red square indicates data collected from the clinopyroxenite vein, whereas green diamonds show data from the lherzolite wall rock.

6.3. Equilibrium temperature

Equilibrium temperature was calculated based on the major element compositions of the constituent minerals. For equilibrium temperature two pyroxene thermometer was used suggested by Brey and Köhler (1990) at a pressure of 1.5 GPa. The Tihany peridotites show a wide range of equilibrium temperature between 925-1165 °C (±16 ºC) which is more extended than that of peridotites collected from other localities in BBHVF (Embey Isztin *et al.,* 2001). For the Szb0311 xenolith, only the core compositions of orthopyroxene-clinopyroxene pairs in the lherzolite part were used for the calculation, which provides an equilibrium temperature of 1100 ºC (±16 ºC).

7. TRACE ELEMENTS

7. 1. Trace element composition of clinopyroxenes and orthopyroxenes

7. 1. 1. Tihany peridotites

In terms of trace elements no zonations were observed from core to rim in pyroxenes. The clinopyroxenes show narrow composition in the same rock sample, except for highly incompatible trace elements, but varies in different xenoliths (Appendix 4; Figure 15). In trace element compositional point of view, the Tihany peridotite xenoliths can be distinguished in two parts.

For clinopyroxenes in the NOFLUID xenoliths the most unambiguous feature is the so-called 'U-shaped' REE (rare earth elements + Y) C1 chondrite-normalized pattern (Figure 16a), which means depletion in MREE compared to LREE and HREE (Appendix 4; Figure 16a). The La_N/Lu_N ratios are between 0.82 and 2.21 (1.46 in average), the La_N/Sm_N ratios are between 2.48 and 9.49 (5.21 in average). Regarding the normalized REE pattern of clinopyroxenes in Tih 0305 and Tih 0503 NOFLUID xenoliths, their clinopyroxenes have slight elevation in Ce, Nd and Sm compared to those of the other NOFLUID xenoliths (Figure 16a). The NOFLUID clinopyroxenes display REE pattern similar to those of clinopyroxenes described in orthopyroxene-rich olivine websterite veins and harzburgite wall rock from Szentbékkálla by Bali *et al.* (2007) (Figure 16a). From the most MREE-depleted clinopyroxenes in Tih 0304 xenolith, a continuous increase in HFSE (Zr, Hf, Ti) can be observed from Tih 0501 through Tih 0305 to Tih 0503 (Figure 15). The latter two xenoliths have concentration of Zr, Hf, Ti similar to that of FLUIDPOOR ones. However, Ti shows negative anomalies in NOFLUID samples, except for the Tih 0305 xenolith, and slight enrichment in Sr and Pb on the primitive mantle-normalized multielement patterns (Figure 15). Not only the REE, but the HFS elements also show similarities to orthopyroxene-rich olivine websterite veins and harzburgite wall rock from Szentbékkálla (Bali *et al.,* 2007) as demonstrated in Figure 15. Orthopyroxenes in the NOFLUID xenoliths are extremely depleted in LREE and MREE, the La_N/Sm_N are between 0.011 and 0.115, with an average of 0.038.

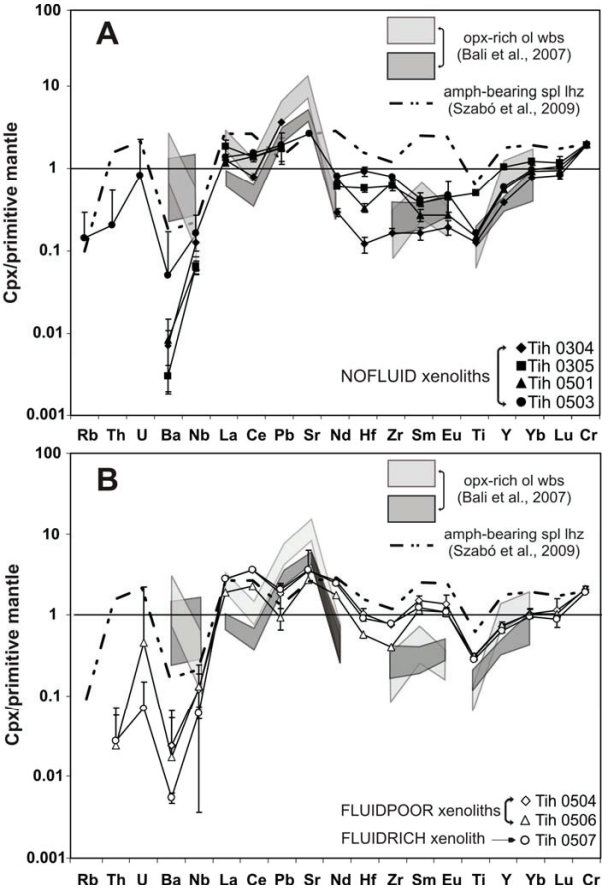

Figure 15. Primitive mantle normalized trace element pattern of clinopyroxenes of the Tihany peridotites. Lines indicate the average trace element values of clinopyroxenes of the studied xenoliths, the error bars indicate the standard deviation. A: for NOFLUID xenoliths, B: for FLUIDPOOR and FLUIDRICH xenoliths. For comparison, trace element patterns for orthopyroxene-rich xenoliths from Szentbékkálla (Bali *et al.,* 2007 and amphibole-bearing spinel lherzolites (Szabó *et al.,* 2009) from the same volcanic field are also shown by shaded and areas and dashed-dotted curves, respectively. Note that clinopyroxenes published by Szabó *et al.,* (2009) have wider compositional ranges, here the one with the lowest normalized values (sample name Szg07 xenolith) is shown. Primitive mantle composition is after McDonough and Sun, 1995). Cpx - clinopyroxene, opx-rich ol wbs - orthopyroxene-rich olivine websterite

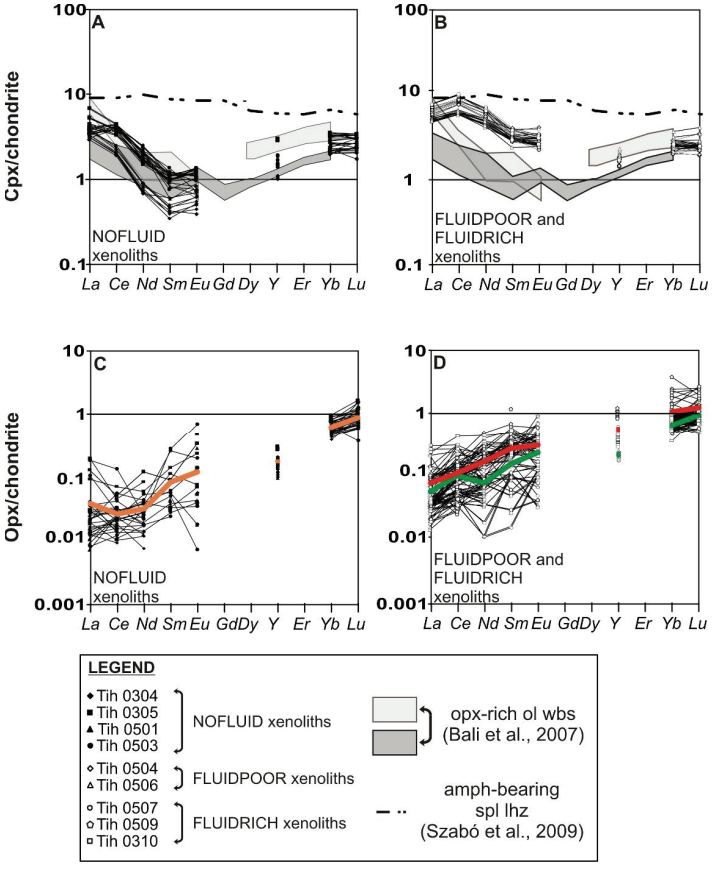

Figure 16. Chondrite normalized rare earth element (REE+Y) pattern for clinopyroxenes (A and B) and orthopyroxenes (C and D) in the Tihany peridotites. Diagrams A and C show pyroxenes patterns in the NOFLUID xenoliths, diagrams B and D display pyroxenes patterns in the FLUIDPOOR and FLUIDRICH xenoliths. For comparison, trace element patterns for orthopyroxene-rich xenoliths from Szentbékkálla (Bali *et al.,* 2007 and amphibole-bearing spinel lherzolites (Szabó *et al.,* 2009) from the same volcanic field are also shown by shaded and areas and dashed-dotted curves, respectively. Orange line indicates the average normalized values of NOFLUID orthopyroxene, green and red lines indicate the average normalized values of FLUIDPOOR and FLUIDRICH xenoliths, respectively. Chondrite composition is after Anders and Grevesse, 1989). Abbreviations: Opx - orthopyroxene, Cpx - clinopyroxene, amph-bearing spl lhz – amphibole-bearing spinel lherzolite, hzb - harzburgite, opx-rich ol wbs - orthopyroxene-rich olivine websterite.

In comparison the REE distribution in clinopyroxenes of the FLUIDPOOR and FLUIDRICH xenoliths have an "n-shaped" pattern with no depletion in MREE relative to the U-shaped ones, but slight enrichment can be observed in LREE (Figure 16b). This is proved by the normalized ratios of the La_N/Sm_N ratios which are between 1.38 and 2.18. Clinopyroxenes in the FLUIDPOOR xenoliths have enrichment in Ce, Nd, Sm, Eu, Zr and Hf compared to the NOFLUID xenoliths (Figure 15). In La and HREE no compositional difference was observed. The primitive mantle-normalized trace element patterns of clinopyroxenes in the FLUIDPOOR and FLUIDRICH xenoliths are similar to that an amphibole spinel lherzolites, found in the same volcanic field, in which coexisting silicate melt and fluid inclusions are present (Szabó *et al.,* 2009; Hidas *et al.,* 2010).

The orthopyroxenes of the FLUIDPOOR and FLUIDRICH xenoliths have also depletion in LREE and MREE, and also have higher concentration in Ce, Nd, Sm and Eu than the NOFLUID ones (Figure 15c and d; Appendix 3), similarly to the clinopyroxenes.

7.1.2. Szentbékkálla peridotite

The trace elements patterns of clinopyroxenes have similar distribution both for the clinopyroxenite vein and for the lherzolite wall rock (Figure 17). However, the trace elements in the vein clinopyroxenes have elevated concentration relative to those in the lherzolite wall rock (Figure 17; Appendix 5). Similarly to the FLUIDPOOR and FLUIDRICH clinopyroxenes in the Tihany peridotite series, the REE pattern of the Szentbékkálla clinopyroxenes show an n-shaped pattern. On the C1 chondrite-normalized REE diagram (Figure 18) it can be seen that there is enrichment in LREEs and MREEs compared to the HREEs.

To summarize, no unequivocal differences are observed in the trace element compositions between the different vein and wall rock clinopyroxene (Appendix 5).

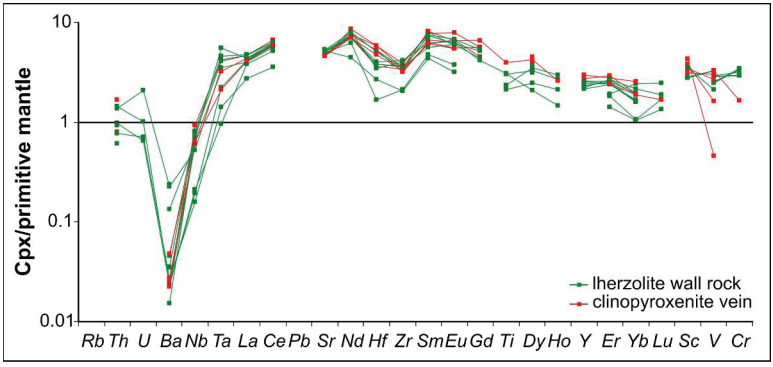

Figure 17. Primitive mantle normalized trace element pattern of clinopyroxenes in the Szentbékkálla Szb0311 xenolith. Green lines indicate normalized values of clinopyroxenes in the lherzolite wall rock, red lines indicate normalized values of clinopyroxenes in the clinopyroxenite vein. Primitive mantle composition is after McDonough and Sun, 1995.

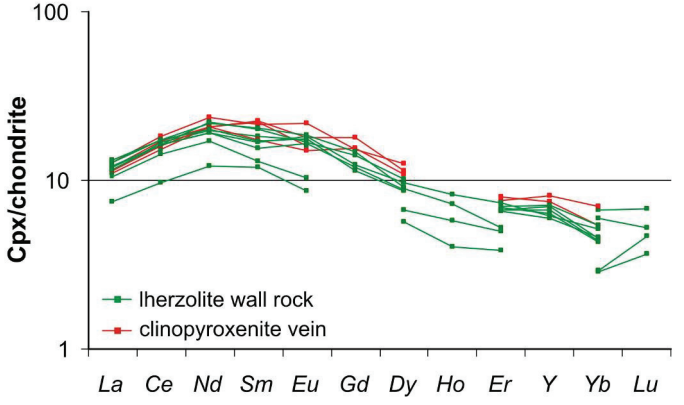

Figure 18. C1 chondrite normalized rare earth element (REE+Y) pattern for clinopyroxenes in the Szentbékkálla Szb0311 xenolith. Green lines indicate normalized values of clinopyroxenes in the lherzolite wall rock, red lines indicate normalized values of clinopyroxenes in the clinopyroxenite vein. C1 Chondrite composition is after Anders and Grevesse, 1989.

7.2. Estimation of trace element ratios linked to fluid inclusions

Trace elements associated to high density fluid inclusions were detected by *in situ* laser ablation ICP-MS analysis in samples Tih 0310, Tih 0509, belonging to the FLUIDRICH xenolith group, and in Szb 0311 in only orthopyroxene-hosted fluid inclusions. Considerable increase of intensities was observed at some trace elements compared to those of host orthopyroxenes during laser ablation ICP-MS analysis of inclusion. The intensity increase must be associated with chemical features of fluid inclusion and inclusion walls in the host orthopyroxenes. By analyzing the CO_2-fluid inclusions *in situ* from the Tihany peridotite xenoliths, predominantly LIL (Large Ion Lithophile) elements such as K, Rb, Ba, moreover Sr, Ti, Nb, Ca, Al intensity increased when fluid inclusions were being ablated. In contrast, the signal of the fluid inclusions from Szentbékkálla was weak, only a slight increase of the Ba, Rb and Nb was seen. Note that the duration of the host-mix transient signals was 15-25 seconds that is somewhat longer time expected from fluid-rich material (Allan *et al.,* 2005, Bertelli *et al.,* 2009).

It is obvious that the absolute element concentration of the ablated CO_2-rich fluid inclusions cannot be determined considering the lack of any internal standards for fluid inclusions. However, trace element ratios in CO_2-rich, COHS fluid inclusions can be estimated as already pointed out by Hidas *et al.* (2010) from fluid inclusions that coexist with silicate melt inclusions in mantle xenoliths from the same volcanic field. To be able to make a considerable comparison with results of Hidas et al. (2010), the same method was applied. For internal standard, Ba was nominated and its hypothetical concentration was set to 100 ppm (Table 3; Figure 19). Furthermore, Cr as a *matrix-only tracer* has been applied to remove the contribution of the host orthopyroxenes from the mixed fluid–host signal. In the "residual signal" the element ratios have been taken account in, which can be considered as semi-quantitative trace element compositions (after Hidas *et al.,* 2010) characteristic for the fluid inclusion (Table 3).

Applying this calculation method, besides the trace elements that are linked to the fluid inclusions and their adjacent host orthopyroxene by regarding only the intensity

versus time transient signal, Pb and Zr have also been identified being associated to the fluid inclusions (Table 3).

The primitive mantle-normalized pattern of the semi-quantified trace elements show similar pattern for the fluid inclusions from the Tihany xenoliths to those published by Hidas *et al.* (2010) (Figure 19), with respect to Nb, K, Pb, Sr and Zr (Figure 19). Additionally, for Na lower concentration was estimated (Figure 19), and for Rb, U, Th, La, Ce, Nd and Hf the concentration was not high enough for calculation. Due to the weak signal for fluids in the Szentbékkálla xenolith, no element ratios were calculated.

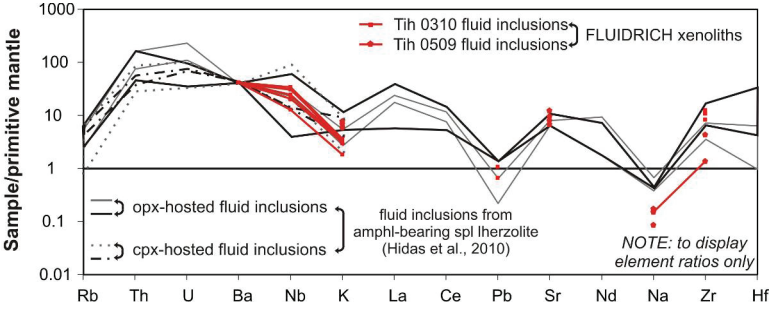

Figure 19. Primitive mantle normalized trace element distribution of fluid inclusions from xenoliths Tih 0310 and 0509 (both belonging to the FLUIDRICH group). Applying the calculation method of Hidas *et al.* (2010) it should be noted that the figure is to display only element ratios. For comparison, the element ratios of Hidas *et al.* (2010) are also indicated. Primitive mantle composition is after McDonough and Sun, 1995.

Xenolith	Tih0310					Tih0509			
Ba	*100*	*100*	*100*	*100*	*100*	*100*	*100*	*100*	*100*
Nb	8.12	8.14	5.90	3.04	7.37	n.d.	n.d.	4.97	n.d.
K	1993	1623	1764	995.7	1885	3768	3255	1705	4223
Pb	1.63	2.64	n.d.	n.d.	n.d.	n.d.	n.d.	n.d.	n.d.
Sr	n.a.	n.a.	n.a.	n.a.	n.a.	57.8	89.1	48.7	68.4
Nd	n.d.	n.d.	n.d.	n.d.	n.d.	n.d.	n.d.	n.d.	n.d.
Na	n.d.	n.d.	82.9	445.3	n.d.	775.9	884.5	440.3	n.d.
Zr	47.5	41.2	31.7	n.d.	41.0	5.23	n.d.	16.4	n.d.
Hf	n.d.	n.d.	n.d.	n.d.	n.d.	n.d.	n.d.	n.d.	n.d.

Table 3. Trace element composition of orthopyroxene-hosted fluid inclusions. Note that, in the lack of internal standard, quantification of fluid inclusions was achieved by method described by Hidas *et al.* (2010) inferring 100 ppm Ba each fluid inclusion. Thus, the numbers must only be considered as element ratios. n.a - not analyzed; n.d - not detected.

8. MICROTHERMOMETRY

8.1. General consideration

The microthermometry of the fluid inclusions provides such information as composition and density on the basis of the phase transitions at different temperatures with assumption that the fluid inclusions keep a constant volume followed by the entrapment (Roedder, 1984).

As a consideration microthermometric analysis was performed on olivine- and pyroxenes-hosted fluid inclusions amongst the natural samples. Contrarily, as a reason of the poor visibility, the microthermometry of the bubbles in the brown glass, no phase transitions were possible to observe. Moreover, if it had been ever possible, it would not have provided information on the density of the fluid in the bubbles because the volume cannot be considered to be constant after trapping like it can for fluid inclusions trapped in minerals.

The microthermometry describes the phase transitions observed under optical microscopic scale. In the followings, optically visible phase transitions will be demonstrated, which are not necessarily all the phase transitions that happen within the fluid inclusions during cooling/heating. On the studied individual fluid inclusions the characteristic phase transitions during cooling and heating were nearly the same no matter which location they derive from. Hence, the microthermometry of the individual fluid inclusions from different localities (Tihany and Szentbékkálla) will be collectively described. However, the poor visibility of the olivine-hosted fluid inclusions does not allow the microthermometric observation of the phases within these fluid inclusions.

8.2. Natural fluid inclusions

The fluid inclusion microthermometry started with very fast cooling down to below -100 ºC so that the fluids, liquid ± vapor at ambient temperature according to the bulk density of the fluid, can surpass the metastable barrier and nucleate a solid phase in

equilibrium with vapor. The inclusions froze out at -80 -90 ºC. At -100 ºC a solid and a vapor phase were together present within the fluid inclusions. Upon progressive heating, two types of phase transition can be observed: (1) melting of solid phase resulting in the solid+liquid+vapor phase assemblage and (2) homogenization of the liquid+vapor into liquid phase. Therefore, the corresponding temperature of these two phases transition is termed as (1) melting temperature and (2) homogenization temperature. No other phase transition, neither visible ice nor gas hydrates melting were observed in the studied fluid inclusions.

8.2.1. The melting temperature (T_{melt})

The melting temperatures, in a one-component system it is also referred to as 'triple point temperature' (Appendix 6) is a point on a P (pressure) - T (temperature) surface where three phases, namely one solid, one liquid and one vapor are present at the same time. Regarding the fact that at low temperatures (<-56.6 ºC) the stable phases were one solid and one vapor, the co-existence of three phases is observed by the phase transition: solid + vapor → solid + liquid + vapor. Thus, the melting starts with the condensation of the liquid and ends up with the complete melting of the solid phase in the presence of the vapor. In reality, the process is very abrupt. The melting temperatures of fluid inclusions in the Tihany peridotites varied from -56.4 and -57.2 ±0.2 ºC, whereas the fluid inclusions from Szentbékkálla xenolith ranges between -56.6 and -56.8 ±0.2 ºC. On the basis of the experiments by Span and Wagner (1996), the melting temperature of the pure CO_2 is at 216.592 ±0.003 Kelvin, which corresponds to -56.558 ±0.003 ºC. Therefore, the CO_2-dominance in the fluid phase has been proven. However, the presence of other volatile species is also suggested in fluid inclusions, which show lower melting temperatures than the triple point temperature of pure CO_2.

8.2.2. The homogenization temperature (Th_{car})

When the solid is completely melted, only the liquid and the vapor phase coexist. Upon further heating, the volume of the liquid phase expands with increasing temperature

at the expense of the vapor phase. This process terminates at the temperature when there is no vapor phase in the fluid inclusions. The temperature where the vapor disappears is called as homogenization temperature, from which the density of the bulk fluid can be calculated assuming one-component fluid system. The homogenization temperature is in reverse accordance with the density: the lower the homogenization temperature to the liquid phase, the higher the density.

The homogenization temperatures are in a range between -41 to +28 ºC in Tihany peridotites (n=73, Appendix 6). Fluid inclusions from Szentbékkálla xenolith show homogenization between -47.8 and +26 ºC (n=37, Appendix 6): the orthopyroxene-hosted fluid inclusions ranges between -47.8 and +26 ºC, whereas the clinopyroxene-hosted ones yield a range of T_h between -44.9 +22 ºC. Therefore, the different host minerals do not cause differences in the homogenization temperature. Instead, as a general rule the smaller the fluid inclusion the lower the homogenization temperature (Figure 20), which is consistent with experimental and theoretical studies of the effect of size on fluid inclusion re-equilibration (Roedder, 1984; Bodnar and Bethke, 1984; Bodnar *et al.,* 1989; Sterner and Bodnar, 1989; Vityk and Bodnar, 1995; Vityk *et al.,* 2000; Viti and Frezzotti, 2000; Fall *et al.,* 2009; Hidas *et al.,* 2010).

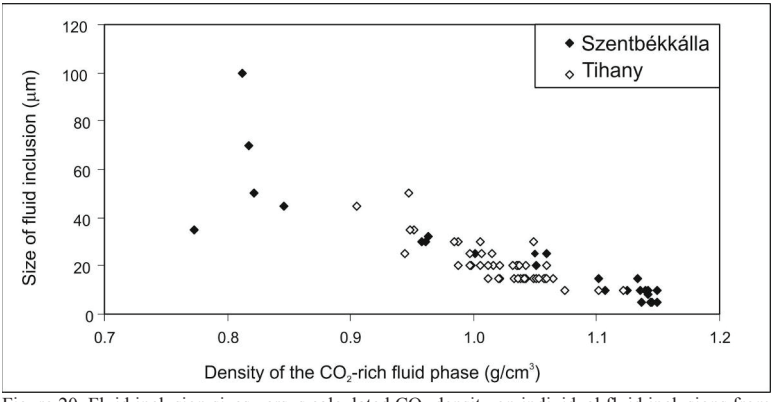

Figure 20. Fluid inclusion sizes versus calculated CO_2 density on individual fluid inclusions from Tihany and Szentbékkálla peridotite xenoliths. Density calculation for the individual fluid inclusions given from homogenization temperature was modeled by pure CO_2 using the equation of state developed by Span and Wagner (1996).

8. 2. 3. Minimum trapping pressure estimation for fluid inclusions

Based on the equation of state by Span and Wagner (1996), the highest calculated densities are between 1.01 and 1.12 g/cm^3, modeling as pure CO_2 (see details in chapter of Discussion) for the xenoliths Tih 0506, Tih 0504, Tih 0507, Tih 0310 and Tih 0509, respectively (Berkesi *et al.,* 2007; Appendix 6). As no process is reasonable that causes increase density in fluid followed by the entrapment, in each sample the highest density fluid inclusions were taken into consideration as the closest to the original trapping density.

As a consequence, minimum trapping pressure condition was also calculated (e.g., Span and Wagner, 1996) to intercept the given isochors, concerning the calculated density, with an independent temperature value (Brey and Köhler, 1990) for the mantle peridotite xenoliths. Minimum trapping pressures for the different xenolith samples are between 0.65 and 1.1 GPa (Appendix 6).

9. RAMAN SPECTROSCOPY

Similarly to this work, Raman spectroscopy has been applied in many fluid inclusion studies for over decades. *"Laser-excited Raman spectroscopy has been successfully applied to the identification and partial analysis of solid, liquid, and gaseous phases in fluid inclusions. The procedure is no panacea for problems of analysis of fluid inclusions, but some unique features make it very useful. In particular, the measurement is performed in situ; it is non-destructive; and it can produce qualitative and quantitative data"* (Rosasco *et al.,* 1975). It can be stated that in the last decades Raman spectroscopy became a fundamental and then routinely used (spectroscopic) techniques of the fluid inclusion studies. Moreover, the coupling of microthermometry and Raman microspectroscopy is still the only viable option to obtain precise composition of the fluid (Dubessy *et al.*, 1982, 1984; Burke 2001; Berkesi *et al.*, 2009; Hidas *et al.*, 2010).

As a consideration, Raman microspectroscopy on the studied individual natural fluid inclusions was carried out at different temperatures, in order to determine the bulk composition of the fluid inclusions. Either the olivine- or the pyroxenes-hosted fluid inclusions have been analyzed in details. Furthermore, the bubbles found in the brown glass were studied by Raman techniques, too. All the Raman peak positions, which will be reported below have been determined by the fitting procedure approximated by Gaussian-Lorentzian function.

9.1. Silicate mineral-hosted fluid inclusions

9.1.1. Raman microspectroscopy at room temperature

9.1.1.2. Fluid phases

The CO_2, being the dominant fluid species within the fluid inclusions has been proven in each fluid inclusions studied (Figure 21c and Figure 22). The identification of the CO_2 was based on its two highest intensity peak, the so-called Fermi diad (Fermi 1931). The Fermi diad bands of CO_2 in fluid inclusions from Tihany and Szentbékkálla xenoliths

varied 1281.18 -1287.49 ±1.6 cm^{-1} and 1384.38-1392.66 ±1.6 cm^{-1}, respectively (e.g. Figure 21c, Figure 22). The peak shift depends on the CO_2-density (pressure), as already proven by Rosso and Bodnar, (1995). The density of CO_2 has been calculated by the CO_2 Fermi diads of the olivine-hosted fluid inclusions in Szentbékkálla composite xenolith, because in these fluid inclusions the poor visibility did not allow to see the homogenization of the CO_2-rich phase. The density of the CO_2 has been calculated by applying the equation of Fall *et al.,* (2011). As a result, the CO_2-density of the olivine-hosted fluid inclusions has a density interval between 0.44 and 1.03 (0.86 in average) g/cm^3 (Table 4). Furthermore, as a general rule, in the highest CO_2-density fluid inclusions, not only the Fermi diads, but also the so-called "hot bands" (peaks at around 1261 cm^{-1} and at around 1408 cm^{-1}, see also Figure 22) appear. Rarely the peak concerning the $^{13}CO_2$ could also be identified (peak appearing ~1371.8 cm^{-1}, Howard-Lock and Stoicheff, 1971; Figure 22).

Sample name	Host	position of CO_2 bands (Fermi diad)		Δ Fermi diad	ρ_{CO2} (g/cm^3)
		upper band (υ^-)	lower band (υ^+)		
Szb0311/ol1/incl1	Ol	1388.12 (±1.8)	1282.89 (±1.8)	105.23	1.03
Szb0311/ol1/incl2		1388.12 (±1.8)	1282.89 (±1.8)	105.23	1.03
Szb0311/ol1/incl3		1386.90 (±1.8)	1282.10 (±1.8)	104.90	0.93
Szb0311/ol2/incl1		1386.60 (±1.8)	1282.89 (±1.8)	103.71	0.44

Table 4. Raman analysis of the CO_2 in olivine-hosted fluid inclusions in Szb 0311 xenolith. Both the position of the upper and the lower band of the Fermi diad are presented. As a result, a calculated density is also shown. Abbreviation: Ol - olivine

H_2S as additional volatile species was also detected with a low-intensity peak at about 2608-2610 cm^{-1} in each fluid inclusion (Figure 21a). In the highest CO_2 density fluid inclusions the peaks of the dissolved H_2O in CO_2 were also detected even at room temperature (Figure 23) in xenoliths Tih 0310 and Szb 0311. Rarely, focusing at the wall of the fluid inclusions, a broad band of liquid H_2O was also found between ~2800 and

~3700cm^{-1} ±1.6 also in xenoliths Tih 0310 and Szb 0311. The peak positions are at 3243 and 3427 cm^{-1} (Figure 23).

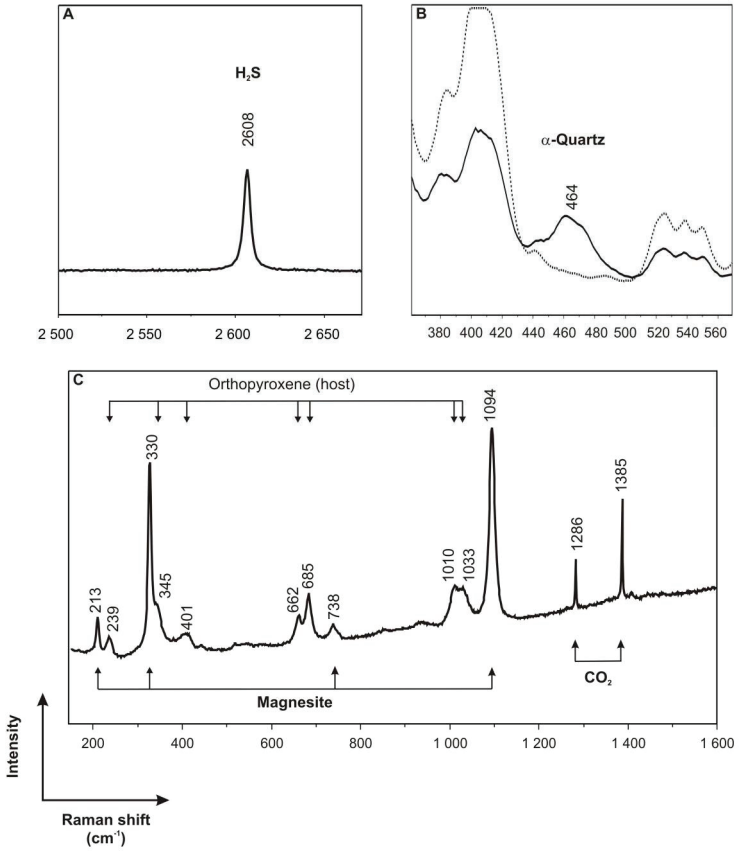

Figure 21. Representative Raman spectra of phases within the studied fluid inclusions. All the spectra were taken at room temperature. Raman spectra between the spectral region of A) 2500-2700 cm^{-1} and B) 360 and 580 cm^{-1} showing peaks at 2608 cm^{-1} (H_2S) and at 464 (α-quartz), respectively. The dashed lines correspond to the spectra taken on the host orthopyroxene close to the fluid inclusions with the same set as done for the fluid inclusions. C) Characteristics of the fluid inclusions within the spectral range of 150-1600 cm^{-1} demonstrating the presence of magnesite and CO_2 in the fluid inclusions. Peak positions (numbers above the peaks) were determined by fitting the peaks with Gaussian-Lorentzian function.

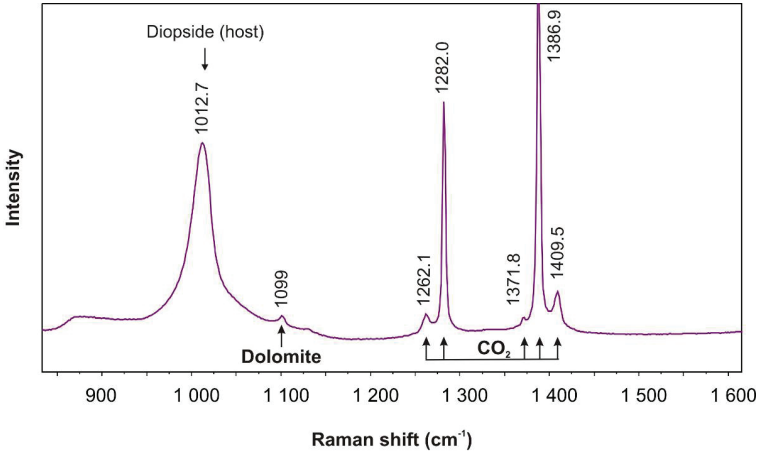

Figure 22. Representative Raman spectra of different solid (daughter) phases in the studied clinopyroxene-hosted fluid inclusions from the Szentbékkálla Szb 0311 xenolith. The spectrum was taken at room temperature. Raman spectrum is shown between the spectral region of 850 and 1650 cm^{-1} demonstrating the presence of dolomite in clinopyroxene (diopside)-hosted fluid inclusions. Peak positions (numbers above the peaks) were determined by fitting the peaks with Gaussian-Lorentzian function. The peak corresponding to the $^{13}CO_2$ is at 1371.8 cm^{-1}.

9.1.1.3 Solid (daughter) phases

The visible solid phase within the orthopyroxene-hosted fluid inclusions (Figure 5d) was identified as magnesite (Figure 21c) from the xenoliths Tih 0310 and Tih 0509 and Szb 0311. Furthermore, majority of those fluid inclusions in which by microscopic observation no solid phases were visible also contain magnesite confirmed based on detected peaks at 1094±1.8, 738±1.8 and 330±1.8 cm^{-1} (Figure 21c) in the xenoliths mentioned above. Additionally, α-quartz always is in coexistence with magnesite in the orthopyroxene-hosted fluid inclusions was also found, based on peak at 465±1.8 cm^{-1} (Figure 21b).

Beside the high-density CO_2, dolomite (with no trace of the presence of α-quartz) was identified in the clinopyroxene-hosted fluid inclusions of xenolith Szb 0311 (Figure 22). These fluid inclusions in clinopyroxenes occur along a growth zone of the crystal (Figure 10a).

9.1.2. Raman microspectroscopy at moderately elevated temperature

The main aim of Raman microspectroscopy at moderately elevated temperature was to look for the traces of H_2O in the fluid inclusions. The presence of water in the Earth's deep lithosphere has been documented by numerous studies (Skogby *et al.,* 2006; Walker *et al.,* 2007; Kovács *et al.*, 2010) and it is expected that fluid inclusions trapped at deep lithospheric conditions should contain H_2O in addition to the more commonly reported CO_2. However, before this work direct evidence the presence of water in fluid inclusions from mantle peridotites has been only rarely reported (Roedder *et al.,* 1965; Trial *et al.,* 1984). This contradiction might result from (1) the very high CO_2/H_2O ratio of mantle fluids (e.g., Frezzotti *et al.,* 1992; 2002; Hidas *et al.,* 2010) combined with the low solubility of water in dense CO_2 at room temperature, (2) the difference in wetting properties of the immiscible CO_2-rich and H_2O-rich phases (e.g. Roedder, 1984) preventing recognition of the H_2O-rich phase that occurs as a thin film on the wall of inclusion at room temperature (Roedder, 1984; Bodnar *et al.,* 1985), and (3) the small volume of the submicroscopic H_2O-rich liquid film compared to the size of the excitation laser spot (Bodnar *et al.,* 1985). Any or all of these factors preclude the detection of small amounts of H_2O by Raman spectroscopy at room-temperature (Berkesi *et al.,* 2009).

The inclusions needed to be heated up to detect the H_2O, because the excitation laser could focus strictly on the volumetrically dominant CO_2-rich phase. It is known that the solubility of H_2O increases in the CO_2 with increasing temperature (Sterner and Bodnar, 1990). Upon heating the Raman analysis revealed the presence of H_2O in each fluid inclusion as a characteristic symmetric band corresponding to the dissolved H_2O in the CO_2-rich phase in which peak position varied between 3629-3647 cm^{-1} (Figure 23). The molar percentages of the CO_2, H_2S and the H_2O have already been calculated at 150 ºC (Berkesi *et al.,* 2009), however, without knowing if the fluid are still homogenized, single-phase fluid at this temperature. Considering this, we performed Raman spectroscopy at different temperatures on fluid inclusions from either the Tihany (two samples from the FLUIDRICH xenoliths Tih 0310 (n=10) and Tih 0509 (n=8) as they enclose the highest CO_2 density fluid inclusions) or the Szentbékkálla (Szb 0311, n=11)

peridotites. The goal was to reach the total homogenization temperature (i.e., the temperature at which only one single phase is in equilibrium because there is no longer immiscibility between the CO_2 and the H_2O-rich phase, Figure 24) and obtain the molar percentages of the fluid species from the spectra taken at the same or higher temperature than the total homogenization temperature. Starting from 25 ºC then at 32 ºC, as the critical temperature of the pure CO_2 is 30.98±0.015ºC (precisely 304.1282 K, Span and Wagner, 1996), spectra were taken focusing with the laser on the one visible fluid phase, namely the CO_2-rich phase.

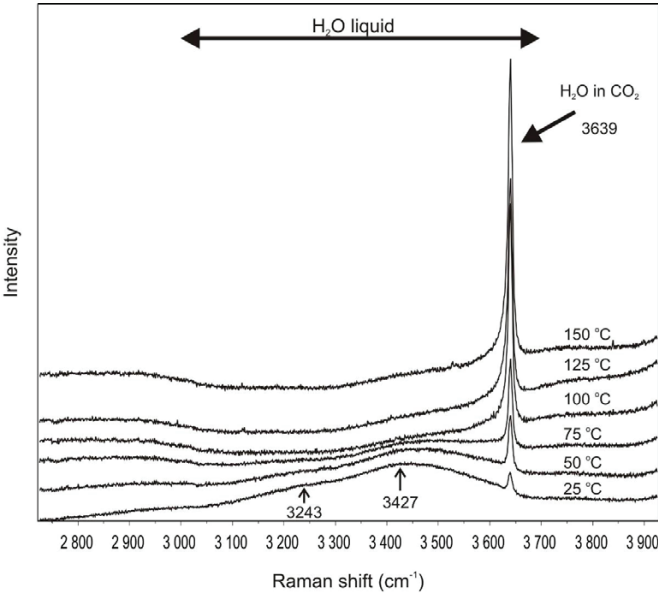

Figure 23. Raman spectra in a range of 2650-3950 cm^{-1} showing the spectra taken at different temperatures on the same fluid inclusion from Tih 0310 xenolith. The corresponding temperatures are indicated on the right side of the spectra. Besides detecting the liquid H_2O (broad band between 3000 and 3700 cm^{-1}), the peak of the dissolved H_2O in the CO_2-rich phase was also detected at room temperature. Upon heating the peak of liquid H_2O continuously disappeared for increasing peak of the dissolved H_2O. Total homogenization was determined when the peak area of the dissolved H_2O did not increase by further heating. The peak position of the dissolved H_2O was the same at each temperature. Peak positions (numbers above or below the peaks) were determined by fitting the peaks with Gaussian-Lorentzian function.

Afterwards the inclusions were further heated and analyzed at each 25 ºC stepwise. As a function of temperature the ratio of the CO_2 total peak area, including the Fermi diad and the hot bands (Rosso and Bodnar, 1995) to the dissolved H_2O peak area were checked. During heating, neither the peak positions of CO_2 nor that of dissolved H_2O was changing. However, their ratio decreased as a result of continuous dissolution of H_2O in the CO_2-rich phase, and vice versa, as soon as reaching/overstepping their total homogenization temperature. Upon further heating the ratio was not changing anymore as the fluid phase is still completely homogenized and a single phase is stable (Figure 24). This fact let us to calculate the bulk molar percentages of the fluid phases within each individual fluid inclusion. Similar method for quantifying the methane in the water has already been performed by Pironon *et al.* (2004). To define more precisely the total homogenization temperature, we performed analyses with 5 ºC stepwise in the possible total homogenization interval provided by the peak area ratios. Total homogenization values varied between 75±2.5 ºC and 155±2.5 ºC in Tihany peridotites and 90±2.5 ºC and 175±2.5 ºC in Szentbékkálla peridotites (Table 5).

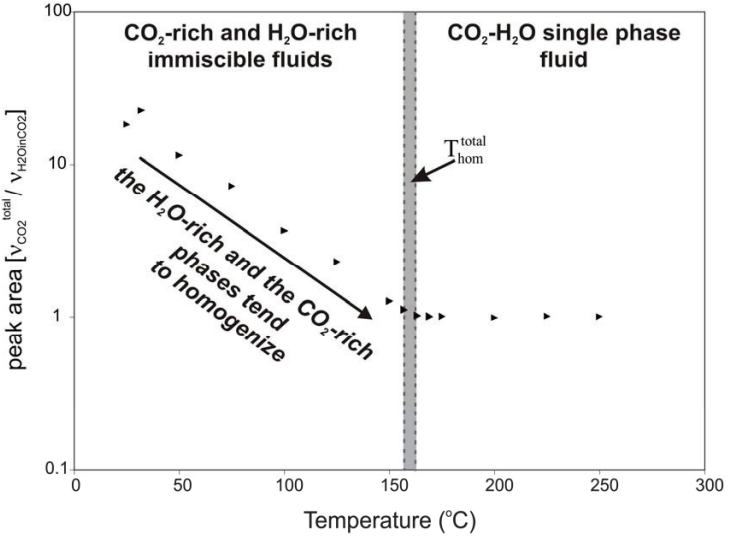

Figure 24. Representative example for the variation of the CO_2/H_2O Raman peak area as a function of temperature in a fluid inclusion from Tih 0509 xenolith. During heating the ratio decreased as a result of continuous dissolution. The minimum temperature of the points when the ratio keeps a constant value was considered as the maximum value of the total homogenization temperature (abbreviated as T_{hom}^{total}).

Molar percentages have been calculated, based on the peak area ratios, by applying the relative Raman cross-sections and calculation method after Dubessy *et al.* 1989; 1992. The total bulk composition of the fluid inclusions in the studied peridotites is shown in Table 5. The maximum H_2O content is not higher than 11 mol% in either the Tihany or in the Szentbékkálla xenoliths, whereas the H_2S content stays around 1 mol%.

Sample	*Host*	*Total homogenization temperature (°C)*		*Bulk fluid composition (mol%)*				*Solid (daughter) phases*
					CO_2	H_2O	H_2S	
Tih 0310	Opx	**n=10**			**n=10**			Mgs, Qtz
		minimum	75	minimum	89	2	0.3	
		maximum	150	maximum	98	11	1	
		average	130	average	95	4	1	
Tih 0509	Opx	**n=8**			**n=8**			Mgs
		minimum	120	minimum	95	2	0.1	
		maximum	155	maximum	98	4	1	
		average	135	average	97	3	0.5	
Szb 0311	Opx	**n=7**			**n=7**			Mgs, Qtz
		minimum	100	minimum	89	0.2	0.3	
		maximum	150	maximum	99.8	11.1	1	
		average	110	average	94	7	0.4	
Szb 0311	Cpx	**n=8**			**n=8**			Dol
		minimum	90	minimum	96	1	0.1	
		maximum	120	maximum	98	3	0.8	
		average	105	average	97	1.7	0.5	
Szb 0311	Ol	**n=4**			**n=4**			Mgs
		minimum	75	minimum	98	0.7	0.1	
		maximum	175	maximum	100	2	0.4	
		average	110	average	99	1.4	0.35	

Table 5. Summary of the results from both the room temperature and the moderately elevated temperature Raman analysis on natural fluid inclusions. Besides the total homogenization temperatures detected, the bulk molar percentages of the fluid species (CO_2, H_2S, H_2O) and the detected daughter phases are also listed. Abbreviations: Opx - orthopyroxene, Cpx – clinopyroxene, Mgs-magnesite, Dol-dolomite, Qtz-quartz

9.2. Raman spectrometry of interstitial glasses

The bubbles hosted by the interstitial glasses were also studied by Raman spectroscopy applying the excitation wavelength of 457 nm. For the reason of the strong effect of the fluorescence on the Raman spectra, the identification of the fluid species in the glass-hosted bubbles were highly difficult compared to the olivine- and pyroxene-hosted fluid inclusions. Only low-intensity peaks of CO_2 have been detected.

10. FOCUSED ION BEAM - SCANNING ELECTRON MICROSCOPY (FIB - SEM)

10.1. General consideration

A focused ion beam (FIB) is a relatively new technique (Dobrzhinetskaya *et al.,* 2003), which has been recently used mostly for TEM (transmission electron microscopy) studies in the earth sciences providing a unique combination of the chemical analysis and microscopic observation (Wirth, 2009) at nanometric scale. The FIB technique has became one of the most promising tools for many geological studies (Dobrzhinetskaya *et al.,* 2001; 2003; 2005; 2006; Heaney *et al.,* 2001; Lee *et al.,* 2003; 2007; Stöckhert, 2003; Wirth 2004; 2009; Obst *et al.,* 2005; Dégi *et al.,* 2010). It is important to emphasize that there are only a few previous works on fluid inclusions using the FIB-SEM (Dobrzhinetskaya *et al.,* 2003; 2005; 2006; Anderson, 2011). The TEM foils cut from fluid inclusions appears to be very useful for detecting nanophases (Dobrzhinetskaya *et al.,* 2006; Wirth and Rocholl, 2003), however, it provides information from a "two dimensional" section, which is not suitable for accurate determination of volume proportion of the solid phases observed in fluid inclusions.

In this chapter the applicability of the stepwise exposure of the fluid inclusions is demonstrated to obtain precise volume proportions of daughter phases. The application of the FIB technique for the studied fluid inclusions aimed to look at solid phases that are found in the fluid inclusion cavity. In this study we show that in fluid inclusions even submicron sized daughter phases can be efficiently studied by FIB-SEM.

By using the focused ion beam technique, inclusions can be exposed and then immediately studied by SEM-EDX. Because of the polishing material filled partly or entirely the fluid inclusion cavity during making the thin section, the exposed fluid inclusions was not possible to study by SEM. Although, we had proofs on the presence of different solid phases by Raman microspectroscopy, however, in the vast majority of the cases there was no information on the volume of the solid phases. These solid phases are so-called reaction products between the trapped fluid and the host minerals (e.g., pyroxenes) resulting in a change of fluid composition relative to the trapped one.

Furthermore, during microthermometry it has been revealed that the smaller inclusions could preserve the highest density CO_2 as a result, they are thought to be the most representative fluids of the trapped composition. The small size, however, provide the poorest visibility in the microscope. Therefore, a high resolution imaging and at least a qualitative chemical analysis are needed to determine the solid phases and their volumes relative to that of inclusion.

10.2. The inclusion exposing procedure

Putting together all of these facts, the following procedure has been used during the FIB-SEM analysis of the fluid inclusions. Either from the Tihany xenoliths (Tih 0311) or from the Szentbékkálla sample (Szb 0311) FIB sectioning and inclusion exposure has been carried out. Inclusions with a size of 3-10 μm close to the surface (maximum 10 microns deep) have been selected. A detailed documentation is crucial before inclusion opening. *The FIB microscope is based on a Ga^+ (liquid/metal) source and operates along the same principle as the scanning electron microscope (SEM), where a beam of charged particles is scanned across a specimen and the resulting images are constructed. However, unlike SEM, the FIB system may produce a high current density beam, which is used for 'in situ' sectioning of the μm-sized particles* (Dobrzhinetskaya *et al.,* 2006). Similarly to the "conventional" SEM studies, a thin carbon coating as a conducting material has been put onto the surface of the sample. After finding the pre-selected area of investigation, an ultra-thin platinum layer was deposited with electron beam for the further orientation in the sample. It is quite important because the sample is then tilted with 52º, therefore the area of interest must be found after tilting again.

Due to the tilting, the Ga^+ ion (which is the milling beam) became perpendicular to the sample surface (Figure 25). Therefore deposition of a thin (1-2 μm) protection layer of platinum onto the area of interest is an obligatory step. The platinum layer plays an important role in protecting the part of the sample from abrasion by the Ga-ion beam (Wirth, 2004). At the beginning of the milling process three large trenches are milled around three edges of the platinum strip (Figure 25). A somewhat deeper trench is milled at the edge of the platinum where the inclusion exposure starts. Since these trenches have been milled by high ion current, a column-like structure is forming on the walls (Figure

25). Using lower ion current allow to make perfectly fine surface. Reduced ion current is used by direct opening of the inclusions, too. Arbitrary size can be cut from the surface exposed by the ion beam and then see the exposed part of the inclusion by SEM and analyze with EDX. The actual progress of the inclusion exposing process is monitored acquiring secondary electron (SE) images of the sample. The interaction of Ga ions with atoms and electrons of the selected area (material) of interest creates secondary electrons that are used for imaging (Figure 25a). On the exposed inclusions both backscattered and secondary imaging were applied at each step of exposing progress.

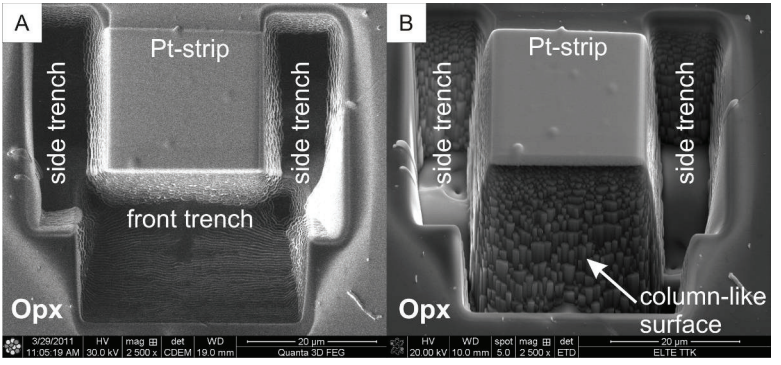

Figure 25. Ion (A) and electron (B) induced secondary electron images of the FIB-SEM. The pictures have been taken before the inclusion exposure followed by the trenches milling procedure. The fluid inclusion selected for FIB –SEM study is below the Pt-strip. For details, see text.

10.3. Identification strategy of the daughter phases

Identification of daughter phases were mostly based on their morphology on the secondary and the brightness on the backscattered electron images together with study of EDS spectra (Figure 27). The latter one has been taken at 10-15 kV (depending on size of phases and elements of interest) and at 0.46 – 2 nA, which allowed the detection of major elements from carbon through oxygen to barium. Because of the small size of the daughter phases in fluid inclusions, the signals detected by EDS detector are mixed

signals, as X-ray from the adjacent area is also detected. To better distinguish the daughter phases from the signals of the host mineral, EDS control spectra from the host mineral were also taken in the proximity and from the same depth of the solid phases after each spectra.

10.4. Results

During fluid inclusions exposure it has been revealed that the position of the fluid inclusion is extremely important for the observation. Figure 26 indicates that the optimal case is when the long axis of fluid inclusion slopes towards to the surface of the host mineral, where the Pt-strip has been deposited. Otherwise it can be filled up by sliced material excluding the possibility to study the daughter minerals referred to as GCM (gallium contaminated material, Figure 26 and 27) accumulation. This observation provides additional consideration to selecting the fluid inclusions for FIB study, moreover helps to decide from which part the FIB sectioning should be started. Note that this is not a crucial phenomenon if the fluid inclusion contains high portion of daughter phases and low volume percentage of cavity. Upon sectioning and therefore exposing the inclusion, several solid phases have been found. Identification of these phases were based on the morphology on SE, the brightness on the BE images and on the EDX spectra. However, because of the small size of the solid phases, signals detected by EDS detector are mixed signals, as x-ray from the adjacent area is also detected. To identify the daughter phases, EDS spectra from the host mineral (orthopyroxene) were taken in the proximity of the solid phases of fluid inclusions after each spectra. Expected solid phases such as magnesite (Figure 27a) and quartz have been found within the fluid inclusions. They have a size between 200 – 2000 nm occurring as clusters on the inclusion walls. Either the magnesite or quartz forms euhedral or subhedral shapes. Furthermore, S-bearing solid phase has also been identified. Its size ranges between 400 -1000 nm and are subhedral in shape. Based on the BS image, this phase can be classified as sulfide (Figure 27b). Due to the sectioning of the fluid inclusions, on the basis of the SE imaging, the volume % of the magnesite and quartz within the inclusion cavity are ranging from 3.3 to 5.0, and from 2.6 to 4.2 vol.%, respectively, whereas the sulfide remains between 1.3 and 1.9 vol.%.

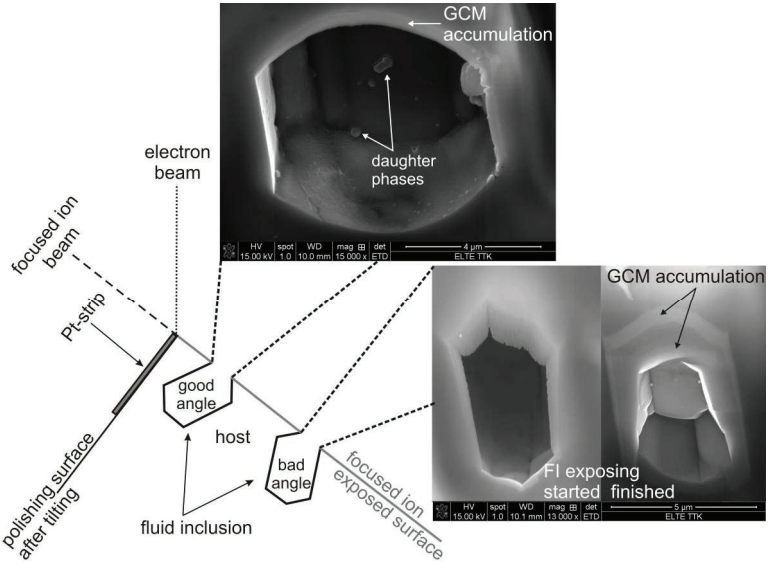

Figure 26. Shematic figure showing the importance of the fluid inclusion position for the best observation. The inclusion having "good angle" is optimal for the FIB sectioning, whereas the one with "bad angle" accumulated by sliced material, referred to as gallium contaminated material (GCM) on the secondary electron images, ruling out the possibility to study the daughter minerals. The secondary electron images document the difference in visibility for the two cases. For details, see the text.

One of the most interesting features observed was a thin film covering the wall of the fluid inclusions studied. They have numerous spherical-shaped holes on the surface as a result of devolatilization, which is typical for volatile-rich glasses (Figure 27c). The EDS analysis revealed that the glass has higher Si/Mg than the host orthopyroxene and richer in Fe, Ca, in sometimes in Al. The glass covers the wall of the inclusions, however, the carbonate-rich cluster are "sticked" directly to the inclusion wall of orthopyroxene. The thickness of the thin glass layer is around 100-200 nm, therefore remains invisible by using any other analytical method (optical microscopy, heating-freezing stage, Raman).

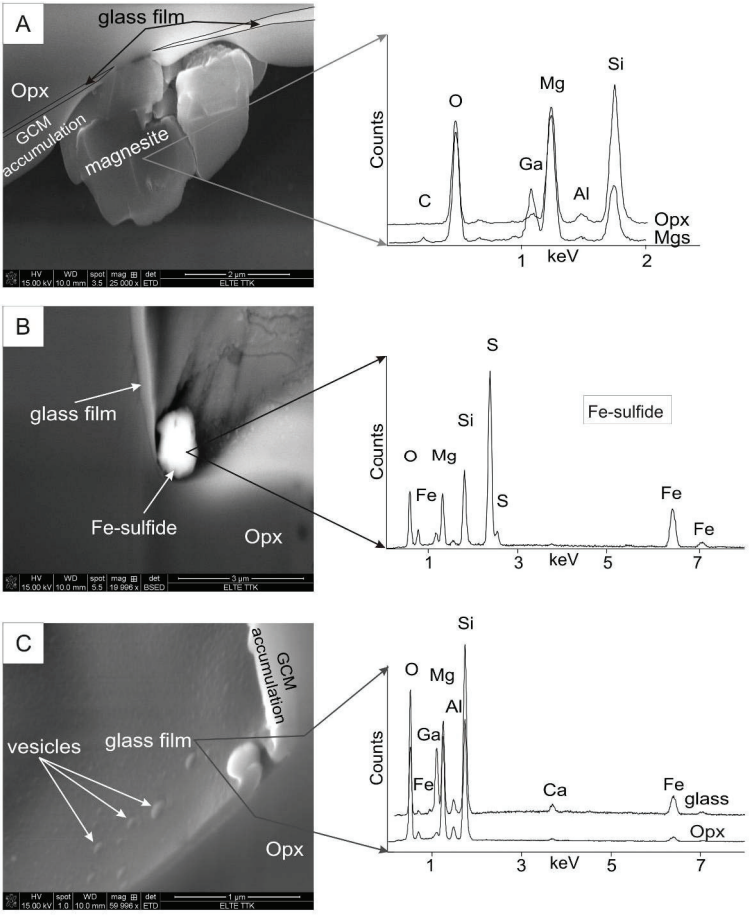

Figure 27. Daughter phases of fluid inclusions identified by applying the FIB-SEM technique. A - secondary electron image and its corresponding EDS spectra of the host orthopyroxene (Opx) and the magnesite (Mgs) daughter phases stuck to the inclusion wall. It can be seen that the magnesite has direct interface with the host orthopyroxene because there is no glass film between them. B - backscattered electron image of Fe-sulfide daughter phase and its EDS spectrum. C - secondary electron image of the glass film having numerous spherical-shaped vesicles on its surface. EDS spectra of glass film and host orthopyroxene are also shown. GCM - gallium contaminated material

11. FUSED SILICA TUBING AND THE APPLICATION OF THE FUSED SILICA FLUID INCLUSIONS

11.1. Preparation of fused silica capillary tubing

The technique itself was established and developed firstly in the USGS lab, Reston (USA) according to Chou *et al.* (2008), additionaly it was adapted in France in G2R lab (Dubessy *et al.* 2009). Many advances, linked to this technique applied to fluid inclusion studies, has been presented in Ding (2010) who performed the fused silica capillary tubing in G2R, Nancy, France. The sealed pure silica glass capillaries are considered as synthetic fluid inclusions and be applicable to the studies of the interest problems related to fluid inclusions and geological fluids (Chou *et al.,* 2008; Dubessy *et al.,* 2009). The main steps of preparation of the silica capillary fluid inclusion (referred to as SCFI in the following) were introduced by Chou *et al.* (2008).

In this work the inner diameter of the SCT is 100 micrometer having round cross section (capillary tubes are provided by Polymicro Technologies©, web: *http://www.polymicro.com*) (Figure 28). Before the sample was loaded by CO_2 or CO_2-H_2O fluids, the outer polyimide layer, in approximate thickness of 20 microns, was removed by burning in hydrogen flame.

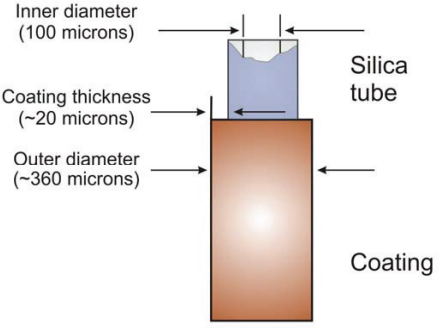

Figure 28. Schematic draw of the silica tube used in this work, provided by Polymicro Technologies©. For details, see text.

In case of CO_2-H_2O fluid inclusions the H_2O (de-ionized water, electrical conductivity: 18 MΩ, ρ=1 g/cm^3) was firstly loaded into the one-end-sealed SCFI. The major steps of liquid loading mechanism have already been presented in Ding (2010). The polyimide removal and the soldering at both end has been done by hydrogene flame (Elmaflame 300 Soldering and Welding Unit). The tube is then centrifuged to force the loaded H_2O into the closed end. To protect the fragile sample tube, it was inserted in a protective glass tube (1.5 mm outer diameter, 1.1 mm inner diameter, and 75 mm long) before centrifugation as proposed by Chou *et al.,* 2008.

Afterwards the capillary was attached to the pressure line that was already "cleaned" by any pollution, air, water, etc. inside the line by vacuum pump (Figure 29), which produces a vacuum down to 0.03 mbar and is permanently connected to the stainless steel line. Meanwhile, all the volumes was continuously kept at 120 ºC to vaporize and evacuate the water adhered to the inner wall of the line, except for the volume of the capillary (Vcap, Figure 29).

Attainment of the vacuum was checked by pressure gauge connected to the volume 2 (V2 on Figure 29). The pollutions, water and the air in the capillary tube was stepwise evacuated by vacuum pump through the pressure line, too. As the Vcap is kept at room temperature, this volume was heated for several minutes by electronically controlled hot air gun (Steinel HL 1910 E) at ~110 ºC under vacuum pumping. To avoid the evacuation of the loaded H_2O, the capillary was put in liquid nitrogen until the level of the H_2O. Afterwards pure CO_2 vapor was loaded into the capillary through the line by filling the different parts, i.e. different volumes (V1-Vcap, Figure 29) separated by the cut-off valves. The inner volumes of the line was previously calibrated by argon gas applying a standard known volume (Ding, 2010), as a result, the volume of Volume 2, 3, 4 and 5 is known (Figure 29). Pure CO_2 was cryogenically added into the SCFI from the CO_2 bottle, its maximum H_2O content is 7 ppm, through the line, as the tube have been put in liquid nitrogen. Pure CO_2 in the SCFI then solidified, causing decrease in CO_2 vapor pressure, as observed by pressure gauge.

The residual gaseous CO_2 in the SCFI is re-evacuated and the open end was sealed by fusion in a hydrogen flame under vacuum using the hottest part of hydrogen flame around 2850 °C (Figure 31b).

Name	Volume (cm^3)
V2	1,886 0 +/- 0,0008 (0,04%)
V3	0,3398 +/ - 0,0018 (0,53%)
V4	1,0264 +/ - 0,0039 (0,38%)
V5	0,6135 +/ - 0,0033 (0,53%)

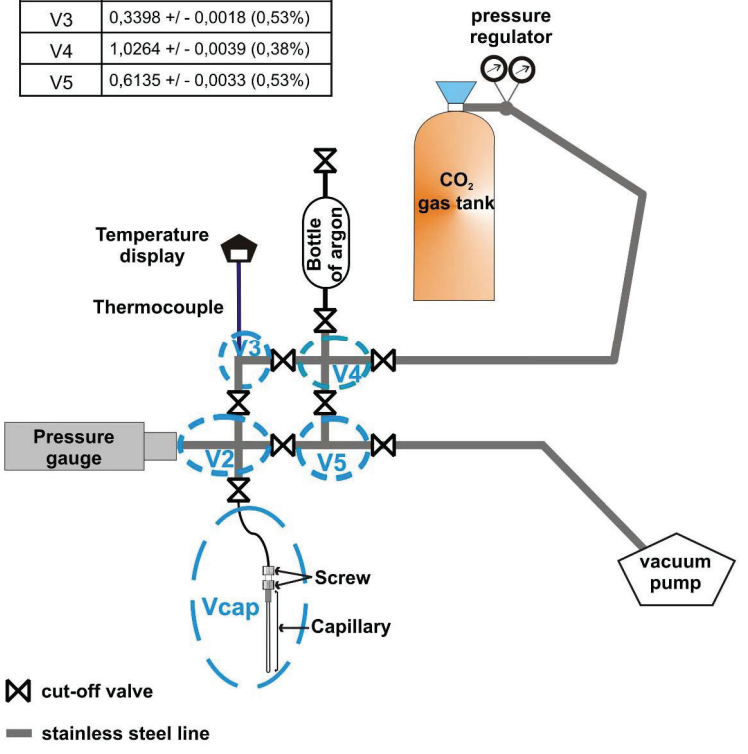

Figure 29. Schematic illustration of the pressure-controlled line built for the preparation of the fused capillary fluid inclusions. The system is available at UMR G2R laboratory, Nancy, France on the basis of the development by Jean Dubessy, Pascal Robert and Junying Ding (Dubessy *et al.*, 2009; Ding, 2010). The table on the top of the figure shows the volume (cm^3) with uncertainty of the different parts of the pressure line denoted as blue dashed curves. Abbreviation: V – volume. For details, see text.

11.2. The determination of volume of the co-existing phases within the silica-fused capillary fluid inclusions (SCFI)

After having removed the both-end-sealed silica-fused capillary fluid inclusions (SCFI) from the pressure line, the volume of the different phases were measured by high precision micrometric stage (MW®) stage both in the cylindrical and the conic part (Figure 30). The length of the SCT inclusions was not higher than 1.5 cm. The volume of the cylindrical part and the conic part were calculated by the volume of the cylinder[1] and the cone[2], respectively. Therefore the volume of the co-existing phases within the silica capillary cell could be calculated (Table 6).

Capillary is put on the micrometric stage and observed under optical microscope and measure the parameters (the radius of the circular face as well as the length, see the footnotes of this page) that are required to calculate both the conic and the cylindrical parts by moving the stage in X or Y directions. The reading uncertainty is ±1μm, as a result, the relative standard deviation (RSD) of the calculated volume of capillary is better than 1% (Ding, 2010). To reduce artifacts, the volumes were measured three times.

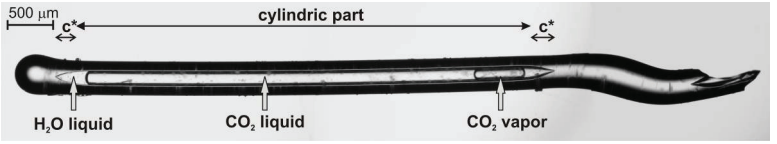

Figure 30. Photomicrograph of a CO_2-H_2O silica-fused capillary fluid inclusion (SCFI) with three phases in coexistence (H_2O liquid, CO_2 liquid and CO_2 vapor). To determine the volume of the different phases, lengths of the phases should be measured and then the volume can be approximated by either cylindrical or conic volume. Abbreviation: c* - conic part.

[1] The volume of a cylinder can be calculated by using the equation $\pi*r^2*l$, where r- radius of circular face (in micrometers), l = length (in micrometers)

[2] The volume of a cone can be calculated by using the equation $1/3*\pi*r^2*l$, where r- radius of circular face (in micrometers), l = length (in micrometers)

As it is illustrated on the Figure 30, the SCFI inclusions give an excellent insight into the phase relations of the carbonic and the aqueous phases, which is highly limited in case of the natural fluid inclusions.

Capillary name	Volume of CO_2-rich phase (in cm^3, at 25°C)				Volume of H_2O-rich phase (in cm^3, at 25°C)
	Single-phase CO_2	Two-phased CO_2		Total volume of CO_2	
	Liquid	Liquid	Vapor		Liquid
0821/1	8.17E-05			8.17E-05	5.05E-07
0821/2	7.72E-05			7.72E-05	6.15E-07
1108/3	7.09E-05			7.09E-05	no visible H_2O
1103/4	6.89E-05			6.89E-05	7.77E-06
1103/2		6.26E-05	2.90E-05	9.16E-05	1.81E-06
1028/2		5.88E-05	9.90E-06	6.87E-05	no visible H_2O
1102/5		6.34E-05	1.69E-05	8.03E-05	no visible H_2O
1108/1	7.74E-05			7.74E-05	no visible H_2O
0818/4		3.21E-05	4.18E-05	7.38E-05	1.71E-07
0907/2	6.98E-05			6.98E-05	1.02E-07
1108/2	8.68E-05			8.68E-05	no visible H_2O
1108/4	6.52E-05			6.52E-05	no visible H_2O
0820/3	9.39E-05			9.39E-05	1.37E-07
1026/1		6.56E-05	2.07E-05	8.63E-05	no visible H_2O
0831/5		5.29E-05	2.95E-05	8.24E-05	2.49E-06
0907/6	8.12E-05			8.12E-05	no visible H_2O
0902/3	8.14E-05			8.14E-05	2.03E-07
0903/1	8.63E-05			8.63E-05	1.02E-07
1025/4	4.74E-05			4.74E-05	no visible H_2O
0821/4		6.75E-05	1.20E-05	7.96E-05	3.28E-07
0820/1		2.05E-05	4.75E-05	6.80E-05	2.81E-07
0831/1		5.29E-05	2.95E-05	8.24E-05	2.49E-06
0903/3	8.67E-05			8.67E-05	no visible H_2O
0831/1		5.29E-05	2.95E-05	8.24E-05	2.49E-06

Table 6. Measured volumes of the co-existing phases within the silica-fused capillary fluid inclusions. All the volumes have been measured three times to reduce the uncertainty. The numbers indicate the average.

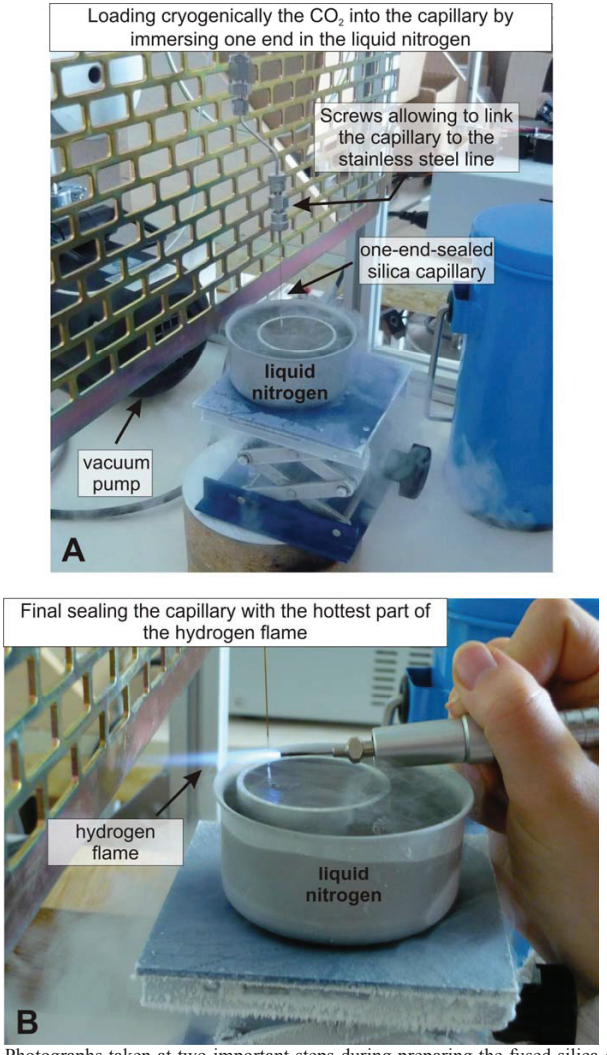

Figure 31. Photographs taken at two important steps during preparing the fused silica capillaries that are attached to the pressure line (Fig. 29). (A) step of cryogenically loading of CO_2 into the capillary tube. (B) step of sealing the capillary tube that consists of CO_2 and H_2O. Photographs were taken in G2R laboratory, Nancy, France. For details, see text.

11.3. Calculate the P-V-T-X parameters of the trapped CO_2 within the SCFI

This is a simplified calculation assuming no effect of absorbed CO_2 on the inner wall of the volumes. The calculation method of P-V-T-X(n) properties for the CO_2 and the H_2O within the fused silica capillary fluid inclusions (SCFI) can be approximated by the ideal gas equation, as follows:

*n(number of moles) * R(gas constant) * T(temperature) = P(pressure) * V(volume)*

where the R is a constant value (83144.72 $cm^3 \cdot mbar \cdot K^{-1} \cdot mol^{-1}$), T is known (393 Kelvin in V2, V3, V4 and V5; whereas ~300 Kelvin in Vcap), pressure is controlled by the pressure gauge. Thus, is it known and the volumes have been calibrated, except the Vcap (Ding 2010). As a result, the Vcap (i.e., volume of the capillary and the corresponding part of the stainless steel line; Figure 29) and number of moles, and therefore the density of the CO_2 can be calculated. The calculation method has been described by Ding (2010).

11.4 Result on the silica capillary fluid inclusions (referred to as SCFI)

On the prepared fused silica capillaries microthermometric heating-freezing experiments and Raman microspectroscopy has been carried out. Basically, routinely used techniques for the natural fluid inclusions have been applied here, too.

11. 4. 1. Microthermometry of fused silica capillaries

Microthermometic observation has been carried out at G2R laboratory, Nancy (using USGS-type heating-freezing gas flow stage) on the CO_2-H_2O SCFI as it is ideal for the observation of different kinds of phase transitions that cannot be or only poorly observed in natural fluid inclusions. The aim was to see phase transitions in the temperature range

from -100 to ~ 200 ºC; out of this temperature range no phase transition was expected. The following phase transitions have been observed.

1 / Phase transitions that were also seen in the natural fluid inclusions:

Melting of solid CO_2 (quadruple point Q3): the studied inclusions, similarly to the natural ones, froze out at around -90 ºC during fast cooling. Hence, at -100 ºC the stable phase assemblage in equilibrium is solid CO_2 (SOL_{CO2}) + CO_2 vapor (VAP_{CO2}) + clathrate (CLA). Upon progressive heating the first phase transition is when SOL_{CO2} melts at the Q3 quadruple point (-56.6 ºC, 0.5 MPa) producing carbonic liquid (LIQ_{CAR}) in the presence of VAP_{CO2} and CLA.

Homogenization of the carbonic phase: the homogenization temperature was recorded when the two, liquid (LIQ_{CAR}) and the vapor (VAP_{CO2}), carbonic phases became one phase at the expense of the other phase. In most cases the homogenization was into the liquid phase (the vapor disappeared). Sometimes critical homogenization was observed when the meniscus separating liquid from vapor gradually fades and disappears upon homogenization at the critical temperature (Kobe and Lynn, 1953; Roedder, 1984). Based on the homogenization temperature of the carbonic phase, calculation of the CO_2 density was completed, which is independent to the calculation described in the Chapter 8. Previously, Ding (2010) has made a calculation of the maximal achievable CO_2 density in the SCFI and stated that "*the maximum resulting density will be near 1.17 g/cm^3. This high density limit shows that capillary will be suitable for the calibration of water dissolved in dense CO_2 like in deep metamorphic fluids or mantle fluids in xenoliths.*"

The temperature-density relations for CO_2 are available in the NIST chemistry webbook database (*http://webbook.nist.gov/chemistry/fluid/*), using the equation of state by Span and Wagner, 1996. The density of the individual studied SCFI is summarized in Table 7.

However, sometimes ice formed in the SCFI, which melted at around 0ºC. This phase transition is not considered on the basis of the bulk composition of the fluid in SCFI (this point will be discussed in the chapter 12.2.1.1.).

2/ Phase transitions that were not seen in the natural fluid inclusions

Melting of clathrate: in the H_2O–CO_2 binary system, clathrate melts in the presence of LIQ_{CAR}, VAP_{CO2}, and H_2O-rich liquid (LIQ_{AQ}) at the invariant quadruple point Q2 at +10 ºC, but clathrate can also melt in the presence of LIQ_{AQ} and either VAP_{CO2} or CO_2 liquid if the pressure at the moment of clathrate melting is not on the CO_2 liquid–vapor curve (Fall *et al.,* 2011). The clathrate always nucleates at the interface between one of the CO_2 phases (either liquid or vapor) and the liquid H_2O phase. During cooling from room temperature at around -30 ºC the clathrate nucleates. Upon progressive heating, the clathrate melts at 10 ºC in the CO_2-H_2O SCFI.

Total homogenization: total homogenization was defined at a specific temperature when the two immiscible phases became completely miscible (i.e. the LIQ_{CAR} homogenizes at the expense of the LIQ_{AQ}). From this temperature, further heating will not result in any phase change within the SCFI, as the total homogenization temperature defines the phase boundary of the immiscibility gap and the single phase field (Diamond, 2001). The total homogenization temperature values was used to independently check the reliability of the total homogenization procedure applied on the natural fluid inclusions by using Raman spectroscopy (Chapter 9) at elevated temperature. The question may arise whether the heating of SCFI can result in volume expansion that causes error in observations. Dubessy *et al.* (2009) presented a thermoelastic model to calculate the deformation of the inner cylinder cavity with temperature and pressure, including a free axial deformation. The authors have been pointed out that volume expansion due to heating is not significant (less than 1% until 400°C and 2 kbar). The total homogenization temperature in the SCFI varied between 67 and 175 ºC, so the effect of volume expansion can be ruled out.

Because of the length of the SCFI, a thermal gradient should be taken into account with the used Linkam stage (THMS 600). However, it is to mention that recently a new heating-freezing stage has been commercialized by the Linkam company (web: http://www.linkam.co.uk) and is suitable for capillaries designed in collaboration with J. Dubessy.

11.4.1. Raman microspectroscopy on the SCFI

11.4.1.1. Raman spectroscopy during stepwise heating

The reliability of the determination of the total homogenization temperature was checked on the SCFI, where the homogenization could be observed in the microscope. The same stepwise heating method has been applied on the natural fluid inclusions (see also the Chapter *Raman microspectroscopy at moderately elevated temperature, chapter 9.1.2.*). The total homogenization temperatures have been determined by two independent ways: (1) by the ratio of the integrated areas of the Raman peak of CO_2 (Fermi diad) and that of dissolved H_2O in CO_2 and (2) by optical observation when the two liquids (LIQ_{CAR} and LIQ_{AQ}) became one phase. The maximum deviation between these two method was 15 ºC, but the always the optically observed total homogenization showed the lower temperature values. This difference can be the result in the thermal gradient that exists in the SCFI because of their length. The fact that Raman spectroscopy detected the total homogenisation temperature at higher temperature supports this idea and reveals that the integrated area ratios are more sensible for determining the total homogenization temperature than the optical observation.

Integrated peak area ratios can be applied for determining the total homogenization temperature and, thus, the bulk composition of the high CO_2/H_2O fluid inclusions, which is typical for the deep lithospheric fluids.

11.4.1.2. Calibration of the peak of H_2O in CO_2 applying the fused silica capillaries

11.4.1.2.1. The analytical setup

Raman analyses were conducted in the Géologie et Gestion des Ressources Minérales et Energétiques (G2R) Lab, Nancy University, Nancy, France. HORIBA Jobin-Yvon LabRam HR spectrometer was used with Laser Physics Ar^+ green excitation laser (λ=514.5 nm) with 1800 grooves/mm gratings, no filter, slit width of 200 μm and a confocal hole at 500 μm. The spectral resolution reached was no higher than 0.35 cm^{-1}. The laser power was set to 200 mW at the source and ~80 mW at the sample. CCD detector (cooled with liquid nitrogen) was also used. Two accumulations of two seconds of acquisition time were used for either the fused silica capillary fluid inclusions or for

signal collection of the neon lamp. The latter one acted as a "standard" during the calibration to optimize the accuracy of the peak position determination. This is very important as the monochromator can be characterized by a nonlinear behavior. Two emission lines from a neon (Ne) calibration lamp that was permanently fixed within the optical path of the microscope were recorded before and after each measurement on the peak position of the dissolved H_2O in CO_2 from the capillaries. The position of each measured Raman line was determined using Gaussian/Lorentzian peak fitting after baseline correction.

11.4.1.2.2. The calibration procedure

The goal was to understand the parameter(s) causing peak shift of the dissolved H_2O in CO_2 that was previously observed on the natural fluid inclusions. The Raman analysis provides useful adds, as "*Raman peak position, peak width and peak intensity reflect the microenvironment of the investigated molecules in terms of the atoms involved in bonding, bond length, bond strength and polarizability* (Lin *et al.,* 2007a and references therein)."

Moreover, we also aimed to calibrate the peak positions. On the basis of the Raman analysis on the natural fluid inclusions, the peak position of the dissolved H_2O in CO_2 mostly depends on the CO_2 (solvent) density. As no peak shift was observed at different temperatures on the individual natural fluid inclusions at fixed density, the temperature effect must have been negligible (smaller than the actual spectral resolution). Even tough, each analysis was performed at fixed temperature, therefore the effect of the temperature in the peak shift can be excluded. Temperature was set to 32ºC. As it is slightly higher temperature than that of critical temperature of the CO_2 (30.98±0.015ºC, Span and Wagner, 1996), the heating effect of the laser illumination did not cause change in CO_2 density.

Neon lamp was used for calibration and two peaks of the neon lines have been selected for the calibration. One peak is at lower wavenumber, whereas the other one can be characterized at higher wavenumbers than the peak of the dissolved H_2O in CO_2 (Figure 32). The Ne lines used for calibration closely bracket the position of the peak of interest (Figure 32). Mc Creery (2000) made a point that at least two reference peaks that

bracket the Raman peak(s) of interest should be used for calibration, because of the 1/ nonlinearity of the spectrometer and 2/ random variations in the mechanical drive 3/ expansion with temperature, and 4/ optical aberrations. These neon lines are determined relative to the 514.5 nm Rayleigh line[3] of the Ar ion laser, *in air*: the 3574.25 cm^{-1} (corresponds to 15860.75 cm^{-1} absolute wavenumber) and 3648.47 cm^{-1} (corresponds to 15786.53 absolute wavenumber) Ne lines were used for calibration (Lide, 1999). Some workers also reported the Raman shifts of neon *in vacuo* (Savoie *et al.,* 1983, Seitz *et al.,* 1993), however we used the wavenumbers of neon calculated in air, as the calibration procedure was done in air instead of in vacuo. Mc Creery (2000) noted that *"since the wavelength analyzer is nearly always operating in air, the appropriate frequency values obtained in air should be used"*. Lin et al (2007a,b) propose the same way upon the calibration of the symmetric stretching band of CH_4 by Raman spectroscopy.

Using the measured peak positions for the band of interest and the measured, as well as the real peak positions for the Ne 3574.25 and 3648.47 cm^{-1} Raman shifts, the corrected (i.e., real) position for the dissolved H_2O peak is given by the following expression (modified after Lin *et al.,* 2007b):

$$\upsilon_{corr}^{H_2OinCO_2} = \frac{4}{5}\times\left[\upsilon_{real}^{H_2OinCO_2} + \left(\upsilon_{real}^{Ne,3574.25} - \upsilon_{measured}^{Ne,3574.25}\right)\right] + \frac{1}{5}\times\left[\upsilon_{measured}^{H_2OinCO_2} + \left(\upsilon_{real}^{Ne,3648.47} - \upsilon_{measured}^{Ne,3648.47}\right)\right]$$

The calculation for the peak position correction is necessary to do as a systematic shift of the neon Raman lines over the course of the day was observed. The maximum shift of the neon emission lines on the same day was not higher than 0.35 cm^{-1}, which is, in turn, the spectral resolution achieved. However, the absolute difference in the relative positions of the two Ne lines remains essentially constant at 74.27 ±0.02 cm^{-1}, both during any single day and from day to day.

This shift is *"most likely in response to slight temperature changes in the laboratory that affect the mechanical and optical characteristics of the spectrometer. Stated differently, the instrument calibration changes with time and the accuracy of peak positions based on calibration only at the beginning and/or completion of an analytical*

[3] Rayleigh line correspond the line of the Rayleigh scattering, which is the elastic scattering. The elastically scattered light has the same frequency and wavelength as the incident beam of light (Nasdala *et al.,* 2004). By convention, the Rayleigh line is set at zero Raman shift.

session may be questionable" (Lin *et al.,* 2007b). Therefore, to get as accurate peak position as possible, each individual capillary analysis was started to have taken a spectrum of the neon lines then it was immediately followed by the capillary sample analysis.

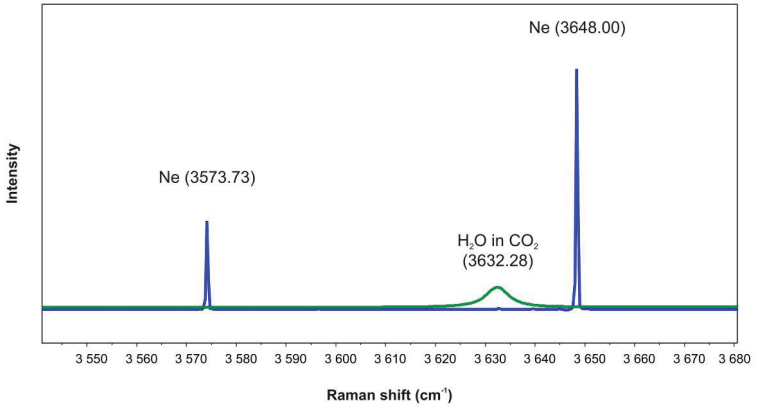

Figure 32. Raman spectra showing how the calibration procedure looks like. The peak of dissolved H_2O in CO_2 (green curve) together with neon peaks (blue curve) are presented. The neon peaks bracket the calibrated peak of interest.

11.4.1.2.3. Results

To our best knowledge, this is the first study to calibrate the position of the peak of the dissolved H_2O in CO_2 and see the dependence of the peak shift, too. The results of the calibration are summarized in Table 7. Both the peaks of CO_2 and the dissolved H_2O in CO_2 were proved in capillaries having different CO_2-density and more or less the same CO_2/H_2O ratio. It is known that the distance between the two peaks of the Fermi diad (splitting) of CO_2 (Figure 21c, and Figure 22) is density/pressure dependent (Wright and Wang, 1973). By comparing the distances between the two peaks of the Fermi diads to the peak of the dissolved H_2O, it has been revealed that the higher the distance in Fermi diad the lower the wavenumber of the dissolved H_2O.

The peak the dissolved H_2O shows a systematic shift to lower wavenumber with increasing density (pressure). The peak shifts to lower wavenumber with the dissolved H_2O Raman peak shows a smooth and continuous shift to lower wave number as a function of CO_2 density (Figure 33). Additional feature is the peak broadening of the dissolved H_2O with decreasing CO_2 density. The FWHM (acronym of Full Width at Half Maximum) of the dissolved H_2O peak ranges from 5.33 to 11.61 cm^{-1} (Table 7, Figure 33)

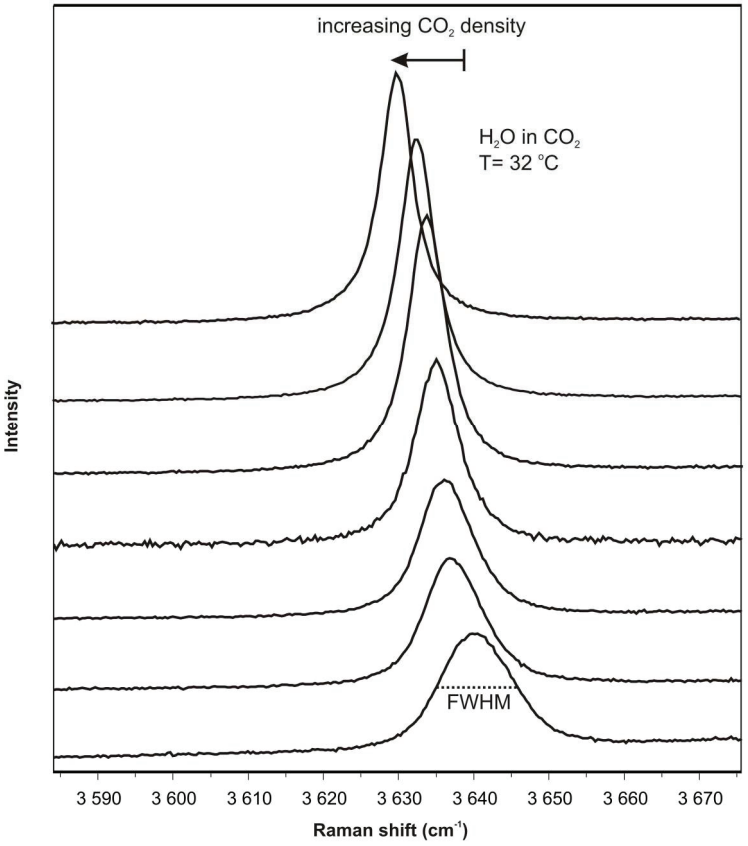

Figure 33. Representative Raman spectra in the spectral region of 3580 and 3680 cm^{-1} showing the CO_2 density dependent position and FWHM (acronym of Full Width at Half Maximum) of the peak of the dissolved H_2O in CO_2. The spectra were taken at constant temperature on the *silica fused capillary fluid inclusions.*

Capillary name	υ^{CO2} (Fermi diad)		Δ Fermi diad	$\upsilon^{neon\ line1}$	$\upsilon^{neon\ line2}$	$\upsilon^{H2OinCO2}$	FWHM H_2OinCO_2	ρ_{CO2}
	upper band (υ^+)	lower band (υ^-)						
	cm^{-1}							g/cm^3
0821/1	1281.07	1385.91	104.84	3573.73	3648.00	3633.48	6.16	0.92
0821/2	1281.07	1385.91	104.84	3573.73	3648.00	3634.16	6.84	0.84
1108/3	1279.65	1385.13	105.48	3573.64	3647.90	3631.17	5.48	1.08
1103/4	1281.07	1385.91	104.84	3573.39	3647.66	3635.18	7.01	0.77
1103/2	1281.55	1385.91	104.36	3573.39	3647.66	3636.90	8.21	0.52
1028/2	1281.55	1385.91	104.36	3573.39	3647.66	3635.87	7.65	0.68
1102/5	1281.55	1385.91	104.36	3573.39	3647.66	3636.55	7.53	0.64
1108/1	1279.61	1384.96	105.35	3573.39	3647.66	3632.45	5.33	1.02
0818/4	1282.04	1386.39	104.35	3573.39	3647.66	3638.26	10.24	0.47
0907/2	1282.52	1386.39	103.87	3573.39	3647.66	3639.63	11.46	0.61
1108/2	1279.13	1384.48	105.35	3573.39	3647.66	3630.74	5.48	1.12
1108/4	1279.13	1384.48	105.35	3573.39	3647.66	3631.08	5.48	1.09
0820/3	1280.58	1385.44	104.86	3573.39	3647.66	3634.5	6.70	0.77
1026/1	1281.55	1385.44	103.89	3573.39	3647.66	3636.21	8.61	0.60
0831/5	1281.55	1386.39	104.84	3574.08	3648.34	3633.81	6.16	0.88
0820/2	1283.98	1387.34	103.36	3574.08	3648.34	3640.65	11.61	0.46
0907/6	1281.55	1386.39	104.84	3573.73	3648.00	3635.53	7.53	0.94
0902/3	1281.07	1385.91	104.84	3573.73	3648.00	3634.16	6.16	0.86
0903/1	1280.58	1385.91	105.33	3573.73	3648.00	3632.79	5.48	0.76
1025/4	1281.07	1385.91	104.84	3573.73	3648.00	3634.16	6.16	-
0821/4	1282.52	1386.39	103.87	3573.73	3648.00	3637.24	9.02	0.50
0820/1	1283.01	1386.87	103.86	3573.73	3648.00	3639.98	11.48	0.47
0831/2	1282.52	1386.87	104.35	3574.73	3648.68	3635.63	7.53	-
0903/3	1281.07	1385.91	104.84	3574.08	3648.34	3632.44	6.02	-
0831/1	1283.01	1386.87	103.86	3574.08	3648.34	3637.23	9.56	-

Table 7. Summary data of the results of the fused silica capillary fluid inclusions. Abbreviations: FWHM H_2O in CO_2 - Full Width at Half Maximum of the Raman peak concerning the dissolved H_2O in CO_2-rich phase, υ^{CO2} - relative Raman peak position of the CO_2, $\upsilon^{neon\ line1}$ - relative Raman peak position of the neon line at lower wavenumber than that of dissolved H_2O in CO_2, $\upsilon^{neon\ line2}$ - relative Raman peak position of the neon line at higher wavenumber than that of dissolved H_2O in CO_2, Δ Fermi diad – distance in peak position between the upper and the lower band of CO_2, ρ_{CO2} – density of CO_2. Definition of 'upper' (υ^+) and 'lower' (υ^-) band of the CO_2 is given from Rosso and Bodnar (1995).
For details, see text.

12. DISCUSSION

12.1. The formation the studied xenoliths

12.1.1. Orthopyroxene-rich poikilitic textured rocks of the Tihany peridotites

In this chapter the formation mechanism of the orthopyroxene enrichment and the poikilitic texture observed in the Tihany peridotites will be discussed. Though the studied rocks have similar texture (Table 1; Figure 4), there are clear differences in their mineral geochemistry between the NOFLUID xenolith group and the other two fluid inclusion-bearing, FLUIDPOOR and FLUIDRICH, xenolith groups (Figure 11 and 15). The FLUIDPOOR and FLUIDRICH xenoliths were most probably overprinted by cryptic metasomatism (will be discussed in chapter 12.2.3) likely followed by the formation of the texture. Here we are focusing on the petrographic feature of the whole xenolith series however, regarding the geochemistry, only the results of the NOFLUID xenoliths have been taken into account. The studied rocks from Tihany have poikilitic texture with high modal proportion of orthopyroxene characterized by coarse-grained orthopyroxene-rich lherzolites and harzburgites (Figure 4; Table 1). In addition, in the studied rocks the modal orthopyroxene/clinopyroxene ratio varies between 1.9 and 16.7 (6.8 in average, Table 1) which values are significantly higher compared to ‘‘normal’’ (average) subcontinental lithospheric mantle in which this ratio is around 2 (Downes et al, 1992; Griffin et al., 1999).

In the followings a possible formation mechanisms of the orthopyroxene enrichment will be discussed compiling with the high orthopyroxene/clinopyroxene ratio and their major and trace element geochemistry. The olivines enclosed in orthopyroxene (Figure 4) are either euhedral or subhedral providing their pre-existence of orthopyroxenes. These olivines usually coexist with spinel. According to chemical composition of the coexisting olivine and spinel (high mg-number of the olivine and the cr-number of the spinel (Figure 12), they may represent an “ancient” relict phase for the lithospheric mantle beneath Tihany, which is characterized by strong geochemical depletion (i.e., ~ 20-25% melt extraction; Figure 34). Thus, such a high degree of partial melting may

amount to the formation of residual orthopyroxene-rich rock as a result of metamorphic differentiation at relatively high pressure (~2 GPa) (e.g. Boyd, 1989). The high mg-number and the low Al_2O_3-content of the studied orthopyroxenes (Appendix 1) may support this idea. Nevertheless, the orthopyroxenes and clinopyroxenes petrographically (Figure 4c and d) and geochemically (Appendix 1, Figure 16) suggest their co-precipitation. Thus, if a melt extraction as a result of partial melting causes the orthopyroxene enrichment, it should be reflected on the chondrite-normalized REE pattern of the clinopyroxene, too. The clinopyroxenes in the NOFLUID peridotites have U-shaped chondrite-normalized REE pattern (Figure 16) that might have formed by the LREE enrichment of a depleted mantle (e.g., Melcher *et al.,* 2002). However, during the onset of partial melting in the forsteritic olivine–enstatitic orthopyroxene–diopsidic clinopyroxene ternary system, representing an average lithospheric mantle rock, the composition of the first melt droplet is clinopyroxene-rich (Morse, 1980), hence when the partial melting commences dominantly the clinopyroxene starts to melt. Following this point, degree of partial melting was modeled based on the REE content of the clinopyroxenes in the Tihany xenoliths (Appendix 4a). Calculations have been carried out on the NOFLUID clinopyroxenes characterized by chondrite-normalized U-shaped pattern (Figure 16). Because of the LREE-enrichment must have been resulted in a late stage process than the melt extraction, the calculation was to model only the MREE and HREE concentration by means of partial melting. Melt extraction assumed either batch or fractionated melting to calculate the composition of residual clinopyroxene. As a starting composition, average BBHVF protogranular xenoliths, representing the dominant non-metasomatized subcontinental lithospheric mantle in this region (Embey-Isztin *et al.,* 1989; Downes *et al.,* 1992), was used. Normann's (1998) calculation method was applied involving partition coefficients of clinopyroxenes from McKenzie and O'Nions (1991). Irrespectively to the melting mode, the result of the calculation is demonstrated on chondrite-normalized REE diagram (Figure 34) revealing that at least 13-15 vol.% of partial melting is required to achieve such high MREE-depletion that observed in the studied NOFLUID clinopyroxenes.

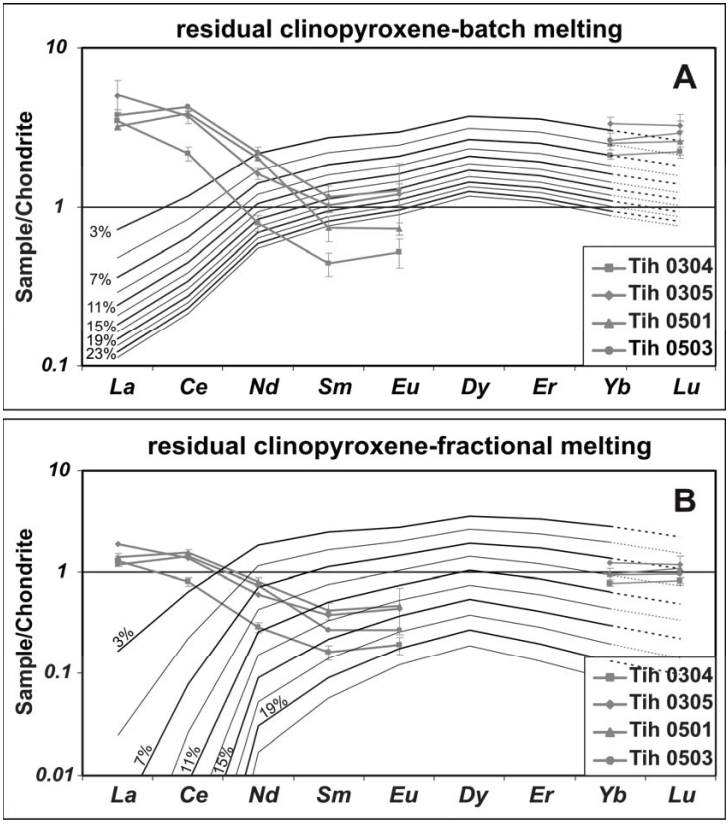

Figure 34. C1 chondrite-normalized (Anders and Grevesse, 1989) rare earth element diagram showing the REE pattern of the calculated, hypothetical residual clinopyroxene composition (black curves) modeling either A) batch melting or B)_fractional melting developed by Normann (1998). Partition coefficients of Mckenzie and O'Nions (1991) and average of protogranular peridotites from the same volcanic field as source composition from Downes *et al.* (1992) were taken for the calculations. As no information of Lu concentration is available in the suspected source, the model composition of this element is extrapolated (dashed part of the black curves). Each black colored curve indicates different degree of partial melting: the numbers to the left of the thickened curves correspond to the degree of the calculated degree of melting. The grey curves are normalized values of U-shaped clinopyroxenes in the NOFLUID xenoliths (Tihany). The symbols' values are the averages. The figure shows that the most MREE-depleted clinopyroxenes (xenoliths Tih 0304, 0305, 0501, 0503) cannot be considered as a residue of partial melting since more than 25% degree of partial melting produce complete consuming of the clinopyroxenes.

Almost all clinopyroxenes would have been melted out at this calculated grade of depletion, resulting in absence clinopyroxenes in the mantle rocks. . Contrarily, the modal abundance of the clinopyroxenes in the studied peridotites is up to 6 vol.% (Table 1). Consequently, the high degree of partial melting resulted in the formation of the studied orthopyroxene and clinopyroxene can be excluded.

Another process should have been responsible for the orthopyroxene enrichment in Tihany peridotite series. This implies that formation of orthopyroxene is resulted in melt infiltration into the original olivine-rich peridotite. Kelemen *et al.* (1992) stated that orthopyroxenites containing more than 32 wt.% of orthopyroxene cannot represent mantle residues and may have formed by reaction of olivine-rich peridotite with a siliceous melt as follows:

$(Mg,Fe)_2SiO_4$ (olivine) + SiO_2-rich melt = $(Mg,Fe)_2SiO_6$ (orthopyroxene) + SiO_2-poor melt equation #1

In connection with this implication other explanations for the orthopyroxene-enrichment are linked to melt/peridotite interaction: (a) the circulation of slab-derived melts or fluids formed during the dehydration process or the partial melting of the subducting oceanic crust, and (b) the circulation of Si-oversaturated alkaline melts or sub-alkaline melts (Dantas *et al.,* 2009). The high pressure melting experiments confirmed the idea 'a' (Rapp *et al.,* 1999) showing that partial melting of "metamorphic" basalts from a subducted oceanic crust could produce SiO_2-rich liquids with compositions close to adakites (Defant and Drummond, 1990). Such liquids could react with peridotites to form orthopyroxenites or orthopyroxene-rich rocks (e.g. Arai *et al.,* 2003, Grove *et al.,* 2003, Bali *et al.,* 2007). According to idea 'b', orthopyroxenes are reaction products between relatively highly evolved alkaline melts and mantle olivines. Indeed, the percolation of alkaline mafic magmas in the mantle involves local silica enrichment of the metasomatic agent by orthopyroxene digestion (e.g. Wulff- Pedersen *et al.,* 1996; Arai *et al.,* 2006) and provides orthopyroxene crystallization according to the reaction:

Olivine + clinopyroxene + orthopyroxene (1) + evolved alkali liquid → orthopyroxene (2) + spinel equation #2

Because of the absence of the positive correlation of the modal percentages between orthopyroxene and spinel, the equation #2 as a responsible reaction for the orthopyroxene

enrichment can be ruled out. In contrast, the orthopyroxene was growing at expense of the olivines as our petrographic observations shows (Figure 4). Thus, such a formation of orthopyroxene can be explained by the reaction shown in equation #1.

In summary, it is highly likely that formation of the studied ortho- and clinopyroxene is resulted in a silicate melt - peridotite reaction, which is also supported by the occurrence of the orthopyroxenes in bends (Figure 4a, b) usually together with the clinopyroxene. However, the question is arisen what kind of melt could have resulted in chemical characters of the pyroxenes. These chemical characters are: 1/ the relatively low Al_2O_3 (<3 wt.%) (Appendix 1a) and high SiO_2 (55.8 wt.% in average) (Appendix 1a) concentration of the orthopyroxenes together with their high mg-number (0.91-0.92) (Figure 11; Appendix 1a), 2/ the U-shaped C1 chondrite normalized REE pattern of the clinopyroxenes. Orthopyroxenes with similar compositions have been studied by Arai *et al.*, 2003; Grove *et al.*, 2003 and Bali *et al.*, 2007 who have interpreted their formation by the equation#1. Similar clinopyroxenes to our studied ones can be crystallized from a high SiO_2 and MgO content "boninite-like" melt (e.g., Falloon *et al.,* 2008). In accord, previously studied orthopyroxene-rich websterites from the BBHVF showed similar compositional range for orthopyroxene and clinopyroxenes (Bali *et al.,* 2007) (Figure 15 and 16) and concluded the that orthopyroxene enrichment are related to a migration of a boninite-like melt in the subcontinental lithospheric mantle. The low La_N/Lu_N ratio in contrast to the higher La_N/Sm_N is also a characteristic geochemical feature for the former migration of boninite-like melt in the upper mantle (Boily and Dion, 2002; Falloon *et al.,* 2008; Manikyamba et al 2005; Bali *et al.,* 2007). Additional boninite-like characterizations are the depletion in Ti, slight enrichment in Sr and Pb in primitive mantle-normalized trace element patterns (Falloon *et al.,* 2008). These phenomena can also be observed in the studied Tihany xenoliths (Figure 15). Assuming the modal orthopyroxene enrichment caused by a suspected boninite-like melt, process drive by equation#1 should be responsible for the olivine consummation and orthopyroxene-formation. We propose that the clinopyroxenes were not involved in this olivine-consuming reaction, but crystallized from the boninitic melt. Thus, the NOFLUID Tihany peridotite xenoliths indicate that the formation of the poikilitic texture, the high modal proportion of the orthopyroxenes, and the U-shaped chondrite normalized REE

pattern of clinopyroxenes are the result of the same metasomatic process, where the metasomatic agent is a boninitic melt.

Boninites are an important magma type as they have the highest H_2O contents among the magmatic suites in suprasubduction environment and require the most depleted mantle wedge sources (Falloon *et al.,* 2008). Boninites magmas are a rare but important of many supra-subduction zone ophiolites and fore-arcs (Rogers *et al.,* 1989). As boninite petrogenesis requires a combination of high temperature and shallow depths in the mantle wedge (Crawford *et al.,* 1989), the presence of boninitic melt has important implications for the tectonic setting (Crawford *et al.,* 1989). Thus, it is plausible that the studied Tihany mantle xenoliths went through a boninite melt metasomatism, which can be linked to a subducted slab existed during tectonic evolution of Pannonian Basin. Kovács *et al.* (2007) has already purposed that subduction-related geochemical characteristics in Tertiary calc-alkaline igneous rocks and orthopyroxene-rich mantle xenoliths from the Bakony-Balaton Highland Volcanic Field are inherited from an early subduction event of either the Budva-Pindos or Vardar Ocean during the age Mesozoic–Paleogene. We have no data for the time of formation of the studied NOFLUID ortho- and clinopyroxene to confirm or reject of this proposal, but the textural and geochemical similarities to the xenoliths studied by Bali *et al.* (2007) is obvious.

12.1.2. The composite xenolith from Szentbékkálla

Understanding the mechanisms of the clinopyroxenite and the lherzolite wall rock formation in from of the Szb 0311 composite xenolith from Szentbékkálla (Figure 6) in details is not the major goal of this thesis. Therefore, here I discuss briefly the results of the petrographic observation (Figure 6, 7, 8, 9) and the major element characteristics (Figure 13 and 14; Appendix 2) in this sample. The composite xenolith can be described by two main formation events when the lherzolitic wall rock and when the clinopyroxenite vein formed suggesting that the formation of the clinopyroxenite is a young process. The clinopyroxenite vein has interstitial glass (Figure 7) and primary silicate melt inclusions are hosted in clinopyroxenes and spinels which is clear evident for magmatic origin. The melt, from which the clinopyroxenite crystallized, migrated towards the lherzolitic wall rock part and caused modal metasomatism. It is supported by

the clinopyroxenes which occur as coronas around the orthopyoxenes in the lherzolitic part of the xenolith (Figure 8e and f) and show variation in the major and trace elements (Figure 13 and 14; Appendix 2) depending on the distance from the clinopyroxenite vein. As a result, the lherzolitic part is petrographically (Figure 8 and 9) and geochemically (Figure 13 and 14; Appendix 2) effected by the clinopyroxenite-crystallizing melt. Consequently, the evolution of the lherzolite prior to the formation of the clinopyroxenite vein can be hardly constrained and out of the scope of this study.

12.2. Fluid inclusions

The negative crystal shape of the studied fluid inclusions (Figure 5 and 10) suggests textural equilibrium between the inclusion and its host phase (Viti and Frezzotti, 2000). The formation of negative crystal shape takes most probably longer time than the duration of the transport of the xenoliths to the surface (Roedder, 1984; Szabó and Bodnar, 1996; Dégi *et al.,* 2009). Moreover, the rapid pressure change during uplift also does not favor the formation of negative crystal shape morphology (Bodnar, 2003). Thus, the possibility of the entrapment of the studied fluid inclusions during transport to the surface is unlikely. Furthermore, the high fluid density, maximum CO_2 density is around 1 g/cm^3 in each sample studied, (Figure 20; Appendix 6a) within the fluid inclusions suggest that the entrapment of the fluids happened at lithospheric mantle conditions prior to sampling by the melt of alkali basalt.

Not surprisingly, each fluid inclusion encloses CO_2-dominant fluid as the dominance of CO_2 is common feature in negative crystal shaped mantle xenolith enclosed fluid inclusions (e.g. Andersen and Neumann, 2001; Berkesi *et al.*, 2009; Frezzotti *et al.,* 1992; 2002; Frezzotti and Peccerillo, 2007; Roedder, 1965; 1983; Hidas *et al.,* 2010). Moreover, up to the recent years, the generally accepted composition for the fluid within the inclusions was the "pure" or "nearly pure" CO_2 (Roedder, 1984; Andersen and Neumann, 2001). Even though, this work shows a number of additional phases and components found in the fluid inclusions.

To describe the trapping composition of the fluid is of fundamental to understand the properties of the fluid. In the followings, the role and the effect of the presence of the different phases and components in the studied fluid inclusions will be discussed.

12.2.1. The presence of H_2O in the fluid inclusions

The Raman microspectroscopy at moderately elevated temperature has proven the presence of H_2O in the fluid inclusions with the relative amount of up to X_{H2O}=0.11 (Table 5). Results of this thesis suggest that the studied fluid inclusions, trapped at subcontinental lithospheric mantle conditions, contain H_2O from 0.2-11 mol% and have

<1 mol% H_2S (Table 5). Thus, the fluid system can be no longer treated as pure or nearly pure CO_2 fluid system. Therefore, the assumption of a pure CO_2 (H_2O-free) fluid in lithospheric mantle environment should be reconsidered. The room temperature Raman spectroscopy and microthermometry alone are not suitable for detecting H_2O in such fluid inclusions (Berkesi *et al.*, 2009). Instead, it can be approximated by CO_2-H_2O system. This conclusion, in turn, has important implications concerning the geochemical and geodynamic evolution of the Earth's deep lithosphere, as H_2O, consequently CO_2-H_2O fluid, can play a great role in melting processes (e.g. Grove *et al.,* 2006), in dissolving and transporting elements (e.g. Newton and Manning, 2000; Antignano and Manning, 2008), as well as in deformation mechanisms (Soustelle *et al.,* 2010).

12.2.1.1 The effect of the addition of small amount of H_2O to pure CO_2 in microthermometry

In this chapter the microthermometric observations (chapter 8, Appendix 6) are re-considered taking into account the possible phase transitions of the CO_2-H_2O system with high X_{CO2} compared to the pure CO_2.

Precisely, the microthermometric characteristics of fluid having compositional range of **$0.002<X_{H2O}<0.852$**, based on the compositional classification of Diamond (2001), is introduced in the followings, as all the studied fluid inclusions fall in this compositional range. Meanwhile, considering the theoretical phase stabilities and phase transitions in this compositional range, I will make a comparison of the visible/observable phase transitions detected during microthermometry in either the natural (chapter 8) or in the capillary fluid inclusions (chapter 11.4.1).

12.2.1.1.1. Freezing

The fluid inclusion microthermometry starts with very fast cooling down to below -100 ºC. This is important to force the fluids, which is liquid and/or vapor at ambient temperature according to the bulk density of the carbonic phase, to surpass the metastable barrier and nucleate CO_2 solid (SOL_{CO2}) in equilibrium with CO_2 vapor (VAP_{CO2}).

Depending on the X_{H2O} in the fluid inclusions, additionally ice or clathrate[4] (CLA) nucleates. For the same reason of metastability, during fast cooling of the inclusions the clathrate crystallizes abruptly after surpassing a metastable barrier at around −35 °C (Roedder, 1963), and the remaining carbonic liquid freezes out at around −90 °C. In case of the studied fluid inclusions, solely the nucleation of SOL_{CO2} was observable, no clathrate out freezing was detectable optically. As a result, at -100 ºC the theoretical stable phase assemblage in true equilibrium is SOL_{CO2} + VAP_{CO2} + CLA lying on the 3-phase curve nr. 1 (Figure 35), although, CLA could not be seen in the natural inclusions.

However, there are metastable phase assemblages because ice may often form as a reason of bulk disequilibrium. "*Even when clathrate finally crystallizes it grows instantaneously to a large size, the fluid inclusion may not always be restored to an equilibrium state. Ice is often observed to crystallize after a few degrees of further subcooling but both carbonic liquid and vapour persist to even lower temperatures, in defiance of the phase rule; thus, four phases coexist over a temperature interval in a binary system! In effect, in real inclusions, clathrate apparently builds a physical barrier to diffusion between the carbonic and aqueous phases, so that at low temperatures the inclusion may be considered to consist of two separate bulk compositions*" (Diamond, 2001). Similarly to the theoretical consideration, in some capillary fluid inclusions studied ice also formed as a result of bulk disequilibrium.

[4] A clathrate compound or cage compound is a chemical substance consisting of a lattice of one type of molecule trapping and containing a second type of molecule. A clathrate hydrate, in particular, is a special type of gas hydrate, in which a lattice of water molecules encloses molecules of a trapped gas (e.g., CO_2). The nominal composition of CO_2 clathrate is $CO_2 * 7.5H_2O$, although it is non-stoichiometric and its composition varies slightly with pressure and temperature (Diamond, 2001).

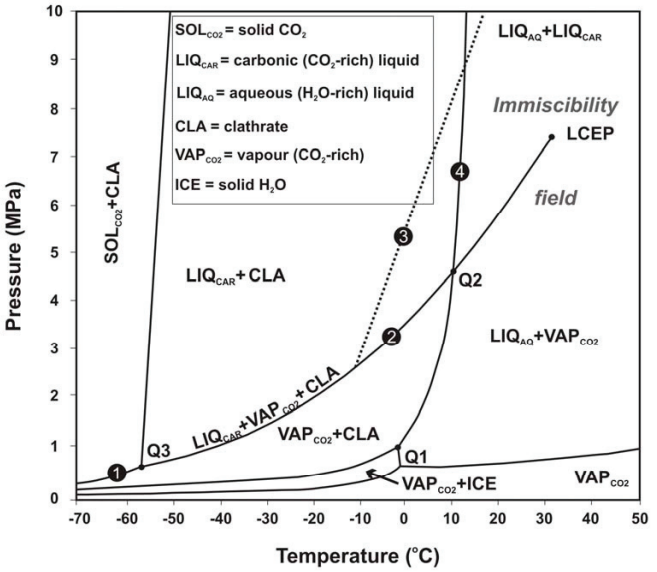

Figure 35. Pressure–temperature phase diagram of the system H_2O–CO_2 at low temperatures, modified after Fall et al. (2011). At quadruple point Q1 four phases, namely aqueous liquid, CO_2 vapor, CO_2 clathrate and H_2O ice (solid), coexist. At quadruple point Q2 also four phases, namely aqueous liquid, CO_2 vapor, carbonic liquid, and CO_2 clathrate, coexist. At quadruple point Q3 the following four phases, namely solid CO_2 solid, CO_2 vapor, carbonic liquid and CO_2 clathrate, coexist. On the divariant curve nr. 1 CO_2 solid coexists together with CO_2 vapor and clathrate, whereas on the curve nr. 2 a carbonic liquid, CO_2 vapor and clathrate coexist. Curve nr. 3 shows a schematic isochor of the carbonic phase. Curve nr. 4 is the clathrate dissolution curve.

12.2.1.1.1. Heating

Theoretically, upon progressive heating from -100 ºC the first phase transition observed is when SOL_{CO2} melts producing carbonic liquid (LIQ_{CAR}) in the presence of VAP_{CO2} and CLA at the Q3 quadruple point (-56.6 ºC, 0.5 MPa) (Figure 35). The temperature at Q3 quadruple point is only 0.04 ºC lower that that of pure CO_2 (Span and

Wagner, 1996), therefore this very slight difference is immeasurable by microthermometry. The observed melting temperatures in either the natural fluid inclusions or in the SCFI were at around -56.6 ºC (abbreviated as T_{melt}) (Appendix 6). Still, in the natural fluid inclusions the CLA was unobservable when SOL_{CO2} melted, therefore the assumption of pure CO_2 (Span and Wagner, 1996) is reasonable, but misinterpreting for the composition of fluid phase filled by the inclusion cavity.

Upon further progressive heating, based on the topology of the phase diagram of the H_2O–CO_2 binary system (Figure 35), CLA melts in the presence of LIQcar, VAP_{CO2}, and LIQ_{AQ} at the invariant quadruple point Q2 at +10 °C. However, at this time CLA can also dissolve in the presence of LIQ_{AQ} and either VAP_{CO2} or LIQcar if the pressure at the moment of CLA dissolution is not on the CO_2 liquid–vapor curve (Fall *et al.,* 2011). The CLA melting could be easily detected in the SCFI (chapter 11.4.1.). Contrarily, after melting of the SOL_{CO2}, in the studied fluid inclusions during progressive heating no clathrate but only a LIQcar and VAP_{CO2} could be seen, despite the fact that the fluid system should lie on the 3-phase curve (LIQcar+ VAP_{CO2}+ CLA, curve nr 2 on Figure 35).

The subsequent observed phase transition was the condensation of the vapor phase, in other words the homogenization of the CO_2 into the liquid phase (abbreviated as Th_{car}) (Appendix 6). If the homogenization temperature of the carbonic phase is lower than temperature corresponding to Q2 (<10 ºC, on the 3-phase curve nr. 2) (Figure 35), the homogenization of the VAP_{CO2} into the LIQ_{car} occurs in the presence of CLA. The majority of the studied natural fluid inclusions homogenized below 10.0 ºC somewhere on the line nr. 2 on Figure 35. After the homogenization of the carbonic phase, the fluid "follows" its way on the P-T diagram on the corresponding isochor of the carbonic phase (curve nr. 3 on Figure 35). CLA starts to dissolve when the isochor intersects the clathrate dissolution curve (curve nr. 4 on Figure 35), therefore melts at higher pressure and slightly higher temperature than that of Q2 (Figure 35). However, the slight temperature difference in this case cannot be distinguished by microthermometry. CLA dissolution/melting was easy to detect in the capillary fluid inclusions, however remained undetected in the natural fluid inclusions.

On the higher temperature (> 10 ºC) side of the P-T phase diagram, assuming that the carbonic phase is already homogenized, the stable phase assemblage must be LIQcar + LIQ_{AQ} (Figure 35). The reason is that at the given P-T two immiscible, a carbonic (CO_2-rich, referred to as LIQ_{car}) and an aqueous (H_2O-rich, referred to as LIQ_{AQ}) liquid are in equilibrium with each other. Further heating enables continuous increase in mutual solubility, progressing towards the total homogenization temperature (T^{tot}_{hom}) of the fluid system (Figure 24). Depending on the bulk composition and density, the T^{tot}_{hom} occurs when crossing the isopleth (and isochor) of the bulk fluid on the solvus of the miscibility gap (Figure 24). In other words, during heating there is an expansion of the LIQcar to fill the entire volume of inclusion cavity. Note that this T^{tot}_{hom} nominates the temperature when LIQ_{car} and LIQ_{AQ} became single phase i.e., homogenized. However, this refers not to the temperature when there is only one phase in the fluid inclusion, as daughter phases (like carbonates, quartz, glass film, sulfide) (Figure 27) still exist at the determined T^{tot}_{hom}.

No visible information could be collected upon further heating on the T^{tot}_{hom} of the natural fluid inclusions, solely in the capillaries. On higher temperatures, when leaving the solvus, one phase remain stable at fixed composition and density.

Owing to the unfavorable optical characteristics and having a small inclusions (<5 μm, Figure 20) the presence of the H_2O cannot be confirmed in mantle xenoliths-hosted fluid inclusions by microthermometry. The fused silica capillary fluid inclusions played an important role in controlling the analyses and in trying to infer the T^{tot}_{hom} by applying the Raman microspectroscopy at moderately high temperature.

12.2.1.2. The density of fluid inclusions considering the presence of H_2O within the fluid inclusions

It is widely known that the fluid inclusions allow the estimation the P-T conditions of entrapment (Roedder, 1983; 1984) if the fluid density is known. On the basis of the fluid composition and the density, the isochor on the P-T plane can be drawn. Owing to the isochor of the bulk fluid and entrapment temperature value, the minimum trapping pressure is possible to calculate. In the previous chapter difficulties about finding traces for the presence of the H_2O during microthermometric study were described. Assuming

that there is no H_2O in the fluid inclusion and then drawing the isochor on the basis of the Th_{car} for the pure CO_2 system, error in the calculated trapping pressure may be caused (Figure 36). Hurai (2010) has also emphasized this problem and stated that "*depending upon the EOS (equation of state) used, the described method overestimates the trapping pressure by 14.2– 21.8 MPa for the CO_2–H_2O inclusion sealed at 180 °C and 100 MPa within the two-phase immiscibility field. This discrepancy is caused by differing slopes of the curved isochoric trajectory of the two-phase CO_2–H_2O fluid and linear isochoric trajectory of the monophase pure CO_2 fluid.*"

The question arises whether the underestimation of the amount of the H_2O may cause significant error in density calculation. Berkesi *et al.* (2009) present molar percentages for the fluid species at 150 ºC without knowing at that moment if at this temperature the fluid is already homogenized. Later, however, stepwise method (chapter 9.1.2.; Figure 24) is demonstrated to determine both the total homogenization temperatures (Table 5) and the bulk molar percentages of the fluid species including the water. The diversity of H_2O content (0.2-11 mol%; Table 5) in the individual fluid inclusions can be considered as a result of 1) the non-completion fluid/host carbonation reaction (see chapter 12.2.2.1.), and 2) H_2O loss at those P-T conditions where the CO_2-rich and the H_2O-rich immiscible phases coexisted. Contributions of Bakker and Jansen (1991) and Severs *et al.* (2007) draw attention to the latter effect in experiments of quartz-hosted inclusions up to 800ºC. Therefore, the detected H_2O content should be regarded as a maximum value in the first consideration as a part of CO_2 is bounded in magnesite, hence the calculated molar percentages for the CO_2 is underestimated, consequently H_2O is overestimated. In contrast, the detected H_2O content should be regarded as a as a minimum value in the second consideration as part of H_2O has been lost, compared to the trapping composition (for instance as a result of decrepitation, Figure 5 and 10). These results suggest that even 11 mol% H_2O may remain undetected or underestimated if heating experiments compiled with Raman microspectroscopy is not applied. In our study, as emphasized in the previous chapter, during microthermometry solely the characteristic phase transitions of the CO_2–rich phase was observed. Consequently, the calculation of the minimum trapping pressure by the intersection of the isochor of the pure CO_2 with the two-pyroxene equilibrium temperatures (Brey and Köhler, 1990) is proposed. However,

without adding the water content to the fluid system, the calculation of minimum trapping pressure might include error. To see the effect of small amount of H_2O in minimum trapping pressure estimation, firstly, the density shift was calculated between a pure CO_2 and a COH supercritical fluids with 89 mol% CO_2 and 11 mol% H_2O using the equation of state of Duan and Zhang (2006).

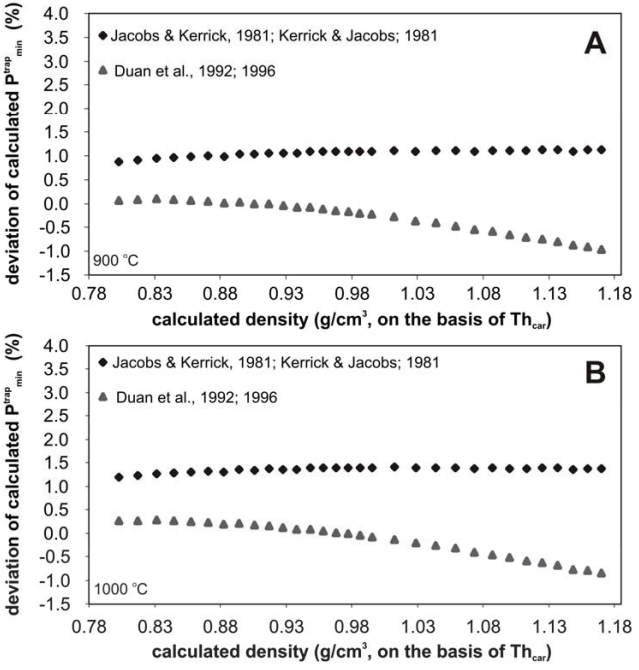

Figure 36. Demonstration of the effect of invisible H_2O on bulk density. On the x axis the calculated densities of modeling pure CO_2 is shown in a range of 0.80-1.17 g/cm^3 on the basis of the visible homogenization temperature of the CO_2 vapor and the carbonic liquid (abbreviated as Th_{car}). The y axis indicate the deviation (in percentages) of the calculated minimum trapping pressures from the pure CO_2 system to the system 89 mol% CO_2 – 11 mol% H_2O using different equation of states (1/Duan *et al.,* 1992 and 1996 and 2/ Kerrick and Jacobs, 1981; Jacobs and Kerrick; 1981). Diagram A shows minimum trapping pressures with an intersection of the isochors at 900 ºC, and diagram B demonstrates minimum trapping pressures of the isochors for 1000 ºC.

Calculation software available on http://calc.geochem-model.org/Pages/CO2H2O.aspx. Carbon-dioxide densities from 0.80 to 1.17 g/cm^3 (Figure 36) have been taken into account as lower densities are usually not applied in minimum trapping estimation. Eleven mol% H_2O causes bulk density decrease of about 0.03 g/cm^3 in a supercritical fluid, compared to that of pure CO_2. Then its effect on minimum trapping pressure was calculated both at 900 ºC and 1000 ºC. Equations of state developed by Duan *et al.,* 1992 and 1996 (D) and Kerrick and Jacobs (KJ) (1981) and Jacobs and Kerrick 1981 (JK) were applied and tested (Figure 36), using the calculation software package FLUIS (Bakker, 2003). No significant change between 900 and 1000 ºC was observed. More or less irrespectively of the density, the equation of KJ and JK show lower minimum trapping pressure than the pure CO_2 density with a maximum deviation of 1.4 % (Figure 36) that corresponds to 0.14 kbar shifted value. In contrast, using the Duan equations at lower densities (0.8-0.97 g/cm^3 at 900 ºC and 0.80-0.90 g/cm^3 at 1000 ºC) the H_2O-bearing system provides lower pressures, whereas at higher densities (0.98-1.17 g/cm^3 at 900 ºC and 0.91-1.17 g/cm^3 at 1000 ºC) the H_2O-bearing system gives slightly higher pressure values (Figure 36). At lower densities the H_2O-bearing isochors decrease the pressure values with a maximum of 0.3 % (corresponding to 0.01 kbar). At higher density calculations the H_2O-bearing isochors provides higher pressures than the pure CO_2 isochors. In case of Duan equation, the higher the density the higher the deviation; the maximum shift is 0.10 kbar (corresponds maximum shift of 1 %) (Figure 36).

To summarize these results, it can be outlined that the minimum trapping pressure determination using the pure CO_2 model may have a maximum error of about 1.5 % compared to CO_2-H_2O system that contain 11 mol % H_2O. Moreover, it is also suggested that the use of the appropriate state equation has higher relevance than not-detected water up to 11 mol %.

Total homogenization experiments were carried out on the xenoliths Tih 0310, Tih 0509 and Szb 0311, providing the highest density CO_2-rich inclusions (Appendix 6) Adding the bulk water content to fluid system, the bulk density and the minimum trapping pressure value was recalculated using the equation of state by Duan *et al.* (1992, 1996). In xenolith Tih0310 the modified (highest) bulk density is 1.06 g/cm^3 which is

0.03 g/cm^3 lower than modeling with pure CO_2 (Appendix 6), whereas the minimum trapping pressure is 0.85 GPa (0.01 higher than modeling with pure CO_2). Having lower bulk H_2O content (4 mol%) in xenolith Tih 0509, the minimum trapping pressure did not change, the modified bulk density decreased from 1.12 to 1.11 g/cm^3 modeling pure CO_2 and CO_2-H_2O system, respectively (Appendix 6). Similarly to the Tih 0310 sample, in the Szb 0311 xenoliths the highest H_2O content, orthopyroxene-hosted fluid inclusions have 0.03 g/cm^3 lower bulk density than calculated for pure CO_2 system. Its consequent modified minimum trapping pressure value is only 0.02 GPa higher than in the pure CO_2 - system (Appendix 6).

12.2.1.3. The role of H_2O in density estimation by Raman microspectroscopy

As it was presented in the Chapter 11.4.1.2, the CO_2-density dependence on the Raman peak position of the dissolved H_2O in CO_2 liquid has been discovered (Figure 33; Table 7). To our best knowledge this is the first time to calibrate the position of this peak and also observe the density-dependence of the peak shift.

The microthermometric measurements revealed that the smallest inclusions can be considered to be the most representative inclusions (Figure 20) in both density and composition. In 2-3 micrometer sized fluid inclusions the visibility of the phase transitions by heating-freezing experiments is extremely poor. Thus, the dissolved H_2O peak wavenumber may be used to calculate the density of the CO_2-dominant liquid in a fluid inclusion. If so, it may provide the CO_2 density at higher accuracy than given by using the CO_2 density estimation on the basis of the distance between the Fermi diads (Kawakami *et al.,* 2003; Fall *et al.,* 2011). The reason is that in deep lithosphere fluid inclusions in the vast majority of the cases the density of *liquid* CO_2 must be determined. It means density range from about the critical density (0.467 g/cm^3, Span and Wagner, 1996) until the density close to the CO_2 triple point (~1.178 g/cm^3, Span and Wagner, 1996). This work has data in the range of the 0.47 and 1.12 g/cm^3 (Table 7). Therefore, the density range of interest is about 0.65 g/cm^3. In that range the distance between the CO_2 Fermi diads (that is widely used for density determination) varies from 103.36 to 105.48 cm^{-1} (Table 7), in other words in a range of 2.12 cm^{-1}. In contrast, for the same density range the peak of the dissolved H_2O in the CO_2 varies in a wavenumber range of

9.92 cm^{-1}, between 3630.73 and 3640.64 cm^{-1} (Table 7). Accordingly, the liquid CO_2 density may be determined at higher accuracy when taking into account the peak of the dissolved H_2O in CO_2, instead of the distance in the Fermi diads of CO_2. However, for the proper calibration further study is required.

The results from this study may be used on any properly calibrated Raman microprobe to estimate the density/pressure in a fluid inclusion. These data, in turn, may be used to construct the fluid isochor corresponding to the original formation conditions.

The peak broadening of the dissolved H_2O with decreasing CO_2 density, shed lighted the influence of CO_2 molecules on the perturbation of the energy of the symmetric stretching of the H_2O in CO_2. (Dubessy et al, 2010)

12.2.2. The density of fluid inclusions considering the formation of the daughter phases

As it was pointed out in the previous chapters, fluid inclusions are generally thought to be as a closed system that provides useful information on trapping conditions (Roedder, 1984). However, it is also emphasized that the pressure estimation for the entrapment in mantle fluids are only an indication, as it can be regarded as a minimum value (Roedder, 1984; Andersen and Neumann, 2001). Nevertheless, many processes may cause fluid loss resulting in density decrease and underestimating the trapping condition. During uplift of the mantle rocks, because of the rapid decrease of external pressure occurring at high temperatures, fluid pressure exceeds the confining pressure and inclusions may decrepitate. We observed partial or total decrepitation on the fluid inclusions (Figure 5 and 10), which indicate fluid loss after fluid entrapment. Moreover, previous studies pointed out the nanoscale evidences of fluid loss, such as diffusivity (e.g., Severs *et al.,* 2007) and the formation of nanoscale fractures across the inclusions (Bakker and Jansen, 1990; Viti and Frezzotti, 2000).

However, decrease of fluid density is also obvious phenomena due to precipitation of solid phase(s) (i.e., daughter phases), which is/are denser than the residual fluid (Connolly and Cesare, 1993). Previously, graphite (Bergman and Dubessy, 1984; Cesare, 1995), halite (Frezzotti *et al.,* 2002), and OH-bearing solids (Frezzotti *et al.,* 2010; Pintér *et al.*, 2011) as daughter phases, whereas diamond, carbonates (Frezzotti and Peccerillo,

2007) as heterogeneously trapped phases were already described in deep lithospheric fluid inclusions.

In the studied pyroxene-hosted fluid inclusions carbonates (Figure 21 and 22) and quartz (Figure 21) were detected and identified as formed via the reaction of the CO_2-rich fluid and the host orthopyroxene after entrapment. This implication is the most reasonable process as 1) the main divalent cations of the carbonates detected by Raman spectroscopy are always the same than that of host phases. Magnesite was found in orthopyroxene-hosted fluid inclusions (Figure 21), whereas dolomite was detected in clinopyroxene-hosted fluid inclusions (Figure 22), 2) in case of the optically visible solid phases, the fluid:solid volume percentages is the same (Figure 5), and 3) carbonate or quartz were found only in the fluid inclusions but not as constituent minerals in the xenoliths, 4) the FIB exposure of the orthopyroxene-hosted fluid inclusions show a direct interface between the magnesite and the host mineral (Figure 27). In other words, the carbonation reactions can be considered as post-entrapment processes, which will be described and its P-T dependence determined.

12.2.2.1. Carbonation in the orthopyroxene- and clinopyroxene-hosted fluid inclusions

As all the products and reactants have been detected in the orthopyroxene-hosted fluid inclusions, the following carbonation reaction has taken place (Holland and Powell, 1990; Koziol and Newton; 1995; Matas *et al.,* 2000):

$MgSiO_3$ (enstatite) + CO_2 = $MgCO_3$ (magnesite) + SiO_2 (quartz) equation #3

In the clinopyroxene-hosted fluid inclusions, however, only dolomite was found. Formation of the daughter phase(s) can be explained by the following carbonation reaction:

$CaMgSi_2O_6$ (diopside) + $2CO_2$ = $CaMg(CO_3)_2$ (dolomite) + $2SiO_2$ (quartz)
equation #4

Up to now, precise volume properties only of the orthopyroxene-hosted daughter phases are available due to the limited number of FIB exposure (n=4) and a very few cases where the host phases are visible by microscopic observation. The exact determination of the magnesite and the quartz separately was challenging because the carbonate and the quartz occurs together at the wall of the inclusion, as clusters. According to the calculation using both the SE and BE images (Figure 27), the volume percentages of the magnesite (maximum of 5 volume %) and the quartz (maximum of 4.2 volume %) are nearly equal in the exposed fluid inclusions. It is also suggested theoretically, considering the mass balance for the equation #3. Mass balance calculation was performed to describe the density of fluid from the initial state until the reaction proceeds. The assumption is reasonable as a result of detected magnesite and quartz in the orthopyroxene-hosted CO_2-rich fluid inclusions. The details of the mass balance calculations can be found in Appendix 7. The sum of the volume percentages of the magnesite and quartz was set to a maximum of 10 vol.% because it was the highest value detected. If we re-calculate the CO_2-density (considering pure CO_2) before the reaction took place, the maximum addition for the CO_2-density was ~0.05 g/cm^3.

An interesting phenomenon that has been revealed is that the presence of 11 mol% H_2O, which decreases the density with maximum of 0.03 g/cm^3, (details in the chapter 12.2.1.2.) and the carbonation reaction, which increases the density with a maximum of 0.05 g/cm^3 nearly counterbalances the CO_2 density. Therefore, the CO_2 density estimation in the studied fluid inclusions is acceptable when approximating pure CO_2 and having no information of the volume properties of the carbonates. As the volume ratio of the phases may be different in other mantle xenolith-hosted fluid inclusions to determine the exact CO_2-density, both the bulk H_2O and the exact volume properties of the daughter phases, if there are, should be determined.

12.2.3. Formation of daughter phases – when and where?

12.2.3.1. P-T dependence of the carbonation reaction within the fluid inclusions

In this chapter possible pressure-temperature properties for the carbonation reactions (equations #3 and #4) within the fluid inclusions will be considered. The P-T position of

these two reaction curves are illustrated on the Figure 37 with different bulk fluid composition (i.e. various X_{CO2} in a CO_2-H_2O fluid system) in a range between X_{CO2}=1 and X_{CO2}=0.5. The curves have been calculated by Perple_X 6.6 software (Connolly, 2009) applying the database and solution models of Holland and Powell (1990). Schreinemakers projection[5] of the phase relations as a function of X_{CO2} by using the calculation method of Connolly and Trommsdorff (1991) onto the P-T plane has been done in the system MgO-SiO_2-CO_2-H_2O-CaO (CaO only for the clinopyroxene-bearing system), excluding all the phases except for enstatite, magnesite, quartz and the CO_2-H_2O mixture in Figure 37 A, whereas diopside, dolomite, quartz and the CO_2-H_2O mixture in Figure 37B. It is clearly seen that the position of the reaction curves of the equation #3 and #4 are the same. Therefore, they can be considered together.

Based on experimental studies (Johannes, 1969; Koziol and Newmann, 1995) and interpretation of natural paragenesis (Trommsdorff and Connolly, 1990), the reaction curve of equation #3 is calibrated in a range between 490-890 ºC and 2-17.8 kbar (with no data in a range between 490 and 638 ºC), respectively (Figure 37). On the other hand, the position of the reaction curve in the P-T space for the MgO-SiO_2-CO_2 system is thermodynamically constrained (Holland and Powell, 1990, Matas *et al.,* 2000).

Based on the experimental results of Koziol and Newmann (1995), the reaction curve of equation #3 at 890 ±2 ºC, which is the maximum temperature of their experimental study, corresponds to 17.9 kbar (±200 bar) (Figure 37) Even if the temperature is lower than the calculated equilibrium temperatures for the upper mantle beneath the study area, Tihany and Szentbékkálla (dash-dotted square on Figure 37), the corresponding pressure seems to be too high in the mantle: the spinel/garnet lherzolite is around 16 kbar at 900 ºC (O'Reilly and Griffin; 1996). Thus, the reactions described by equation #3 and.#4 taking place at mantle conditions can be ruled out, due to all the studied xenoliths are equilibrated in the spinel lherzolite stability field (Table 1, 2).

Another possibility is the nucleation of the carbonates and the quartz inside the inclusion during the transport to the surface, i.e. during the upwelling of the basaltic melt

[5] Schreinemakers' method is a geometric approach used to determine the relationships of reaction curves that intersect at an invariant point in multicomponent systems. This method produces topologically correct bundles or sequences of reactions around an invariant point and can be applied to a wide variety of phase diagrams such as P-T, T-X, activity-activity, etc. (Zen, 1966)

(Figure 37). In this case the duration of the ascent and the heating effect of the uprising alkali basaltic lava should be taken into account. The shortest duration of reaction of equation #3 is 30 hours (Koziol and Newmann, 1995), corresponding to the highest experimental P-T conditions. This is in agreement with the calculated ascent time for spinel lherzolites from the same (Dégi *et al.,* 2009) and another (Szabó and Bodnar, 1996) Pliocene–Pleistocene alkali basaltic volcanic field in the Pannonian Basin. However, the basaltic melt that carries the xenoliths to the surface is characterized by higher temperatures than peridotites at lithospheric mantle condition. On the higher temperature side of the reaction curve in the pressure-temperature phase diagram (Figure 37), the stable phases are always the reactants (i.e. the host minerals and the CO_2 fluid), which suggests no reaction. Thus, it is proposed that the reaction could have happened after carrying the xenoliths to the surface and during relatively fast cooling of the host basaltic melt (Figure 37). The reactions commenced when the fluid inclusion-bearing xenoliths, hosted in the cooling lava, reached the temperature at about 400-600 ºC (Figure 37) when intersecting the reaction curves of equation #3 or #4. Therefore, at ambient condition, thermodynamically the stable phase assemblages are the reaction products without presence of CO_2. However, this latter component exists within the inclusions even if all the host phases are in excess. Therefore, we propose that the reaction has not been completed. This might be as a result of the nucleation/condensation of such phases that acted as a "barrier" between CO_2 and the host orthopyroxene, excluding the completion of the reactions (Eq #3 and Eq #4). Our FIB exposures clearly revealed a thin glass film covering the entire wall of the inclusions (Figure 27c). This glass film is missing from those parts of the wall, which shows direct interface between the daughter phases (e.g., carbonate and quartz) and host orthopyroxene (Figure 27a). Consequently, the "precipitation" of the glass film excluded the completion of equation #3. Carbonates, together with CO_2 was previously found in other mantle xenolith-hosted fluid inclusions (e.g., Andersen and Neumann, 2001 and references therein; Frezzotti et al., 2002; Frezzotti and Peccerillo 2007). Therefore, on the basis of the studied fluid inclusions it is suggested that the presence of glass phase in mantle fluid inclusions can be a general phenomena that excludes the completion of the carbonation reaction (Eq#3 and Eq#4 in this study).

12.2.3.2. The possible compositional range of the CO_2-H_2O fluid during the reaction

On the Figure 37 the position of the reaction curve at lower X_{CO2} (<0.5) is not indicated as the fluid inclusions have a residual CO_2-rich fluid characteristics. Moreover, according to the experimental results of Johannes (1969) in the system MgO-SiO_2-CO_2-H_2O at 2000 bars at varying temperatures (up to 660 ºC), the stability fields of the assemblages where enstatite and magnesite coexist are limited to low H_2O ($X_{H2O} \geq 0.13$) contents. Furthermore, Lüttge and Metz (1991) has proven the reversibility of the reaction equation #3 at fluid composition $X_{CO2} \geq 0.9$ in the system CaO-MgO-SiO_2-CO_2-H_2O at 500 MPa.

In addition, low H_2O content is also supported in both experiments above by the fact that no Raman peak of OH-bearing phases (serpentines or any other Mg-phyllosilicates) were found. Consequently H_2O should be completely dissolved in the CO_2-dominated fluid when the reactions of equation #3 and #4 take place. Taking into consideration the determined total homogenization (T^{hom}_{tot}) temperatures of the fluid inclusions by high-temperature Laser Raman microspectroscopy, the temperature when equation#3 and #4 took place should be higher than ~150 ºC.

In this study moderately high temperature Raman analysis has been carried out at a maximum temperature of 275 ºC. Upon heating the fluid inclusions, above the homogenization temperature of the carbonic phase, the fluid follows P-T path of the corresponding isochor. Theoretically, when the isochors intersect the reaction curves of equations #3 and # 4 (Figure 37) at a given temperature, the reaction products start to be consumed to form CO_2 and the host pyroxene phases. This may cause problems by determining the total homogenization temperature (T^{hom}_{tot}) of the fluid phase (note that T^{hom}_{tot} only refers to the homogenization of the aqueous liquid into the carbonic liquid, as emphasized in the chapter 12.2.1.1), as during heating CO_2 is continuously produced. However, as demonstrated on Figure 37, the isochors of the corresponding densities range between 0.6 and 1.12 g/cm^3 (the density range of the fluid in this study) intersect the reaction curves at ~400 – 780 ºC. This is at least 175 ºC higher than the temperature at which we heated the inclusions up. Consequently, during heating (up to ~275ºC,

chapter 9.1.2.) the inclusions did not intersect the reaction curves of equation #3and #4. Therefore, CO_2 had not been produced during heating.

Figure 37. (next page) Pressure (GPa)-Temperature (ºC) diagram. The black arrow shows an approximate P-T path of the upwelling basaltic melt/lava. Diagram A shows the red reaction curve of enstatite (En) + CO_2 = magnesite (Mgs) + quartz (Qtz) determined by Johannes (1969); Trommsdorff and Connolly (1990); Holland and Powell (1990); Koziol and Newmann (1995) is shown. Diagram B shows the green reaction curve of diopside (Di) + CO_2 = dolomite (Dol) + quartz (Qtz) determined by Holland and Powell (1990). The curves with numbers correspond to the isochors of the CO_2. The dashed-dotted rectangle indicates the possible P-T ranges where the mantle rocks and the fluids might have equilibrated in the lithospheric upper mantle. This was determined by the equilibrium temperatures (using the geothermometer by Brey and Köhler (1990) and by the spinel (Spl)/garnet (Grt) and the plagioclase (Pl)/spinel (Spl) transition curves (O'Reilly and Griffin, 1999). X_{CO2} is the molar fraction of CO_2 in the hypothetical CO_2-H_2O fluid system. For details, see text

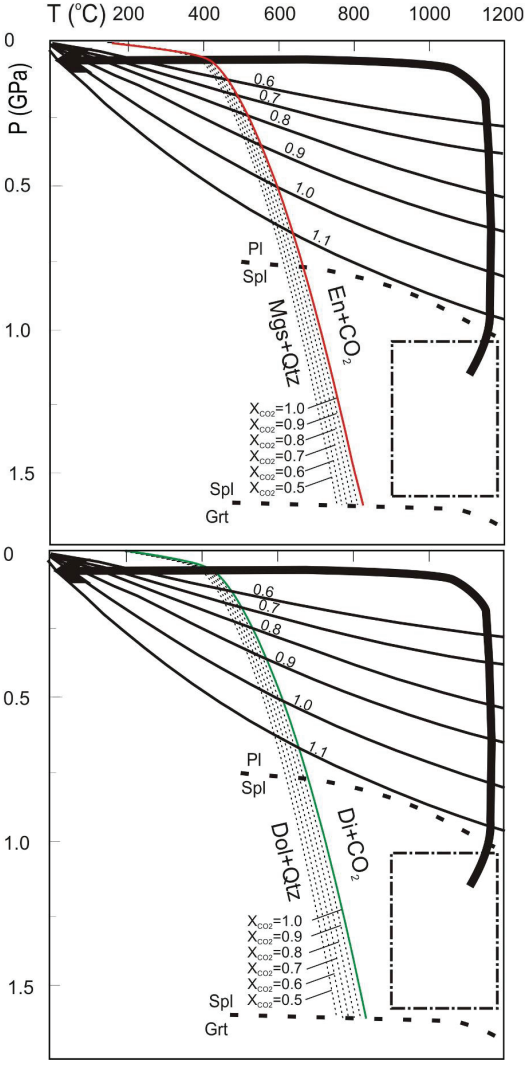
T (°C) 200
400
600
800
1000
1200
P (GPa)
0
0.5
1.0
1.5
0.6
0.7
0.8
0.9
1.0
1.1
Pl
Spl
Mgs+Qtz
En+CO2
XCO2=1.0
XCO2=0.9
XCO2=0.8
XCO2=0.7
XCO2=0.6
XCO2=0.5
Spl
Grt
Dol+Qtz
Di+CO2

12.2.3. Fluid metasomatism

Fluid metasomatism is one of the most common interpretations to understand the trace element transport without change in modal properties of the rock in mantle xenoliths (e.g., Young and Lee, 2009; Malaviarachchi et al., 2010). The Tihany peridotite xenoliths provide better understand the metasomatism affected on upper mantle by fluid. The strong relation between the enrichment of clinopyroxenes in Al_2O_3, TiO_2 (Figure 11; Appendix 1), MREE and Zr (Figure 39; Appendix 4) with the presence of fluid inclusions indicates metasomatism by a volatile-rich fluid on the studied peridotite xenoliths. Therefore, the chemistry of the fluid inclusions can be considered to be characteristic for a residual fluid phase followed by fluid/rock interaction, as it is usually interpreted for the CO_2-rich fluid inclusions (Roedder, 1984; de Vivo *et al.,* 1988; Szabó and Bodnar, 1996; Hidas *et al.,* 2010). Interactions between metasomatic fluids and mantle rocks seem to have occurred heterogeneously (Figure 15), as it is shown in the chemistry of the xenoliths from the least affected NOFLUID through FLUIDPOOR to FLUIDRICH ones.

On the basis of the experimental study of Eggler (1975), pure CO_2 does not play role in dissolving elements even at high temperature and pressure (P~20 kbar, T~1300 ºC). The question to answer is whether which component(s) of the fluid can be significant in dissolving, and therefore transporting trace elements in the lithospheric mantle. In contrast to CO_2, the H_2O behave as a solvent and aqueous fluids may play a great role in trace element transport at high P-T, too (Keppler, 1996; Kessel *et al.,* 2005). However, it can be excluded the possibility that the trace elements, found to be linked to the studied fluid inclusions (Figure 19, Table 3), are dominantly dissolved in H_2O at room temperature, because the duration of the host-mix transient signals (Figure 38) by LA-ICPMS analyses was longer than expected from fluid-rich material (Allan *et al.,* 2005; Bertelli *et al.,* 2009). The transient signals, when a fluid phase is ablated by LA-ICPMS, are more sharp, peak appears for about 2-5 seconds (Allan *et al.,* 2005; Bertelli *et al.,* 2009). No information is available on the presence of salt dissolved in the H_2O-rich fluid phase, however its possibility cannot be excluded. Frezzotti *et al.,* (2010) proved evidences on chlorine and alkali-bearing fluid inclusions from mantle xenoliths from the

Ethiopian plateau. Nevertheless, partition coefficients of chlorine-free and chlorine-bearing hydrous fluid relative to andesitic and rhyolitic melt show values for Zr and Ti close to zero even at high temperature experiments (Keppler, 1996; Spandler *et al.,* 2007). We rather believe that glass phase (Figure 27c), found in the studied inclusions caused transient mixed signals of the fluid inclusion and the host mineral during ablation. Note that the daughter minerals (carbonates, quartz) also may contain some trace elements due to the reaction to the host mineral. However, the host orthopyroxene are highly poor in trace elements (Appendix 3), hence these daughter phases could not incorporated them from the host mineral. Trace elements in these daughter phases might rather originate from the CO_2-rich fluid. Based on previous studies, carbonates may contain valuable Rb, Ba and Sr (Kilias *et al.,* 2006), moreover, the quartz may also contain some trace elements in significant concentrations, such as Al, Ti (Flem *et al.,* 2002; Müller *et al.,* 2003; Rusk *et al.,* 2008), as proved in magmatic and hydrothermal environment.

However, HFS elements, such as Zr and Nb were found to be concentrated in the fluid inclusions, besides, their concentration is increased in FLUIDPOOR and intensely in FLUIDRICH clinopyroxenes, too (Figure 15 and 39). For the signal of Nb and Zr none of the daughter minerals can be responsible. HFS elements preferentially partition into the silicate melt with orders of magnitude higher than the fluid-rich phase. In addition, on the basis of the study of Young and Lee (2009), if HFSE is added to the mantle pyroxenes by cryptic metasomatism, the metasomatic agent is rather a silicate melt than the fluid. The primitive mantle-normalized trace element pattern of the FLUIDPOOR and FLUIDRICH xenoliths' clinopyroxenes is similar to the one from amphibole-bearing spinel lherzolite, found in the same volcanic field, in which coexisting silicate melt and fluid inclusions have been found both in clinopyroxene and orthopyroxene (Szabó *et al.,* 2009; Hidas *et al.,* 2010) (Figure 15). Hidas *et al.* (2010) pointed out that the fluid inclusions might have been trapped after a silicate-volatile immiscibility and the trace element characteristics of the volatile-rich part is controlled by the chemistry of the parental melt. After applying the same semi-quantitative calculation as used by Hidas et al. (2010), similar element ratios have been revealed for Nb, K, Pb, Sr and Zr, and somewhat lower Na (Figure 19; Table 3). Both the similar

clinopyroxene trace element characteristics and the element ratios of the fluid inclusions support the idea that the CO_2-rich fluids trapped in the lithospheric mantle might have dissolved silicate melt components. As a result of decreasing solubility at lower temperatures (e.g., Botcharnikov *et al.,* 2005; 2006), during cooling unmixing of these components could occur and form melt (and subsequently glass). As a result, the former dissolved silicate melt component may present in the inclusions as a thin glass film observed by FIB-SEM of the exposed fluid inclusions (Figure 27). The presence of glass is a direct evidence for the dissolved melt component in the CO_2-rich fluid at lithospheric mantle condition. This fact was already proposed in the study of Hidas *et al.* (2010), however, the glass film was found in situ firstly within the studied fluid inclusions. However, no primary silicate melt inclusions together with fluid inclusions have been detected in the studied rock, in contrast to the work of Hidas *et al.* (2010).

So far, it cannot be undoubtedly determined which solid/fluid phase(s) are the main carrier of which trace elements in the fluid inclusions at ambient conditions. It is highly likely that there were phase separations in the fluid inclusions after entrapment of a *one* fluid phase in the mantle, forming solid daughter phases and a melt phase. Then quenching of the melt phase could have happened onto the wall, preserving further formation of daughter phases. This detailed study provides that dissolved silicate components in a supercritical, volatile (C-O-H-S)-rich fluid may play a great role in carrying many trace elements and, consequently, in chemical overprinting of the peridotitic mantle.

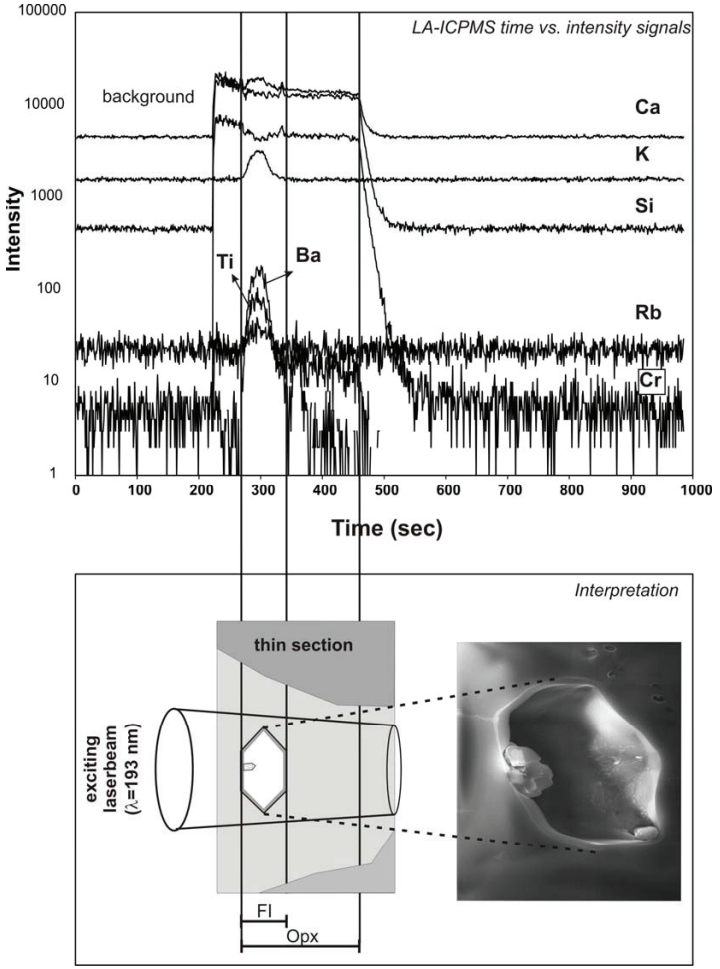

Figure 38. Representative LA-ICPMS time vs. intensity signals on an orthopyroxene (from xenolith Tih0310) showing also the interpretation of the increase of the signals K, Ca, Ba, Ti during the fluid inclusion ablation. The FIB sectioning of the inclusions revealed that increase of the abovementioned elements can be linked to the presence of different solid phases (magnesite, quartz, glass film) found within the fluid inclusion. The picture below is a secondary electron image that was taken during FIB-SEM analyses. More information of the solid phases of this inclusion can be found on Fig. 27

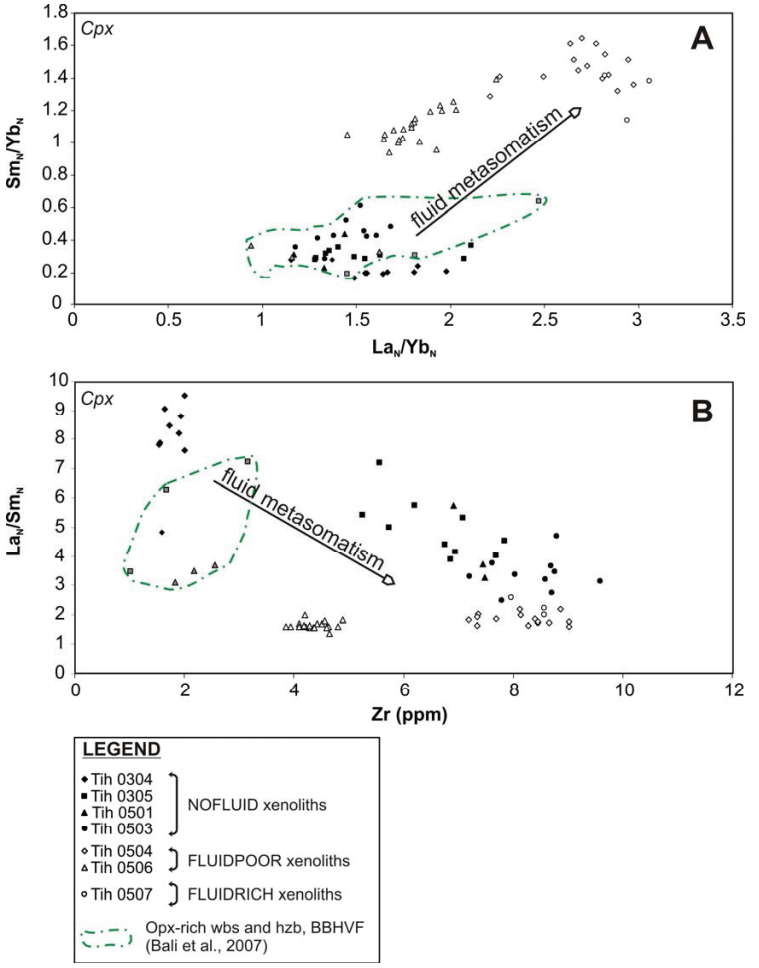

Figure 39. A) La_N/Yb_N vs. Sm_N/Yb_N and B) Zr (in ppm) vs. La_N/Sm_N diagram of the Tihany peridotite xenolith series. For comparison, the green dashed-dotted area yields the compositional range of clinopyroxenes from orthopyroxene-rich xenoliths of BakonyBalaton Highland volcanic field (Szentbékkálla, Bali *et al.,* 2007). Opx-rich wbs and hzb – orthopyroxene-rich websterite and harzburgite, BBHVFBakony-Balaton Highland Volcanic Field

13. SUMMARY OF THE MAIN RESULTS

Due to the detailed study of mantle fluid inclusions from the Central Pannonian Basin (localities: Tihany and Szentbékkálla) with a combination of the application of the fused silica capillary synthetic fluid inclusions, several conclusions can be drawn, as follows:

(1) The petrography, major and trace element of the fluid-inclusion absent (referred to as NOFLUID) Tihany peridotites strongly indicate that the orthopyroxene-enrichment formed by not only SiO_2-, but also Mg-rich melt as a reaction product between the peridotite and "boninite-like" melt. The xenolith from Szentbékkálla must have formed by at least two processes: first when the lherzolitic wall rock and second when the clinopyroxenite vein formed.

(2) Total homogenization experiments were carried out on the studied fluid inclusions by applying the Raman microspectroscopy at moderately high temperature. The results of this work suggest that fluid inclusions trapped at subcontinental lithospheric mantle conditions contain small amounts of H_2O (maximum water content: X_{H2O}=0.11). Thus, the fluid system can be no longer treated as pure or nearly pure (considering the presence of <1 mol% H_2S) CO_2 fluid system. Therefore, the assumption of a pure CO_2 (H_2O-free) fluid in this environment should be reconsidered as the room temperature Raman spectroscopy and microthermometry alone are not suitable for detecting H_2O in such fluid inclusions.

(3) The preparation and application of fused silica capillary fluid inclusions played an important role in controlling the analyses when trying to infer the bulk fluid composition by applying the Raman microspectroscopy at moderately high temperature. Furthermore, the study of the synthetic fluid inclusions revealed the CO_2-density dependence on the Raman peak position of the dissolved H_2O in CO_2 liquid. To our best knowledge, this is the first study to calibrate the position of this peak and also observe the dependence of the peak shift. The liquid CO_2 density may be determined at higher accuracy when taking into account the peak of the dissolved H_2O in CO_2, instead of the distance in the Fermi diads of CO_2. However, for the proper calibration further study is required. Additional feature, the peak broadening of the dissolved H_2O with decreasing CO_2 density, shed

lighted on the influence of CO_2 molecules on the symmetric stretching of the dissolved H_2O.

(4) The fluid inclusion exposure applying the FIB technique revealed the presence of S-bearing solid phase (Fe-sulfide), which, to our best knowledge, has not been previously described in mantle fluid inclusion. Moreover, the presence of sulfide allows us to understand the role of H_2S fluid molecule found by Raman microspectroscopy in the mantle fluid inclusions. In addition, one of the most interesting features observed was a thin film covering the whole wall of the fluid inclusions. This film has a feature that is typical also for the volcanic glasses, showing numerous spherical-shaped holes (vesicles) on the surface as a result of the devolatization. This glass feature supports the idea that the CO_2-rich fluids trapped in the lithospheric mantle might have dissolved silicate melt components.

(5) In the studied samples carbonates and quartz were detected and identified as formed via the reaction of the CO_2-rich fluid and the host orthopyroxene after entrapment. Water should have been completely dissolved in the CO_2-dominated fluid when the reactions took place. With favorable kinetics, the inclusions started to react when the xenolith enclosed in the cooling lava reached the reaction curve at about 400-600 ºC. The "quenching" of the glass phase excluded the completion of the carbonation reaction. As carbonates were previously found in other mantle xenolith-hosted CO_2-rich fluid inclusions, it is suggested that the presence of the glass phase is generally reasonable in mantle fluid inclusions.

(6) The strong relation between the chemical characteristics and the presence of fluid inclusions indicates metasomatism by a volatile-rich phase on the Tihany fluid inclusion-bearing peridotite xenoliths.

(7) During entrapment of a one phase, supercritical COHS-bearing volatile-like species was characteristic; further phase separation, such as the formation of daughter phases and the quenching the glass onto the wall happened after formation of fluid inclusion in the mantle. Our detailed study provides that dissolved silicate melt in a supercritical, volatile-rich fluid may play a great role in chemical overprinting of the peridotite wall rock.

14. MAGYAR NYELVŰ ÖSSZEFOGLALÓ

A Pannon-medence központi részéről (BakonyBalaton-felvidék vulkáni terület) származó negatív kristály alakú fluidumokat tartalmazó peridotit xenolitok részletes vizsgálatára került sor jelen doktori munkában, különös hangsúlyt fektetve a fluidum zárványokra. A köpeny xenolitok mellett egy újdonságnak számító technikával szintetikus CO_2-H_2O zárványokat állítottam elő és szintén részletesen tanulmányoztam, amelyek kiváló lehetőséget nyújtottak a természetes köpenyfluidumok modellezéséhez. A fluidumzárványok összetételének ilyen pontos meghatározása mindezidáig még nem történt meg. A CO_2 mellett egyéb fluidummolekulák - H_2O és H_2S - kimutatása és relatív koncentrációjuk (mol%-ban kifejezett) meghatározását is elvégeztem. Mindezt melegítéssel kombinált Raman technikával sikerült megvalósítani. Az eredmények szerint akár 11 mol% H_2O jelenlére sem kimutatható fluidumzárványban, ha nem alkalmazzuk az előbb említett módszert. A CO_2-ban oldott H_2O Raman sávjának pozíciójáról továbbá sikerült kimutatni, hogy az a CO_2 sűrűségétől függ, amely potenciális lehetőséget nyújthat jövőbeni kutatások esetében a CO_2 sűrűségének meghatározására olyan fluidumzárványban, ahol a mikrotermometriai megfigyeléseknek a fluidumzárvány kismérete akadályt szab. Karbonát és kvarc leányásványok jelenlétét is sikerült kimutatni, ami a csapdázódott fluidum és a bezáró ásvány (orto- és klinopiroxén) reakciójának termékei. Meghatároztam a reakció P–T függését. A fókuszált ionsugaras feltárás során e reakciótermékek térfogatarányát becsültem meg, lehetőséget nyújtva a csapdázódott CO_2 visszaszámolására tömegegyensúlyt feltételezve. Az ionsugaras feltárásával továbbá olyan szilárd fázisok (Fe-szulfid és kőzetüveg) detektálása történt, amelyekről köpenyfluidumokban eddig még nem tettek említést: a Fe-gazdag szulfid fázis a H_2S jelenlétének fontosságát erősíti meg, a zárvány falát borító, hólyagüreges kőzetüveg pedig fontos szerepet kap a fluidum/peridotit kölcsönhatásának megértésében. A tihanyi xenolitok közül a fluidumzárványokat tartalmazó peridotitok gazdagodtak fő-és nyomelemekben (Al, Ti, Zr, Nb, könnyű ritkaföldfémek) a fluidumzányokat nem tartalmazókhoz képest. A természetes fluidumzárványok félkvantitatív nyomelemkoncentrációi a felsorolt elemekben relatív dúsak.

15. ENGLISH SUMMARY

Due to the detailed study of mantle fluid inclusions from the Central Pannonian Basin (localities: Tihany and Szentbékkálla) with a combination of the application of the fused silica capillary synthetic fluid inclusions several conclusions can be drawn, as follows:

(1)The petrography, major and trace element of the fluid-inclusion absent (referred to as NOFLUID)Tihany peridotites strongly indicate that the orthopyroxene-enrichment was likely formed by a reaction of peridotite and a SiO_2-, and MgO-rich "boninite-like" melt.

(2) Results of this work suggest that H_2O in fluid inclusions trapped at subcontinental lithospheric mantle conditions is more common than it was previously thought. Therefore, the assumption of a pure CO_2 (H_2O-free) fluid in this environment must be reconsidered. Room temperature Raman spectroscopy and microthermometry alone are not suitable for detecting H_2O in such fluid inclusions.

(3) The study of the synthetic fluid inclusions revealed the CO_2-density dependence on the Raman peak position of the dissolved H_2O in CO_2 liquid. The liquid CO_2 density may be determined at higher accuracy when taking into account the peak of the dissolved H_2O in CO_2 instead of the distance in the Fermi diads of CO_2.

(4) The fluid inclusion exposure applying the FIB technique revealed the presence of S-bearing solid phase (Fe-sulfide), and a glass film covering the wall of the inclusion. The idea is thus supported that the CO_2-rich fluid existing in the lithospheric mantle dissolves silicate melt components.

(5) In the studied samples carbonates and quartz were also detected and then identified as formed via the reaction of the CO_2-rich fluid and the host pyroxene after entrapment. The "quenching" of the glass phase probably excluded the completion of the carbonation reaction, as a result, preserved the residual CO_2 and the daughter phases in the fluid inclusions.

(6) The strong relation between the chemical characteristics and the presence (or absence) of fluid inclusions (e.g. xenolith groups "NOFLUID" or "FLUIDRICH") indicates metasomatism by a volatile-rich phase on the Tihany fluid inclusion-bearing peridotites. The metasomatic agent was likely a supercritical CO_2-rich, COHS-bearing volatile-rich fluid containing silicate component, as well.

REFERENCES

Allan, M. M., B. W. D. Yardley, L. J. Forbes, K. I. Shmulovich, D. A. Banks, and T. J. Shepherd (2005), Validation of LA-ICP-MS fluid inclusion analysis with synthetic fluid inclusions, *American Mineralogist*, *90*, 1767-1775.

Anders, E., and N. Grevesse (1989), Abundances of the elements: meteoric and solar, *Geochimica et Cosmochimica Acta*, *53*, 197-214.

Andersen, T., and E.-R. Neumann (2001), Fluid inclusions in mantle xenoliths, *Lithos*, *55*, 301-320.

Anderson, A., and T. McCarron (2011), Three-dimensional textural and chemical characterization of polyphase inclusions in spodumene using a dual focused ion beam - scanning electron microscope (FIB-SEM) *Canadian Mineralogist*, 49, 541-553.

Antignano, A., and C. E. Manning (2008), Rutile solubility in H_2O, H_2O–SiO_2, and H_2O–$NaAlSi_3O_8$ fluids at 0.7–2.0 GPa and 700–1000 °C: Implications for mobility of nominally insoluble elements, *Chemical Geology*, *255*, 283-293.

Arai, S. (1980), Dunite-harzburgite-chromitite complexes as refractory residue in the Sangun-Yamaguchi zone, western Japan, *Journal of Petrology*, *21*, 141-165.

Arai, S. (1994), Compositional variation of olivine-chromian spinel in Mg-rich magmas as a guide to their residual spinel peridotites, *Journal of Volcanology and Geothermal Research*, *59*, 279-293.

Arai, S., K. Kadoshima, and T. Morishita (2006), Widespread arc-related melting in the mantle section of the northern Oman ophiolite as inferred from detrital chromian spinels, *Journal of the Geological Society*, *163*, 869-879.

Arai, S., Y. Shimizu, and F. Gervilla (2003), Quartz diorite veins in a peridotite xenolith from Tallante, Spain: Implications for reaction and survival of slab derived SiO_2-oversaturated melt in the upper mantle, *Proc. Japan Academy Ser. B*, *79*, 145-150.

Arai, S., Y. Shimizu, T. Morishita, and I. Yoshito (2006), A new type of orthopyroxenite xenolith from Takashima, Southwest Japan: silica enrichment of the mantle by evolved alkali basalt, *Contributions to Mineralogy and Petrology*, *152*, 387-398.

Bada, G., and F. Horváth (2001), On the structure and tectonic evolution of the Pannonian basin and surrounding orogens, *Acta Geologica Hungarica*, *44*, 301-327.

Bada, G., F. Horváth, P. Dövényi, P. Szafián, G. Windhoffer, and S. Cloetingh (2007), Present-day stress field and tectonic inversion in the Pannonian basin, *Global and Planetary Change*, *58*, 165-180.

Bakker, R. J. (2003), Package FLUIDS 1. Computer programs for analysis of fluid inclusion data and for modelling bulk fluid properties, *Chemical Geology*, *194*, 3-23.

Bakker, R. J., and J. B. H. Jansen (1990), Preferential water leakage from fluid inclusions by means of mobile dislocations, *Nature*, *345*, 58-60.

Bakker, R. J., and J. B. H. Jansen (1991), Experimental post-entrapment water-loss from synthetic CO_2-H_2O inclusions in natural quartz, *Geochimica et Cosmochimica Acta*, *55*, 2215-2230.

Bali, E., G. Falus, C. Szabó, D. W. Peate, K. Hidas, K. Török, and T. Ntaflos (2007), Remnants of boninitic melts in the upper mantle beneath the central Pannonian

Basin?, *Mineralogy and Petrology*, *90*, 51-72.
Bali, E., C. Szabó, O. Vaselli, and K. Török (2002), Significance of silicate melt pockets in upper mantle xenoliths from the Bakony-Balaton Highland Volcanic Field, Western Hungary, *Lithos*, *61*, 79-102.
Bali, E., Z. Zajacz, I. Kovács, C. Szabó, W. Halter, O. Vaselli, K. Török, and R. J. Bodnar (2008), A quartz-bearing orthopyroxene-rich websterite xenolith from the Pannonian Basin, western Hungary: Evidence for release of quartz-saturated melts from a subducted slab., *Journal of Petrology*, *49*, 421-439.
Bali, E., A. Zanetti, C. Szabo, D. W. Peate, and T. E. Waight (2008), A micro-scale investigation of melt production and extraction in the upper mantle based on silicate melt pockets in ultramafic xenoliths from the Bakony-Balaton Highland Volcanic Field (Western Hungary), *Contributions to Mineralogy and Petrology*, *155*, 165-179.
Balla, Z. (1984), The Carpathian loop and the Pannonian basin: kinematic analysis, *Geophysical Transactions*, *30*, 313-353.
Balogh, K., E. Árva-Sós, Z. Pécskay, and L. Ravasz-Baranyai (1986), K/Ar dating of post-sarmatian alcalibasaltic rocks in Hungary, *Acta Miner.-Petr. Szeged*, *28*, 75-93.
Balogh, K., A. Jámbor, Z. Partényi, L. Ravasz-Baranyai, and G. Solti (1982), K/Ar radigenic age of Transdanubian basalts, *Annual Report of the Hungarian Geological Institute from 1980*, 243-259.
Balogh, K., and K. Németh (2005), Evidence for the neogene small-volume intracontinental volcanism in western Hungary: K/Ar geochronology of the Tihany Maar volcanic complex, *Geologica Carpathica 56*, 91-99.
Balogh, K., and Z. Pécskay (2001), K/Ar and Ar/Ar geochronological studies in the Pannonian–Carpathians–Dinarides (PANCARDI) region, *Acta Geologica Academiae Scientiarum Hungaricae 44*, 281–301.
Bergman, S. C., and J. Dubessy (1984), CO_2-CO fluid inclusions in a composite peridotite xenolith: implications for upper mantle oxygen fugacity, *Contributions to Mineralogy and Petrology*, *85*, 1-13.
Berkesi, M., K. Hidas, T. Guzmics, J. Dubessy, R. J. Bodnar, C. Szabó, B. Vajna, and T. Tsunogae (2009), Detection of small amounts of H_2O in CO_2-rich fluid inclusions using Raman spectroscopy, *Journal of Raman Spectroscopy*, *40*, 1461-1463.
Berkesi, M., C. Szabó, R. J. Bodnar, and L. Fedele (2007), CO_2-bearing fluid inclusions in upper mantle xenoliths from Tihany (western Hungary): Minimum trapping pressures and trace element compositions, *Geochimica et Cosmochimica Acta*, *71*, A83-A83.
Bertelli, M., T. Baker, J. S. Cleverley, and T. Ulrich (2009), Geochemical modelling of a Zn–Pb skarn: Constraints from LA–ICP–MS analysis of fluid inclusions, *Journal of Geochemical Exploration*, *102*, 13-26.
Bodinier, J. L., C. Dupuy, and J. Vernieres (1988), Behavior of trace elements during upper mantle metasomatism - evidences from the Lherz massif, *Chemical Geology*, *70*, 152-152.
Bodnar, R. J. (2003), Reequilibration of fluid inclusions, in *Fluid Inclusions: Analysis and Interpretation*, edited by I. Samson, A. Anderson and D. Marshall, pp. 213-230, Mineralogical Association of Canada.

Bodnar, R. J., and P. M. Bethke (1984), Systematics of stretching of fluid inclusions1. Fluorite and sphalerite at 1 atmosphere confining pressure, *Economic Geology*, *79*, 141-161.

Bodnar, R. J., P. R. Binns, and D. L. Hall (1989), Synthetic fluid inclusions 6. quantitative-evaluation of the decrepitation behavior of fluid inclusions in quartz at one atmosphere confining pressure, *Journal of Metamorphic Geology*, *7*, 229-242.

Bodnar, R. J., C. W. Burnham, and S. M. Sterner (1985), Synthetic fluid inclusions in natural quartz. III. Determination of phase equilibrium properties in the system H_2O-NaCI to 1000°C and 1500 bars, *Geochimica et Cosmochimica Acta*, *49*, 1861-1873.

Boily, M., and C. Dion (2002), Geochemistry of boninite-type volcanic rocks in the Frotet-Evans greenstone belt, Opatica subprovince, Quebec: implications for the evolution of Archaean greenstone belts, *Precambrian Research*, *115*, 349-371.

Bonelli, R., and M. L. Frezzotti (2003), Raman Spectra Database, *http://www.dst.unisi.it/geofluidslab/Raman%20intro.htm*.

Borsy, Z., K. Balogh, M. Kozák, and Z. Pécskay (1986), Contributions to the evolution of the Tapolca-basin, Hungary, *Acta Geographica Debrecina 23*, 79–104

Botcharnikov, R., H. Behrens, and F. Holtz (2006), Solubility and speciation of C-O-H fluids in andesitic melt at T=1100-1300 degrees C and P=200 and 500MPa, *Chemical Geology*, *229*, 125-143.

Botcharnikov, R., M. Freise, F. Holtz, and H. Behrens (2005), Solubility of C-O-H mixtures in natural melts: new experimental data and application range of recent models, *Annals of Geophysics*, *48*, 633-646.

Boyd, F. R. (1989), Compositional distinction between oceanic and cratonic lithosphere, *Earth and Planetary Science Letters*, *96*, 15-26.

Bozzo, A. T., H.-S. Chen, J. R. Kass, and A. J. Barduhn (1975), The properties of the hydrates of chlorine and carbon dioxide, *Desalination*, *16*, 303-320.

Brey, G. P., and T. P. Köhler (1990), Geothermobarometry in four phase lherzolites II. New thermobarometers and practical assessment of existing thermobarometers, *Journal of Petrology*, *31*, 1353-1378.

Burke, E. A. J. (2001), Raman microspectrometry of fluid inclusions, *Lithos*, *55*, 139-158.

Cesare, B. (1995), Graphite precipitation in C–O–H fluid inclusions: closed system compositional and density changes, and thermobarometric implications, *Contributions to Mineralogy and Petrology*, *122*, 25-33.

Channell, J. E. T., and H. W. Kozur (1997), How many oceans? Meliata, Vardar, and Pindos oceans in Mesozoic Alpine paleogeography, *Geology*, *25*, 183-186.

Chou, I.-M., Y. Song, and R. C. Burruss (2008), A new method for synthesizing fluid inclusions in fused silica capillaries containing organic and inorganic material, *Geochimica et Cosmochimica Acta*, *72*, 5217-5231.

Connolly, J. A. D. (2009), The geodynamic euation of state:what and how, *Geochemistry, Geophysics, Geosystems*, *10*, DOI:10.1029/2009GC002540.

Connolly, J. A. D., and B. Cesare (1993), C-O-H-S fluid composition and oxygen fugacity in graphitic metapelites, *Journal of Metamorphic Geology*, *11*, 379-388.

Connolly, J. A. D., and V. Trommsdorff (1991), Petrogenetic grids for metacarbonate rocks:pressure-temperature phase-diagram projection for mixed-volatile systems,

Contributions to Mineralogy and Petrology, *108*, 93-105.
Crawford, A. J., T. J. Falloon, and D. H. Green (1989), Classification, petrogenesis and tectonic setting of boninites, in *Boninites and Related Rocks*, edited by A. J. Crawford, pp. 1-49, Unwin Hyman, London.
Császár, G., and G. Lelkesné-Felvári (1999), Balaton Phyllite Formation Group, in *Geology of the Balaton Highland*, edited by T. Csillag, pp. 15-21, Magyar Állami Földtani Intézet, Budapest.
Csernyi, T., and R. Corrada (1989), New results of the detailed geophysical-geological investigation of Holocen sediments and basins of Lake Balaton, *Annual Report of the Hungarian Geological Institute from 1987*, 341-347.
Csontos, L. (1995), Tertiary tectonic evolution of the Intra-Carpathian area: a review., *Acta Vulcanologica*, *7*, 1-13.
Csontos, L., and A. Nagymarosy (1998), The mid-Hungarian line: a zone of repeated tectonic inversions, *Tectonophysics*, *297*, 51-71.
Csontos, L., A. Nagymarosy, F. Horváth, and M. Kovac (1992), Tertiary evolution of the Intra-Carpathian area: A model, *Tectonophysics*, *208*, 221-241.
Csontos, L., and A. Vörös (2004), Mesozoic plate tectonic reconstruction of the Carpathian region., *Palaeogeography Palaeoclimatology Palaeoecology*, *210*, 1-56.
Cvetković, V., H. Downes, D. Prelević, M. Jovanović, and M. Lazarov (2004), Characteristics of the lithospheric mantle beneath East Serbia inferred from ultramafic xenoliths in Palaeogene basanites, *Contributions to Mineralogy and Petrology*, *148*, 335-357.
Dantas, C., M. Grégoire, E. Koester, R. V. Conceição, and N. Rieck Jr (2009), The lherzolite–websterite xenolith suite from Northern Patagonia (Argentina): Evidence of mantle–melt reaction processes, *Lithos*, *107*, 107-120.
de Vivo, B., M. L. Frezzotti, A. Lima, and R. Trigila (1988), Spinel lherzolite nodules from Oahu (Hawaii): a fluid inclusion study, *Bulletin de Minéralogie*, *111*, 307-319.
Defant, M. J., and M. S. Drummond (1990), Derivation of some modern arc magmas by melting of young subducted lithosphere, *Nature*, *347*, 662-665.
Dégi, J., R. Abart, K. Török, E. Bali, R. Wirth, and D. Rhede (2010), Symplectite formation during decompression induced garnet breakdown in lower crustal mafic granulite xenoliths: mechanisms and rates, *Contributions to Mineralogy and Petrology*, *159*, 293–314.
Dégi, J., R. Abart, K. Török, D. Rhede, and E. Petrishcheva (2009), Evidence for xenolith–host basalt interaction from chemical patterns in Fe–Ti-oxides from mafic granulite xenoliths of the Bakony–Balaton Volcanic field (W-Hungary), *Mineralogy and Petrology*, *95*, 219-234.
Demény, A., T. W. Vennemann, E. Hegner, G. Nagy, J. Milton, A. Embey-Isztin, Z. Homonnay, and G. Dobosi (2004), Trace element and C-O-Sr-Nd isotope evidence for subduction-related carbonate-silicate melts in mantle xenoliths (Pannonian Basin, Hungary), *Lithos*, *75*, 89-113.
Diamond, L. W. (2001), Review of the systematics of CO_2–H_2O fluid inclusions, *Lithos*, *55*, 69-99.
Ding, J. (2010), The pH determination of palaeofluids: experimental and thermodynamic

approach, 174 pp, Nancy Université - Nanjing University, Nanjing.
Dobrzhinetskaya, L. F., H. W. Green, T. E. Mitchell, and R. M. Dickerson (2001), Metamorphic diamonds: mechanism of growth and inclusion of oxides, *Geology*, *29*, 263–266.
Dobrzhinetskaya, L. F., H. W. Green, M. Weschler, M. Darus, Y.-C. Wang, H.-J. Massonne, and B. Stöckhert (2003), Focused ion beam technique and transmission electron microscope studies of microdiamonds from the Saxonian Erzgebirge, Germany, *Earth and Planetary Science Letters*, *210*, 399–410.
Dobrzhinetskaya, L. F., R. Wirth, and H. W. Green II. (2005), Direct observation and analysis of a trapped COH fluid growth medium in metamorphic diamond, *TerraNova*, *17*, 472–477.
Dobrzhinetskaya, L. F., R. Wirth, and H. W. Green II. (2006), Nanometric inclusions of carbonates in Kokchetav diamonds from Kazakhstan: a new constraint for the depth of metamorphic diamond crystallization, *Earth and Planetary Science Letters*, *243*, 85–93.
Downes, H. (2001), Formation and modification of the shallow sub-continental lithospheric mantle: a review of geochemical evidence from ultramafic xenolith suites and tectonically emplaced ultramafic massifs of western and central Europe, *Journal of Petrology*, *42*, 233-250.
Downes, H., J. L. Bodinier, M. Thirlwall, J.-P. Lorand, and J. Fabries (1991), REE and Sr–Nd isotopic geochemistry of eastern Pyrenean peridotite massifs: sub - continental lithospheric mantle modified by continental magmatism, *Journal of Petrology, Special Lherzolites Issue*, 97-115.
Downes, H., A. Embey-Isztin, and M. Thirlwall (1992), Petrology and geochemistry of spinel peridotite xenoliths from the western Pannonian Basin (Hungary) - Evidence for an association between enrichment and texture in the upper mantle, *Contributions to Mineralogy and Petrology*, *109*, 340-354.
Downes, H., G. Pantó, T. Póka, D. P. Mattey, and P. B. Greenwood (1995), Calc-alkaline volcanics of the Inner Carpathian arc, Northern Hungary: new geochemical and oxygen isotopic results, *Acta Vulcanologica*, *7*, 29-41.
Downes, H., and O. Vaselli (1995), The lithospheric mantle beneath the Carpathian-Pannonian Region: a review of trace element and isotopic evidence from ultramafic xenoliths, *Acta Vulcanologica*, *7*, 219-229.
Duan, Z., N. Moller, and J. H. Weare (1992), An equation of state for the CH_4–CO_2–H_2O system: II. Mixtures from 50 to 1000 °C and 0 to 1000 bar, *Geochimica et Cosmochimica Acta, 56*, 2619-2631.
Duan, Z., N. Moller, and J. H. Weare (1996), A general equation of state for supercritical fluid mixtures and molecular dynamics simulation of mixture PVTX properties., *Geochimica et Cosmochimica Acta, 60*, 1209-1216.
Duan, Z., and Z. Zhang (2006), Equation of state of the H_2O, CO_2, and H_2O-CO_2 systems up to 10 GPa and 2573.15 K: Molecular dynamics simulations with ab initio potential surface, *Geochimica et Cosmochimica Acta, 70*, 2311-2324.
Dubessy, J., D. Audeoud, R. Wilkins, and C. Kosztolanyi (1982), The use of the Raman microprobe MOLE in the determination of the electrolytes dissolved in the aqueous phase of fluid inclusions, *Chemical Geology*, *37*, 137-150.
Dubessy, J., M.-C. Boiron, A. Moisette, C. Monnin, and N. Sretenskaya (1992),

Determinations of water, hydrates and pH in fluid inclusions by micro-Raman spectrometry, *European Journal of Mineralogy*, *4*, 885-894.

Dubessy, J., J. Ding, P. Robert, M. Leisen, A. Giraud, and M. Berkesi (2009), Capillary techniques combined with vibratoinal spectroscopies applied to fluid inclusions and phase equilibria., *ECROFI (European Current Research On Fluids Inclusions)-XX Abstract Book*, 67-68.

Dubessy, J., Ding, J., Robert, P., Leisen, M., Aparicio, B., Nguyen-Trung, Ch., Berkesi, M. and Uteyev, R. (2010) Raman spectroscopy in capillary cells to 400°C and 2 kbar applied to geochemistry. GeoRaman, 28 June–02 July, Sydney, Australia

Dubessy, J., N. Guilhaumou, J. Mullis, and M. Pagel (1984), Reconaissance par microspectrométrie Raman dans les inclusions fluides de H_2S et CO_2 solides à domaine de fusion comparable, *Bulletin de Minéralogie*, *107*, 189-192.

Dubessy, J., B. Poty, and C. Ramboz (1989), Advances in C-O-H-N-S fluid geochemistry based on micro-Raman spectrometric analysis of fluid inclusions, *European Journal of Mineralogy*, *1*, 517-534.

Embey-Isztin, A. (1976), Amphibolite/lherzolite composite xenolith from Szigliget, north of the lake Balaton, Hungary, *Earth and Planetary Science Letters*, *31*, 297-304.

Embey-Isztin, A. (1984), Texture types and their relative frequencies in ultramafic and mafic xenoliths from Hungarian alkali basaltic rocks, *Annales Hist.-Nat. Mus. Natn. Hung.*, *76*, 27-42.

Embey-Isztin, A., and G. Dobosi (1995), Mantle source characteristics for Miocene-Pleistocene alkali basalts, Carpathian-Pannonian Region: a review of trace elements and isotopic composition, *Acta Vulcanologica*, *7*, 155–166.

Embey-Isztin, A., G. Dobosi, R. Altherr, and H. P. Meyer (2001), Thermal evolution of the lithosphere beneath the western Pannonian Basin: evidence from deep-seated xenoliths, *Tectonophysics*, *331*, 285-306.

Embey-Isztin, A., H. Downes, D. E. James, B. G. Upton, G. Dobosi, H. G. Scharbert, and G. A. Ingram (1993), The petrogenesis of Pliocene alkaline volcanic rocks from the Pannonian Basin, Eastern Central Europe, *Journal of Petrology*, *34*, 317–343.

Embey-Isztin, A., H. Downes, P. D. Kempton, G. Dobosi, and M. Thirlwall (2003), Lower crustal granulite xenoliths from the Pannonian Basin. Part 1: mineral chemistry, thermobarometry and petrology, *Contributions to Mineralogy and Petrology*, *144*, 652-670.

Embey-Isztin, A., H. G. Scharbert, H. Dietrich, and H. Poultidis (1989), Petrology and geochemistry of peridotite xenoliths in alkali basalts from the Transdanubian Volcanic Region, West Hungary, *Journal of Petrology*, *30*, 79-105.

Embey-Isztin, A., H. G. Scharbert, H. Dietrich, and H. Poultidis (1990), Mafic granulites and clinopyroxenite xenoliths from the Transdanubian Volcanic Region (Hungary): implications for the deep structure of the Pannonian Basin, *Mineralogical Magazine*, *54*, 463-483.

Fall, A., J. D. Rimstidt, and R. J. Bodnar (2009), The effect of fluid inclusion size on determination of homogenization temperature and density of liquid-rich aqueous inclusions, *American Mineralogist*, *94*, 1569-1579.

Fall, A., B. Tattitch, and R. J. Bodnar (2011), Combined microthermometric and Raman spectroscopic technique to determine the salinity of H_2O–CO_2–NaCl fluid inclusions based on clathrate melting, *Geochimica et Cosmochimica Acta*, *75*, 951-

964.
Falloon, T. J., L. V. Danyushevsky, A. J. Crawford, S. Meffre, J. D. Woodhead, and S. H. Bloomer (2008), Boninites and Adakites from the Northern Termination of the TongaTrench: Implications for Adakite Petrogenesis, *Journal of Petrology*, *49*, 697-715.
Falus, G. (2004), Microstructural analysis of upper mantle peridotites: their application in understanding mantle processes during the formation of the Intra-Carpathian Basin System, 149 pp, Eötvös University, Budapest.
Falus, G., M. R. Drury, H. L. M. Roermund, and C. Szabó (2004), Magmatism-related localized deformation in the mantle: a case study, *Contributions to Mineralogy and Petrology*, *146*, 493-505.
Falus, G., and C. Szabó (2004), Upper mantle xenoliths from Tihany: traceable lithosphere evolution in Bakony – Balaton Highland Volcanic Field? (in Hungarian with English abstract), *Földtani Közlöny 134*, 499-520.
Falus, G., C. Szabó, and O. Vaselli (2000), Mantle upwelling within the Pannonian Basin: evidence from xenolith lithology and mineral chemistry, *Terra Nova*, *12*, 295-302.
Falus, G., A. Tommasi, J. Ingrin, and C. Szabó (2008), Deformation and seismic anisotropy of the lithospheric mantle in the southeastern Carpathians inferred from the study of mantle xenoliths, *Earth and Planetary Science Letters*, *272*, 50-64.
Fermi, E. (1931), Über den Ramaneffekt des kohlendioxyds, *Zeitung Physica*, *71*, 250-259.
Fisher, J. R. (1976), The volumetric properties of H_2O - a graphical portrayal, *Journal of Research of the U.S.G.S.* , *4*, 189-193.
Flem, B., R. B. Larsen, A. Grimstvedt, and J. Mansfeld (2002), In situ analysis of trace elements in quartz by using laser ablation inductively coupled plasma mass spectrometry, *Chemical Geology*, *182*, 237-247.
Fodor, L., Csontos, L., G. Bada, I. Győrfi, and L. Benkovics (1999), Tertiary tectonic evolution of the Pannonian basin system and neighbouring orogens: a new synthesis of paleostress data, in *The Mediterranean Basins: Tertiary Extensions within the Alpine orogen*, edited by B. Durand, L. Jolivet, F. Horváth and M. Séranne, pp. 295-334, Geological Society Special Publication, London.
Fodor, L., B. Jelen, E. Márton, D. Skaberne, J. Car, and M. Vrabec (1998), Miocene-Pliocene tectonic evolution of the Slovenian Periadriatic fault: Implications for Alpine-Carpathian extrusion models, *Tectonics*, *17*, 690-709.
Fodor, L., A. Magyari, M. Kázmér, and A. Fogarasi (1992), Gravity-Flow Dominated Sedimentation On The Buda Paleoslope (Hungary) - Record Of Late Eocene Continental Escape Of The Bakony Unit, *Geologische Rundschau*, *81*, 695-716.
Frezzotti, M. L., T. Andersen, E.-R. Neumann, and S. L. Simonsen (2002), Carbonatite melt–CO_2 fluid inclusions in mantle xenoliths from Tenerife, Canary Islands: a story of trapping, immiscibility and fluid–rock interaction in the upper mantle, *Lithos*, *64*, 77– 96.
Frezzotti, M. L., E. A. J. Burke, B. de Vivo, B. Stefanini, and I. M. Villa (1992), Mantle fluids in pyroxenite nodules from Salt Lake crater (Oahu, Hawaii), *European Journal of Mineralogy*, *4*, 1137-1153.
Frezzotti, M. L., S. Ferrando, A. Peccerillo, M. Petrelli, F. Tecce, and A. Perucchi (2010),

Chlorine-rich metasomatic H_2O–CO_2 fluids in amphibole-bearing peridotites from Injibara (Lake Tana region, Ethiopian plateau): Nature and evolution of volatiles in the mantle of a region of continental flood basalts, *Geochimica et Cosmochimica Acta*, *74*, 3023–3039.

Frezzotti, M. L., and A. Peccerillo (2007), Diamond-bearing COHS fluids in the mantle beneath Hawaii, *Earth and Planetary Science Letters*, *262*, 273–283.

Géczy, B. (1973), The origin of the Jurassic faunal provinces and the Mediterranean plate tectonics, *Ann Univ Sci Bp R Eötvös nom Sect Geol*, *16*, 99–114.

Géczy, B. (1984), Provincialism of Jurassic ammonites: examples from Hungarian faunas, *Acta Geologica Hungarica*, *27*, 379-389.

Gemmer, L., and G. A. Housemann (2007), Convergence and extension driven by lithospheric gravitational instability: evolution of the Alpine–Carpathian–Pannonian system, *Geophysical Journal International*, *168*, 1276-1290.

Gméling, K., K. Németh, U. Martin, N. Eby, and Z. Varga (2007), Boron concentrations of volcanic fields in different geotectonic settings, *Journal of Volcanology and Geothermal Research*, *159*, 70–84.

Grad, M., A. Guterch, G. R. Keller, T. Janik, E. Hegedűs, J. Vozár, A. Slaczka, T. Tiira, and J. Yliniemi (2006), Lithospheric structure beneath trans-Carpathian transect from Precambrian platform to Pannonian basin: CELEBRATION 2000 seismic profile CEL05, *Geophysical Journal International*, *111*.

Green, D. H., and M. E. Wallace (1988), Mantle metasomatism by ephemeral carbonatite melts, *Nature*, *336*, 459-462.

Griffin, W., S. O'Reilly, and C. Ryan (1999), The composition and origin of subcontinental lithospheric mantle, in *Mantle Petrology: Field observation and high-pressure experimentation: A tribute to Francis R. (Joe) Boyd*, edited by Y. Fei and C. Ryan, pp. 13-45, The Geochemical Society, Houston.

Grove, T. L., N. Chatterjee, S. W. Parman, and E. Médard (2006), The influence of H_2O on mantle wedge melting, *Earth and Planetary Science Letters*, *249*, 74-89.

Grove, T. L., L. T. Elkins-Tanton, S. W. Parman, N. Chatterjee, O. Müntener, and G. A. Gaetani (2003), Fractional crystallization and mantle-melting controls on calc-alkaline differentiation trends, *Contributions to Mineralogy and Petrology*, *145*, 515-533.

Guillong, M., D. L. Meier, M. M. Allan, C. A. Heinrich, and B. W. D. Yardley (2008), SILLS: A MATLAB-based program for the reduction of laser ablation ICP–MS data of homogeneous materials and inclusions, *Mineralogical Association of Canada Short Course*, *40*, 328-333.

Guzmics, T., J. Kodolányi, I. Kovács, C. Szabó, E. Bali, and T. Ntaflos (2008), Primary carbonatite melt inclusions in apatite and in K-feldspar of clinopyroxene-rich mantle xenoliths hosted in lamprophyre dikes (Hungary), *Mineralogy and Petrology*, *94*, 225-242.

Guzmics, T., R. H. Mitchell, C. Szabó, M. Berkesi, R. Milke, and R. Abart (2011), Carbonatite melt inclusions in coexisting magnetite, apatite and monticellite in Kerimasi calciocarbonatite, Tanzania: melt evolution and petrogenesis, *Contributions to Mineralogy and Petrology*, *161*, 177–196.

Guzmics, T., Z. Zajacz, J. Kodolányi, H. Werner, and C. Szabó (2008), LA-ICP-MS study of apatite- and K-feldspar-hosted primary carbonatite melt inclusions in

clinopyroxenite xenoliths from lamprophyres, Hungary, Implication for significance of carbonatite melts in the Earth's mantle, *Geochimica et Cosmochimica Acta*, *72*, 1864-1886.

Győrfy, I., and L. Csontos (1994), Structural evolution of SE Hungary and Neogene basins of the Apuseni Mountains (Romania), *Rom J Tect Reg Geol*, *75*, 19-20.

Haas, J., G. Hámor, and L. Korpás (1999), Geological setting and tectonic evolution of Hungary, *Geologica Hungarica, Series Geologica*, *24*, 179-196.

Haas, J., S. Kovács, L. Krystyn, and R. Lein (1995), Significance of Late Permian Triassic facies zones and terrain reconstructions in the Alpine North Pannonian domain, *Tectonophysics*, *242*, 19-40.

Haas, J., P. Mioc, J. Pamic, B. Tomljenovic, P. Árkai, A. Bérczi-Makk, B. Koroknai, S. Kovács, and E. R. Felgenhauer (2000), Complex structural pattern of the Alpine-Dinaridic-Pannonian triple junction., *International Journal of Earth Sciences*, *89*, 377-389.

Halter, W. E., T. Pettke, C. A. Heinrich, and B. Rothen-Rutishauser (2002), Major to trace element analysis of melt inclusions by laser-ablation ICP-MS: methods of quantification, *Chemical Geology*, *183*, 63-86.

Harangi, S. (2001), Neogene magmatism in the Alpine-Pannonian Transition Zone-a model for melt generation in a complex geodynamic setting, *Acta Vulcanologica*, *13*, 25-39.

Harangi, S., H. Downes, M. Thirlwall, and K. Gméling (2007), Geochemistry, petrogenesis and geodynamic relationships of miocene calc-alkaline volcanic rocks in the western carpathian arc, eastern central Europe, *Journal of Petrology*, *48*, 2261-2287.

Harangi, S., M. Wilson, and S. Tonarini (1995), Petrogenesis of Neogene potassic volcanic rocks in the Pannonian Basin, *Acta Vulcanologica*, *7*, 125-134.

Hartmann, G., and K. H. Wedepohl (1993), The composition of peridotites tectonites from the Ivrea Complex, northern Italy: Residues from melt extraction, *Geochimica et Cosmochimica Acta*, *57*, 1761-1782.

Heaney, P. J., E. P. Vincenzi, L. A. Giannuzzi, and K. J. T. Livi (2001), Focused ion beam milling: a method of site-specific sample extraction for microanalysis of Earth and planetary materials, *American Mineralogist*, *86*, 1094–1099.

Hermann, J., and D. Rubatto (2009), Accessory phase control on the trace element signature of sediment melts in subduction zones, *Chemical Geology*, *265*, 512-526.

Hermann, J., C. Spandler, A. Hack, and A. V. Korsakov (2006), Aqueous fluids and hydrous melts in high-pressure and ultra-high pressure rocks: Implications for element transfer in subduction zones, *Lithos*, *92*, 399–417.

Hidas, K. (2006), The oldest sampled lithosphere in the Bakony-Balaton-Highland Volcanic Field:petrography and geochemistry of xenoliths from the Tihany Maar Complex (in Hungarian with English abstract), 127 pp, ELTE, Budapest.

Hidas, K., G. Falus, C. Szabó, P. J. Szabó, I. Kovács, and T. Földes (2007), Geodynamic implications of flattened tabular equigranular textured peridotites from the Bakony-Balaton Highland Volcanic Field (Western Hungary), *J. Geodyn.*, *43*, 484–503.

Hidas, K., T. Guzmics, C. Szabó, I. Kovács, R. J. Bodnar, Z. Zajacz, Z. Nédli, L. Vaccari, and A. Perucchi (2010), Coexisting silicate melt inclusions and H_2O-bearing, CO_2-

rich fluid inclusions in mantle peridotite xenoliths from the Carpathian–Pannonian region (central Hungary), *Chemical Geology*, *274*, 1–18.

Holland, T. J. B., and R. Powell (1990), An enlarged and updated internally consistent dataset with uncertainties and correlations: the system K_2O-Na_2O-CaO-MgO-MnO-FeO-Fe_2O_3-Al_2O_3-TiO_2-SiO_2-C-H_2-O_2, *Journal of Metamorphic Geology*, *8*, 89-124.

Horváth, F. (1988), Neotectonic behavior of te Alpine-Mediterranean region, in *The Pannonian Basin : a study in basin evolution*, edited by L. H. Royden and F. Horváth, pp. 49-55, American Association of Petroleum Geologist, Hungarian Geological Society, Tulsa, Budapest.

Horváth, F. (1993), Towards a mechanical model for the formation of the Pannonian basin, *Tectonophysics*, *226*, 333-357.

Horváth, F. (2007), A Pannon-medence geodinamikája — Eszmetörténeti tanulmány és geofizikai szintézis, in *ELTE*, edited, p. 238, Budapest.

Horváth, F., and S. Cloetingh (1996), Stress-induced late-stage subsidence anomalies in the Pannonian basin, *Tectonophysics*, *266*, 287-300.

Horváth, F., and L. H. Royden (1981), Mechanism for the formation of the Intra-Carpathian Basins: a review, *Earth Evolution Science*, *3-4*, 307-316.

Howard-Lock, H. E., and B. P. Stoicheff (1971), Raman intensity measurements of the Fermi diad υ_1, $2\upsilon_2$ in $^{12}CO_2$ and $^{13}CO_2$, Journal of Molecular Spectroscopy, 37, 321-326.

Huismanns, R. S., Y. Y. Podladchikov, and S. Coetingh (2001), Dynamic modeling of the transition from passive to active rifting, application to the Pannonian basin, *Tectonics*, *20*, 1021–1039.

Hurai, V. (2010), Fluid inclusion geobarometry: Pressure corrections for immiscible H_2O–CH_4 and H_2O–CO_2 fluids, *Chemical Geology*, *278*, 201-211.

Jacobs, G. K., and D. M. Kerrick (1981), Methane: an equation of state with applications to ternary system H_2O–CO_2–CH_4, *Geochimica et Cosmochimica Acta, 45*, 607-614.

Janik, T., M. Grad, A. Guterch, J. Vozár, M. Bielik, A. Vozárova, E. Hegedűs, C. A. Kovács, I. Kovács, G. R. Keller, and C. W. Group (2011), Crustal structure of the Western Carpathians and Pannonian Basin: Seismic models from CELEBRATION 2000 data and geological implications, *Journal of Geodynamics*, *52*, 97-113.

Johannes, W. (1969), An experimental investigation of the system MgO-SiO_2-H_2O-CO_2, *American Journal of Science*, *267*, 1083-1104.

Jolivet, L., and C. Faccenna (2000), Mediterranean extension and the Africa-Eurasia collision, *Tectonics*, *19*, 1095-1106.

Jugovics, L. (1968), Structure of the Basalt Regions in the Balaton Highland, *Annual Report of the Hungarian Geological Institute*, 75-82.

Kawakami, Y., J. Yamamoto, and H. Kagi (2003), Micro-raman densimeter for CO_2 inclusions in mantlederived minerals, *Applied Spectroscopy*, *57*, 1333-1339.

Kázmér, M., and S. Kovács (1985), Permian-Palaeogene palaeogeography along the eastern part of the Insubric-Periadriatic Linament system: evidence for continental escape of the Bakony-Drauzug Unit, *Acta Geologica Hungarica*, *28*, 71-84.

Kelemen, P. B., H. J. Dick, and J. E. Quick (1992), Formation of harzburgite by pervasive melt/rock reaction in the upper mantle, *Nature*, *358*, 635-641.

Kelemen, P. B., S. R. Hart, and S. Bernstein (1998), Silica enrichment in the continental upper mantle via melt/rock reaction, *Earth and Planetary Science Letters*, *164*, 387-406.

Keppler, H. (1996), Hydrous metasomatism of the sub-arc mantle, Lihir, Papua New Guinea: petrology and geochemistry of fluid metasomatised mantle wedge., *Nature*, *380*, 237-240.

Kerrick, D. M., and G. K. Jacobs (1981), A modified Redlich–Kwong equation for H_2O, CO_2, and H_2O–CO_2 mixtures, *American Journal of Science, 281*, 735-767.

Kerkhof, A. M., and U. F. Hein (2001), Fluid inclusion petrography, *Lithos*, *55*, 27-47.

Kessel, R., M. W. Schmidt, P. Ulmer, and T. Pettke (2005), Trace element signature of subduction-zone fluids, melts and supercritical liquids at 120–180 km depth, *Nature*, *437*, 724-727.

Kilias, S. P., M. Pozo, M. Bustillo, M. G. Stamatakis, and J. P. Calvo (2006), Origin of the Rubian carbonate-hosted magnesite deposit, Galicia, NW Spain: mineralogical, REE, fluid inclusion and isotope evidence, *Mineralium Deposita*, *41*, 713-733.

Knight, C. L., and R. J. Bodnar (1988), Synthetic fluid inclusions: IX. Critical PVTX properties of NaCI-H_20 solutions, *Geochimica et Cosmochimica Acta*, *53*, 3-8.

Kobe, K. A., and R. E. Lynn (1953), The critical properties of elements and compounds. , *Chemical Reviews*, *52*, 117-236.

Kokelaar, B. P. (1983), The mechanism of Surtseyan volcanism, *Journal of the Geological Society of London*, *140*, 939-944.

Konečnỳ, V., J. Lexa, K. Balogh, and P. Konečný (1995), Alkali basalt volcanism in Shouthern Slovakia: volcanic forms and time evolution, *Acta Vulcanologica*, *7*, 167-173.

Kovać, M., J. Kral., M. Márton, D. Plasienka, and P. Uher (1994), Alpine uplift history of the Central West Carpathians: geochrnological, sedimentary and structural data, *Geologica Carpathica*, *45*, 83-96.

Kovács, I., L. Csontos, C. Szabó, E. Bali, G. Falus, K. Benedek, and Z. Zajacz (2007), Paleogene–early Miocene igneous rocks and geodynamics of the Alpine-Carpathian-Pannonian-Dinaric region: An integrated approach, *Geological Society of America Special Paper*, *418*, 93-111.

Kovács, I., H. S. O'Neill, J. Hermann, and E. H. Hauri (2010), Site-specific infrared O-H absorption coefficients for water substitution into olivine, *American Mineralogist*, *95*, 292-299.

Kovács, I., and C. Szabó (2008), Middle Miocene volcanism in the vicinity of the Middle Hungarian Zone: Evidence for an inherited enriched mantle source, *J. Geodyn.*, *45*, 1-17.

Kovács, S., T. Szederkényi, J. Haas, G. Hámor, and A. Nagymarosy (2000), Tectonostratigraphic terranes in the pre-Neogene basement of the Hungarian part of the Pannonian area, *Acta Geologica Hungarica*, *43*, 225-328.

Koziol, A. M., and R. C. Newton (1995), Experimental determination of the reactions magnesite + quartz =enstatite + CO_2, and magnesite = periclase + CO_2, and enthalpies of formation of enstatite and magnesite, *American Mineralogist*, *80*, 1252-1260.

Lee, M. R., P. A. Bland, and G. Graham (2003), Preparation of TEM samples by focused ion beam (FIB) techniques: applications to the study of clays and phyllosilicates in

meteorites, *Mineralogical Magazine*, *67*, 581–592.
Lee, M. R., D. J. Brown, C. L. Smith, M. E. Hodson, M. MacKenzie, and R. Hellmann (2007), Characterization of mineral surfaces using FIB and TEM: a case study of naturally weathered alkali feldspars, *American Mineralogist*, *92*, 1383–1395.
Lenkey, L. (1999), Geothermics of the Pannonian Basin and its bearing on the tectonics of basin evolution, *Vrije Universiteit*, 1-215.
Lide, D. R. (2004), *CRC handbook of chemistry and physics: a ready-reference book of chemical and physical data*, 2712 pp., CRC press.
Lin, F., R. J. Bodnar, and S. P. Becker (2007b), Experimental determination of the Raman CH_4 symmetric stretching ($\square_1$) band position from 1–650 bar and 0.3–22 ^oC: Application to fluid inclusion studies, *Geochimica et Cosmochimica Acta*, *71*, 3746-3756.
Lin, F., A. K. Sum, and R. J. Bodnar (2007a), Correlation of methane Raman $\square_1$ band position with fluid density and interactions at the molecular level, *Journal of Raman Spectroscopy*, *38*, 1510-1515.
Longerich, H. P., S. E. Jackson, and D. Günther (1996), Laser ablation inductively coupled plasma mass spectrometric transient signal data acquisition and analyte concentration calculation, *Journal of Analytical Atomic Spectrometry*, *11*, 899-904.
Lüttge, A., and P. Metz (1991), Mechanism and kinetics of the reaction 1 dolomite + 2 quartz = 1 diopside + 2 CO_2 investigated by powder experiments *Canadian Mineralogist*, *29*, 803-821.
Malaspina, N., J. Hermann, M. Scambelluri, and R. Compagnioni (2006), Polyphase inclusions in garnet-orthopyroxenite (Dabie Shan, China) as monitors for metasomatism and fluid-related trace element transfer in subduction zone peridotite, *Earth and Planetary Science Letters*, *249*, 173-187.
Malaviarachchi, S. P. K., A. Makishima, and E. Nakamura (2010), Melt-Peridotite Reactions and Fluid Metasomatism in the Upper Mantle, Revealed from the Geochemistry of Peridotite and Gabbro from the Horoman Peridotite Massif, Japan Journal of Petrology, 51, 1417-1445.
Manikyamba, C., S. M. Naqvi, D. V. Subba Rao, M. Ram Mohan, T. C. Khanna, T. G. Rao, and G. L. N. Reddy (2004), Boninites from the Neoarchaean Gadwal Greenstone belt, Eastern Dharwar Craton, India: implications for Archaean subduction processes, *Earth and Planetary Science Letters*, *230*, 65-83.
Martin, U., A. Auer, K. Németh, and C. Breitkreuz (2003), Mio/Pliocene phreatomagmatic volcanism in a fluviolacustrine basin in western Hungary, *Journal of the Geological Institute of AS Czech Republic*, *15*, 75-81.
Martin, U., and K. Németh (Mio/Pliocene phreatomagmatic volcanism in the Western Pannonian Basin), Geologica Hungarica, Series Geologica, *26*, 198.
Márton, E. (1987), Paleomagnetism and tectonics in the Mediterranean region, *Journal of Geodynamics*, *7*, 33-57.
Márton, E. (1997), Paleomagnetic aspects of plate tectonics in the Carpatho-Pannonian region, *Mineralium Deposita*, *32*, 441-445.
Márton, E., and P. Márton (1978), Tectonic implications of a new palaeomagnetic result from the Jurassic of the Transdanubian Central Mountains, *Tectonophysics*, *45*, T1-T6.
Matas, J., P. Gillet, Y. Ricard, and I. Martinez (2000), Thermodynamic properties of

carbonates at high pressures from vibrational modelling, *European Journal of Mineralogy*, *12*, 703-720.
McCreery, R. L. (2000), *Raman Spectroscopy for Chemical Analysis*, 420 pp., John Wiley & Sons.
McDonough, W. F., and S. s. Sun (1995), The composition of the Earth, *Chemical Geology*, *120*, 223-253.
McInnes, B. I. A., M. Grégoire, R. A. Binns, P. M. Herzig, and M. D. Hannington (2001), Hydrous metasomatism of the sub-arc mantle, Lihir, Papua New Guinea: petrology and geochemistry of fluid metasomatised mantle wedge, *Earth and Planetary Science Letters*, *188*, 169-183.
McKenzie, D., and R. K. O'Nions (1991), Partial melt distributions from inversion of Rare Earth Element concentrations, *Journal of Petrology*, *32*, 1021-1091.
Melcher, F., T. Meisel, J. Puhl, and F. Koller (2002), Petrogenesis and geotectonic setting of ultramafic rocks in the Eastern Alps: constraints from geochemistry, *Lithos*, *65*, 69-112.
Morse, S. A. (1980), *Basalts and phase diagrams: an introduction to the quantitative use of phase diagrams in igneous petrology*, 493 pp., Springer Verlag, New York.
Müller, A., M. Wiedenbeck, A. M. Kerkhof, A. Kronz, and K. Simon (2003), Trace elements in quartz - a combined electron microprobe, secondary ion mass spectrometry, laser-ablation ICP-MS, and cathodoluminescence study, *European Journal of Mineralogy*, *15*, 747-763.
Mutchler, S. R., L. Fedele, and R. J. Bodnar (2008), Analysis Management System (AMS) for reduction of laser ablation ICPMS data, in *Laser-Ablation-ICPMS in the Earth Sciences: Current Practices and Outstanding Issues*, edited by P. Sylvester, pp. 318-327, Mineralogical Association of Canada Short Course Series.
Nagymarosy, A., and M. Báldi-Beke (1993), The Szolnok Unit and its probable paleogeographic position, *Tectonophysics*, *226*, 457-470.
Nasdala, L., D. C. Smith, R. Kaindl, and M. A. Ziemann (2004), Raman spectroscopy: analytical perspectives in mineralogical research, in *EMU Notes in Mineralogy 6: Spectroscopic Methods in Mineralogy*, edited by A. Beran and E. Libowitzky, pp. 281-329, Eötvös University Press, Budapest.
Nemcok, M., L. Pospisil, J. Lexa, and R. A. Donelick (1998), Tertiary subduction and slab break-off model of the Carpathian-Pannonian region, *Tectonophysics*, *295*, 307-340.
Németh, K., and U. Martin (1999), Volcanism of the Tihany Volcano, in *Pannon Encyclopaedia*, edited by D. Karátson, Kertek 2000 Publishing House, Budapest.
Németh, K., U. Martin, and S. Harangi (2001), Miocene phreatomagmatic volcanism at Tihany (Pannonian Basin, Hungary), *Journal of Volcanology and Geothermal Research*, *111*, 111-135.
Németh, K., J. D. L. White, A. Reay, and U. Martin (2003), Compositional variation during monogenetic volcano growth and its implications for magma supply to continental volcanic fields, *Journal of the Geological Society 160*, 523-530.
Newton, R. C., and C. E. Manning (2000), Quartz solubility in concentrated aqueous NaCl solutions at deep crust– upper mantle metamorphicconditions: 2 –15 kbar and 500– 900 ^{o}C, *Geochimica et Cosmochimica Acta*, *64*, 2993-3005.
Normann, M. D. (1998), Melting and metasomatism in the continental lithosphere: laser

ablation ICPMS analysis of minerals in spinel lherzolites from eastern Australia, *Contributions to Mineralogy and Petrology*, *130*, 240-255.

Obst, M., P. Gasser, D. Mavrocordatos, and M. Dittrich (2005), TEM-specimen preparation of cell/mineral interfaces by focused ion beam milling, *American Mineralogist*, *90*, 1270–1277.

O'Reilly, S., and W. Griffin (1996), 4-D Lithosphere Mapping: methodology and examples, *Tectonophysics*, *262*, 3-18.

Pécskay, Z., J. Lexa, A. Szakács, K. Balogh, I. Seghedi, V. Konečný, M. Kovács, E. Márton, M. Kaličak, V. Széky-Fux, T. Póka, P. Gyarmati, O. Edelstein, E. Rosu, and B. Žec (1995), Space and time distribution of Neogene-Quaternary volcanism in the Carpatho-Pannonian Region, *Acta Vulcanologica*, *7*, 15-28.

Pintér, Z., I. Kovács, M. Berkesi, C. Szabó, T. J. F. Djoukam, J. P. Tchouankoue, and A. Perucchi (2011), Unique phlogopite and amphibole-bearing fluid inclusions in upper mantle xenoliths from Cameroon Volcanic Line, *ECROFI (European Current Research On Fluids Inclusions)-XXI Abstract Book*, accepted abstract.

Pironon, J., J. O. W. Grimmer, S. Teinturier, D. Guillaume, and J. Dubessy (2003), Dissolved methane in water: temperature effect on Raman quantification in fluid inclusions, *Journal of Geochemical Exploration*, *78-79*, 111-115.

Rapp, R. P., N. Shimizu, M. D. Normann, and G. S. Applegate (1999), Reaction between slabderived melts and peridotite in the mantle wedge: experimental constraints at 3.8 GPa, *Chemical Geology*, *160*, 335-356.

Roedder, E. (1963), Studies of fluid inclusions II:freezing data and their interpretation, *Economic Geology*, *58*, 167-208.

Roedder, E. (1965), Liquid CO_2 inclusions in olivine bearing nodules and phenocrysts from basalts, *American Mineralogist*, *50*, 1746-1782.

Roedder, E. (1983), Geobarometry of ultramafic xenoliths from Loihi Seamount, Hawaii, on the basis of CO2 inclusions in olivine, Earth and Planetary Science Letters, 66, 369-379.

Roedder, E. (1984), Fluid inclusions, *Rev. Mineral.*, *12*, 1-646.

Rogers, G., and A. D. Saunders (1989), Magnesian andesites from Mexico, Chile and the Aleutian Islands: implications for magmatism associated with ridge-trench collision, in *Boninites and Related Rocks*, edited by A. J. Crawford, pp. 416-445, Unwin Hyman, London.

Rosasco, G. J., E. Roedder, and J. H. Simmons (1975), Laser-Excited Raman Spectroscopy for Nondestructive Partial Analysis of Individual Phases in Fluid Inclusions in Minerals, *Science*, *190*, 557-560.

Rosenbaum, J. M., A. Zindler, and J. L. Rubenstone (1996), Mantle fluids: Evidence from fluid inclusions, *Geochimica et Cosmochimica Acta*, *60*, 3229-3252.

Rosso, K. M., and R. J. Bodnar (1995), Microthermometric and Raman spectroscopic detection limits of CO_2 in fluid inclusions and the Raman spectroscopic characterization of CO_2, *Geochimica et Cosmochimica Acta*, *59*, 3961-3975.

Royden, L. H., and F. Horváth (1988), *The Pannonian basin – a study in basin evolution*, 394 pp., Amer Assoc Petrol Geol Mem, Tulsa, Oklahoma.

Rudnick, R. L., W. F. McDonough, and B. W. Chappell (1993), Carbonatite metasomatism in the northern Tanzanian mantle—petrographic and geochemical characteristics, *Earth and Planetary Science Letters*, *114*, 463-475.

Rusk, B. G., H. A. Lowers, and M. H. Reed (2008), Trace elements in hydrothermal quartz: Relationships to cathodoluminescent textures and insights into vein formation, *Geology*, *36*, 547-550.

Savoie, R., and M. Pigeon-Gosselin (1983), Emission Spectra of Rare Gas Discharge Lamps for the Calibration of Raman Spectrometers with Excitation at 488.0 and 514.5 nm, *Canadian Journal of Spectroscopy*, *28*, 133-138.

Scambelluri, M., J. Fiebig, N. Malaspina, O. Müntener, and T. Pettke (2004), Serpentinite Subduction: Implications for Fluid Processes and Trace-Element Recycling, *International Geology Review*, *46*, 595-618.

Scambelluri, M., and P. Philippot (2001), Deep fluids in subduction zones, *Lithos*, *55*, 213-227.

Scambelluri, M., R. Vannucci, A. De Stefano, M. Preite-Martinez, and G. Rivalenti (2009), CO_2 fluid and silicate glass as monitors of alkali basalt/peridotite interaction in the mantle wedge beneath Gobernador Gregores, Southern Patagonia, *Lithos*, *107*, 121-133.

Schiano, P., and R. Clocchiatti (1994), Worldwide occurrence of silica-rich melts in sub-continental and suboceanic mantle minerals, *Nature*, *368*, 621-624.

Seitz, J. C., J. D. Pasteris, and V. Morgan, G.B. (1993), Quantitative analysis of mixed volatile fluids by Raman microprobe spectroscopy: a cautionary note on spectral resolution and peak shape, *Applied Spectroscopy*, *47*, 816-820.

Severs, M. J., T. Azbej, J. B. Thomas, C. W. Mandeville, and R. J. Bodnar (2007), Experimental determination of H_2O loss from melt inclusions during laboratory heating: Evidence from Raman spectroscopy, *Chemical Geology*, *237*, 358-371.

Shaw, C. S. J., Y. Thibault, A. D. Edgar, and F. E. Lloyd (1998), Mechanisms of orthopyroxene dissolution in silica-undersaturated melts at 1 atmosphere and implications for the origin of silica-rich glass in mantle xenoliths, *Contributions to Mineralogy and Petrology*, *132*, 354-370.

Skogby, H. (2006), Water in natural mantle minerals I: Pyroxenes, in *Water in Nominally Anhydrous Minerals*, edited by H. Keppler and J. R. Smyth, pp. 155-166, The Mineralogical Society of America, Chantilly, USA.

Soustelle, V., A. Tommasi, S. Demouchy, and D. A. Ionov (2010), Deformation and Fluid/Rock Interaction in the Supra-subduction Mantle: Microstructures and Water Contents in Peridotite Xenoliths from the AvachaVolcano, Kamchatka, *Journal of Petrology*, *51*, 363-394.

Span, R., and W. Wagner (1996), A new equation of state for carbon dioxide covering the fluid region from the triple-point temperature to 1100 K at pressures up to 800 MPa, *Journal of Physical and Chemical References Data 25*, 1513-1558.

Spandler, C., J. A. Mavrogenes, and J. Hermann (2007), Experimental constraints on element mobility from subducted sediments using high-P synthetic fluid/melt inclusions, *Chemical Geology*, *239*, 228-249.

Sterner, S. M., and R. J. Bodnar (1989), Synthetic fluid inclusions 7. Re-equilibration of fluid inclusions in quartz during laboratory-simulated metamorphic burial and uplift, *Journal of Metamorphic Geology*, *7*, 243-260.

Sterner, S. M., and R. J. Bodnar (1991), Synthetic fluid inclusions. X: Experimental determination of P-V-T-X properties in the CO_2-H_2O system to 6 kb and 700°C, *American Journal of Science*, *291*, 1-54.

Stöckhert, B. (2003), Focused ion beam technique and transmission electron microscope studies of microdiamonds from the Saxonian Erzgebirge, Germany, *Earth and Planetary Science Letters*, *210*, 399–410.

Streckeisen, A. (1976), To each plutonic rock its proper name, *Earth Science Reviews*, *12*, 1-33.

Szabó, C., and R. J. Bodnar (1996), Changing magma ascent rates in the Nógrád-Gömör Volcanic Field Northern Hungary/Southern Slovakia: Evidence from CO_2-rich fluid inclusions in metasomatized upper mantle xenoliths, *Petrology*, *4*, 221-230.

Szabó, C., R. J. Bodnar, and A. V. Sobolev (1996), Metasomatism associated with subduction-related, volatile-rich silicate melt in the upper mantle beneath the Nógrád-Gömör Volcanic Field, northern Hungary/southern Slovakia: evidence from silicate melt inclusions, *European Journal of Mineralogy*, *8*, 881-899.

Szabó, C., G. Falus, Z. Zajacz, I. Kovács, and E. Bali (2004), Composition and evolution of lithosphere beneath the Carpathian–Pannonian Region: a review, *Tectonophysics*, *393*, 119–137.

Szabó, C., S. Harangi, and L. Csontos (1992), Review of Neogene and Quaternary volcanism of the Carpathian-Pannonian region, *Tectonophysics*, *208*, 243-256.

Szabó, C., S. Harangi, O. Vaselli, and H. Downes (1995), Temperature and oxygen fugacity in peridotite xenoliths from the Carpathian-Pannonian Region, *Acta Vulcanologica*, *7*, 231-239.

Szabó, C., K. Hidas, E. Bali, Z. Zajacz, I. Kovács, K. Yang, T. Guzmics, and K. Török (2009), Melt-wall rock interaction in the mantle as shown by silicate melt inclusions in peridotite xenoliths from the central Pannonian Basin (western Hungary), *Island Arc*, *18*, 375-400.

Szakács, A., and I. Seghedi (1995), The Calimani-Gurghiu-Hargitha volcanic chain, East Carpathians, Romania: volcanological features, *Acta Vulcanologica*, *7*, 145-155.

Szente, I. (1995), Bivalvia from the Bathonian (Middle Jurassic) of the Mecsek Mts, Hungary, *Annales Univ Sci Budapest, Sect Geol*, *30*, 93-109.

Tari, G. (1991), Multiple Miocene block rotation in the Bakony Mountains, Transdanubian Central Range, Hungary, *Tectonophysics*, *199*, 93-108.

Tari, G. (1994), Alpine tectonics of the Pannonian Basin, 501 pp, Rice University, Houston.

Tari, G., F. Horváth, and J. Rumpler (1992), Styles of extension in the Pannonian Basin, *Tectonophysics*, *208*, 203-219.

Tašárová, A., J. C. Afonso, M. Bielik, H.-J. Götze, and J. Hók (2009), The lithospheric structure of the Western Carpathian–Pannonian Basin region based on the CELEBRATION 2000 seismic experiment and gravity modelling, *Tectonophysics*, *475*, 454–469.

Trial, A. F., R. L. Rudnick, L. D. Ashwal, D. J. Henry, and S. C. Bergman (1984), Fluid inclusions in mantle xenoliths from Ichinomegata, Japan: Evidence for subducted H_2O, *EOS Trans. Amer. Geophys. Un.*, *306*.

Trommsdorff, V., and J. A. D. Connolly (1990), Constraints on phase diagram topology for the system CaO- MgO- SiO_2 -CO_2 - H_20, *Contributions to Mineralogy and Petrology*, *104*, 1-7.

Tullner, T., and T. Csernyi (2003), New aspects of lake-level changes: Lake Balaton, Hungary, *Acta Geologica Hungarica*, *46*, 215-238.

Vakarcs, G., P. R. Vail, G. Tari, G. Pogácsás, R. E. Mattick, and A. Szabó (1994), 3rd-order middle Miocene-early Pliocene depositional sequences in the prograding delta-complex of the Pannonian Basin, *Tectonophysics*, *240*, 81-106.

Viti, C., and M. L. Frezzotti (2000), Re-equilibration of glass and CO_2 inclusions in xenolith olivine: A TEM study, *American Mineralogist*, *85*, 1390-1396.

Vityk, M. O., and R. J. Bodnar (1995), Do fluid inclusions in high-grade metamorphic terranes preserve peak metamorphic density during retrograde decompression?, *American Mineralogist*, *80*, 641-644.

Vörös, A. (1993), Jurassic microplate movements and brachiopod migrations in the western part of the Tethys, *Palaeogeography, Palaeoclimatology, Palaeoecology*, *100*, 125-145.

Walker, A. M., J. Hermann, A. J. Berry, and H. S. O'Neill (2007), Three water sites in upper mantle olivine and the role of titanium in the water weakening mechanism, *Journal of Geophysical Research-Solid Earth*, *112*.

Watson, E. B., J. M. Brenan, and D. R. Baker (1990), Distribution of fluids in the continental mantle, in *Continental Mantle*, edited by M. A. Menzies, pp. 111-125, Clarendon Press, Oxford.

Wein, G. (1969), Tectonic review of the Neogene covered areas of Hungary, *Acta Geologica Hungarica*, *13*, 399-436.

White, J. D. L., and B. F. Houghton (2000), Surtseyan and related eruptions, in *Encyclopedia of Volcanoes*, edited by H. Sigurdsson and B. Houghton, McNutt, S., Rymer, H., Stix, J., pp. 495-512, Academic Press, New York.

Wijbrans, J., K. Németh, U. Martin, and K. Balogh (2007), Ar-40/Ar-39 geochronology of Neogene phreatomagmatic volcanism in the western Pannonian Basin, Hungary, *Journal of Volcanology and Geothermal Research*, *164*, 193-204.

Willingshofer, E., and S. Cloetingh (2003), Present-day lithospheric strength of the Eastern Alps and its relationship to neotectonics, *Tectonics*, *22*, 1075.

Willingshofer, E., J. D. van Wees, S. Cloetingh, and F. Neubauer (1999), Thermomechanical consequences of Cretaceous continent–continent collision in the eastern Alps (Austria): insights from two-dimensional modeling, *Tectonics*, *18*, 809-826.

Wilson, M., and H. Downes (1991), Tertiary–Quaternary extension related alkaline magmatism in Western and Central Europe, *Journal of Petrology*, *32*, 811-849.

Wirth, R. (2004), Focused Ion Beam (FIB): a novel technology for advanced application of micro-and nanoanalysis in geosciences and applied mineralogy, *European Journal of Mineralogy*, *16*, 863–876.

Wirth, R. (2009), Focused Ion Beam (FIB) combined with SEM and TEM: Advanced analytical tools for studies of chemical composition, microstructure and crystal structure in geomaterials on a nanometre scale, *Chemical Geology*, *261*, 217–229.

Wirth, R., and A. Rocholl (2003), Nanocrystalline diamond from the Earth's mantle underneath Hawaii, *Earth and Planetary Science Letters*, *211*, 357-369.

Wright, R. B., and C. H. Wang (1973), Density effect on the Fermi resonance in gaseous CO_2 Raman scattering, *Journal of Chemical Physics*, *58*, 2893-2895.

Wulff-Pedersen, E., E.-R. Neumann, and B. B. Jensen (1996), The upper mantle under La Palma, Canary Islands: formation of K-rich silicic melt and its importance as a metasomatic agent, *Contributions to Mineralogy and Petrology*, *125*, 113-139.

Xu, Y. G., M. A. Menzies, J. L. Bodinier, R. M. Bedini, P. Vroon, and J. C. C. Mercier (1998), Melt percolation and reaction atop a plume: evidence from the poikiloblastic peridotites xenoliths from Boreé (Massif Central, France), *Contributions to Mineralogy and Petrology*, *132*, 65-84.

Yaxley, G., A. J. Crawford, and D. H. Green (1991), Evidence for carbonatite metasomatism in spinell peridotite xenoliths from western Victoria, Australia, *Earth and Planetary Science Letters*, *107*, 305-317.

Yaxley, G., D. H. Green, and V. Kamenetsky (1998), Carbonatite metasomatism in the southeastern Australian lithosphere, *Journal of Petrology*, *39*, 1917-1930.

Young, H. P., and C.-T. A. Lee (2009), Fluid-metasomatized mantle beneath the Ouachita belt of southern Laurentia: Fate of lithospheric mantle in a continental orogenic belt, *Lithosphere*, *1*, 370-383.

Zanetti, A., M. Mazzucchelli, G. Rivalenti, and R. Vannucci (1999), The Finero phlogopite-peridotite massif: an example of subduction-related metasomatism, *Contributions to Mineralogy and Petrology*, *134*, 107-122.

Zen (1966), Construction of Pressure-Temperature Diagrams for Multicomponent Systems after the Method of Schreinemakers -- A Geometric Approach, U.S. Geol. Surv. Bull, 1225, 1-56.

APPENDICES